# Fluorine free lithium ion batteries using aqueous polymeric binders

A comparative study on polymeric binders for greener batteries

Joep Borninkhof

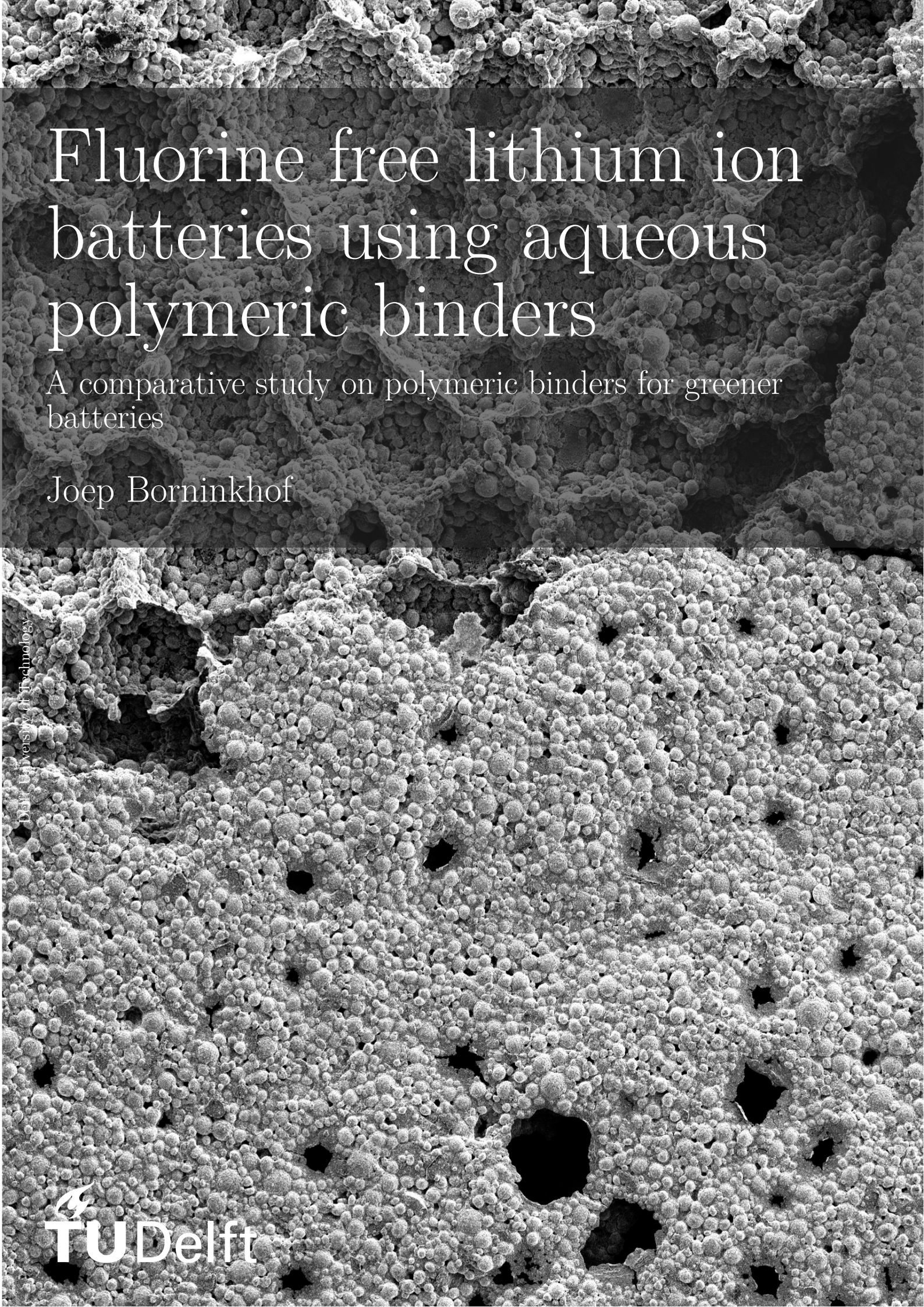

Delft University of Technology

TU Delft

# Fluorine free lithium ion batteries using aqueous polymeric binders

## A comparative study on polymeric binders for greener batteries

by

Joep Borninkhof

Student number 4766636

To obtain the degree of Master of Science
at the Delft University of Technology

*Thesis committee*

| | |
|---|---|
| Supervisor: | Prof. Dr. Ir. F.M. Mulder - TU Delft |
| External examiner: | Dr. E.M. Kelder - TU Delft |

Faculty of Applied Sciences, Delft.
Materials for Energy Conversion and Storage | MECS

Cover: Top view of NMC811 electrode, fabricated in this study with the composite binder CMC/SBR

TU Delft

# Acknowledgements

I want to express my gratitude to Fokko Mulder for making it possible for me to do my thesis within the MECS group. I have had a great time working on this thesis project where I learned a lot.
A very special thanks to my daily supervisor Mark Weijers for comprehensively assisting me and for providing knowledge and guidance throughout my research. Thank you for always taking the time to help by very easily explaining the most difficult subjects. Thank you for always being kind and joking around. Thanks to the members of the SOLiDIFY group for the fruitful discussions in the weekly meetings. Especially Pranav Karanth, who was always willing to help with kindness and for sharing his expertise. I would like to thank the members of the MECS and SEE group for helping me with my questions and providing me with insights during the group meetings. Also big thanks to Laurence Macray for making sure I had enough coffee brakes during the day whilst making jokes and keeping me sharp.

*Joep Borninkhof*
*Delft, February 2024*

# Abstract

Electric vehicles have become the focal point to reduce GHG in the quest for cleaner and more efficient means of transportation. At the core of this transition lies the key component of energy storage, the battery pack. The battery pack has electrodes manufactured with the binder PVDF. Using fluorine-rich compounds makes processing and recycling a more difficult process and it is also harmful for the environment. Therefore, alternative binders should be explored to adhere to the principles of sustainability. In this thesis, a comparative study is presented between electrodes fabricated with fluorine free polymeric binders and PVDF. Moreover, a battery cell solely constituted of fluorine free components is fabricated and tested. By using the analysis techniques electrochemical performance testing, electrochemical impedance spectroscopy and scanning electron microscopy the effect of the binders and electrolytes on the electrode performance is explored. The findings reveal that during rate performance cycling, graphite half cells based on the binder PAA demonstrated the highest discharge capacities at C-rates up to 4C with a capacity retention of 39%. NMC811 half cells based on a composite binder CMC/SBR achieved the highest capacity retention after 100 cycles, being 24%. All the fabricated full cells suffered from a 30-40% initial capacity depletion after the first charge, presumably originating from oxidative degradation of the electrolyte. Consequently, the highest capacity retention after 150 cycles was 14% for a PVDF based full cell. Fluorine free cells using a PAA anode and CMC/SBR cathode exhibited expected capacities with a higher overpotential.

# Contents

**Acknowledgements** i

**Abstract** ii

**Nomenclature** v

**1 Introduction** 1

**2 Literature review** 2
2.1 Lithium ion battery principle . . . 2
2.2 Lithium ion batteries in automotive industry . . . 3
2.3 Role of binder . . . 3
2.4 Fluorine free processing . . . 4
2.5 Battery components . . . 5
2.5.1 Negative electrode . . . 5
2.5.2 Positive electrode . . . 6
2.6 Polymeric binder types . . . 8
2.6.1 Polyvinylidene fluoride . . . 8
2.6.2 Polyacrylic acid . . . 9
2.6.3 Carboxylic methyl cellulose & styrene butadiene rubber . . . 9
2.7 Charging limitations . . . 10
2.8 Energy versus power density . . . 12
2.9 Inversed phase processing for electrodes . . . 12
2.10 Electrolyte salts: $LiPF_6$ and LiBOB . . . 13
2.11 Characterisation techniques . . . 14
2.11.1 Electrochemical impedance spectroscopy . . . 14
2.11.2 Scanning electron microscope . . . 14

**3 Method & Materials** 15
3.1 Electrode preparation . . . 15
3.1.1 Anode . . . 15
3.1.2 Cathode . . . 15
3.2 Cycling regimes . . . 16
3.2.1 Half cell cycling . . . 16
3.2.2 Full cell cycling . . . 17
3.3 Characterisation techniques . . . 18
3.3.1 SEM & EIS . . . 18

**4 Results and discussion** 19
4.1 Processability of the negative and positive electrodes . . . 19
4.2 Fabricating graphite electrodes . . . 20
4.3 Electrochemical characterisation of graphite half cells . . . 22
4.3.1 Rate performance cycling of graphite half cells . . . 22
4.3.2 Long term cycling of graphite half cells . . . 24
4.3.3 Fabricating NMC811 electrodes . . . 28
4.4 Electrochemical characterisation of NMC811 half cells . . . 33
4.4.1 Rate performance cycling of NMC811 half cells . . . 33
4.4.2 Long term cycling of NMC811 half cells . . . 35
4.5 Full cell electrochemical characterisation . . . 38
4.5.1 Fluorine free full cells . . . 42

**5 Conclusion** 46

**6 Recommendations** **48**

**References** **49**

**A Results** **57**
A.1 Electrochemical characterisation . . . . . 57
A.1.1 Graphite vs. lithium rate performance cycling . . . . . 57
A.1.2 Graphite vs. lithium long term cycling . . . . . 58
A.1.3 NMC vs. lithium rate performance cycling . . . . . 59
A.1.4 NMC vs. lithium long term cycling . . . . . 60
A.1.5 Graphite vs. NMC . . . . . 61

# Nomenclature

## Abbreviations

| Abbreviation | Definition |
|---|---|
| APIA | Aceton phase inversed anode |
| CAM | Cathode active materials |
| CCCV | Constant current constant voltage |
| CMC | carboxy methyl cellulose |
| CONVA | Conventionally dried anode |
| CONVC | Conventionally dried cathode |
| DTD | 1,3,2-dioxathiolane-2,2-dioxide |
| EC | Ethylene carbonate |
| EIS | Electrochemical impedance spectroscopy |
| EPIC | Ethanol phase inversed cathode |
| EV(s) | Electric vehicle(s) |
| HPIA | Water phase inversed anode |
| IPIC | Isopropanol phase inversed cathode |
| LFP | Lithium iron phosphate ($LiFePO_4$) |
| LIB(s) | Lithium-ion battery(ies) |
| LiBOB | Lithium bis(oxalato)borate |
| $LiPF_6$ | Lithium hexafluorophosphate |
| NMC811 | Lithium nickel manganese cobalt oxide ($LiNi_{0.8}Mn_{0.1}Co_{0.1}O_2$) |
| NMP | N-methyl-2-pyrrolidone |
| OCP | Open circuit potential |
| PAA | Polyacrylic acid |
| PVDF | polyvinylidene fluoride |
| SBR | styrene butadiene rubber |
| SEI | Solid electrolyte interface |
| SEM | Scanning electron microscopy |
| VC | Vinylene carbonate |

# 1

# Introduction

Environmental concerns for fossil fueled cars where answered with the introduction of Electric vehicles (EVs). EVs have become the focal point to reduce greenhouse gas emissions in the quest for cleaner and more efficient means of transportation [23]. At the core of this transition lies the key component of energy storage, the battery pack [46, 64]. However, the accelerating shift towards sustainable tech brings new environmental challenges [53]. Traditional battery tech does not come without a drawback. The battery pack has electrodes manufactured with fluorine rich components. A Commonly used binder material is PVDF which also contains a lot of fluorine. Working with fluorine-rich compounds makes processing and recycling a more difficult process [74, 47]. On top of this, it is also harmful for the environment [8]. As the demand for EVs continues to rise [6], alternative binders should be explored to adhere to the principles of sustainability [103]. The full scale incorporation of alternative binder is difficult. The reason for this is that currently used binders, for example PVDF, have a positive influence on the electrochemical and structural characteristics of the battery electrode[74, 47]. Hence, a simple swap to a sustainable binder does not suffice. Careful selection of fluorine free binders is needed [54], which would have matching properties, and preferably better properties.

This thesis presents a comparative study between electrodes fabricated with fluorine free polymeric binders and electrodes fabricated with PVDF as a binder. In addition, the electrolyte salt LiBOB will be used as the fitting fluorine free electrolyte salt. Consequently, a full cell configuration, which is fluorine free, will be tested and evaluated.

In this thesis, the main research question that will be addressed: "Are there viable alternatives for fluorine rich batteries?". To achieve this, a broad literary study will be performed. Simultaneously, process of anode and cathode manufacturing and electrochemical testing of batteries with alternative binder systems will be performed. Then, the fluorine free electrolyte salt LiBOB will be tested against conventional electrolyte salt $LiPF_6$. After evaluation, the best performing electrodes will be coupled, together with the LiBOB electrolyte, in order to achieve a fluorine free battery. Consequently, electrochemical testing will be performed on the fluorine free battery.

# 2

# Literature review

## 2.1. Lithium ion battery principle

A lithium-ion battery (LIB) is an electrochemical cell which can store chemical energy and release this energy in the form of electrical energy through redox reactions. This is a reaction in which one species gets oxidised by losing an electron, and the other gets reduced by gaining an electron and thereby completing the redox reaction. A general example of such a cell can be seen in figure 2.1. The cell consists of a positive electrode containing a lithium metal oxide, a carbon based negative electrode, a separator and an electrolyte salt dissolved in an organic solvent. [60]. The main purpose of the electrolyte is to provide ionic transport from one side to the other. The separator acts as an physical barrier, only providing passage for lithium ions. Electrons are blocked by the separator to prevent a short in the battery and hence can only flow through the external circuit to the other side of the battery [62].

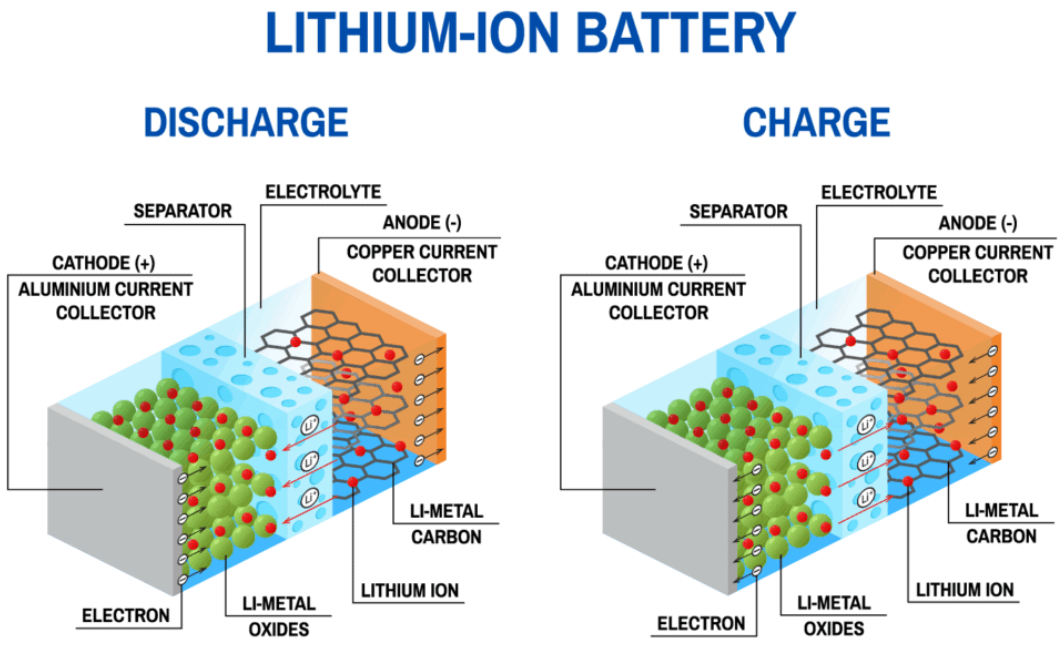


**Figure 2.1:** Schematic lithium ion battery working principle [79].

Upon charging a LIB, positively charged lithium ions transfer from the cathode side through the electrolyte to the anode side, while negatively charged electrons move through the external circuit to the negative electrode and recombine with the li-ions at the active material of the anode [84]. This process is reversible by discharging the battery again and thereby powering an electrical device. There are various types of LIBs, but the working principle remains the same. In equation 2.1 and 2.2 an example

of the half reaction for the anode and cathode are shown, respectively. In this reaction, the transition metal(s), in this case Nickel (Ni), loses electrons through oxidation and goes from $Ni^2+$ or $Ni^3+$ to $Ni^4+$ during charging. During discharging, Ni gets reduced and gains electrons by going from $Ni^4+$ to $Ni^3+$ or $Ni^2+$ [104]. The two half reactions result in an overall reaction and is shown in equation 2.3 [71].

The half reaction at the positive electrode:

$$LiNiMnCoO_2 \rightleftharpoons Li_{1-x}NiMnCoO_2 + xLi^+ + xe^- \tag{2.1}$$

The half reaction at the negative electrode:

$$6C + xLi^+ + xe^- \rightleftharpoons Li_xC_6 \tag{2.2}$$

The overall reaction:

$$LiNiMnCoO_2 + 6C \rightleftharpoons Li_{1-x}NiMnCoO_2 + Li_xC_6 \tag{2.3}$$

## 2.2. Lithium ion batteries in automotive industry

Lithium-ion batteries (LIBs) are among the most competitive options for energy storage. They have become part of the automotive industry, serving as a reliable energy source within the powertrain of electric vehicles (EVs).[46, 64]. For this reason, EVs are gradually gaining traction in the market for commercial light-duty vehicles. However, achieving broader acceptance of EVs hinges on addressing the extended charging duration obstacle, aiming to match the refueling times of conventional internal combustion engine vehicles. The widespread adoption of vehicle electrification technology relies on the rapid progress of lithium-ion battery (LIB) technology, with an extreme fast charging public infrastructure being the key supportive system [84]. LIBs have among the highest energy densities, with the ones employing graphite anodes and nickel-rich layered oxide (e.g. NMC811) cathodes have achieved specific energies ranging from 250 to 300 Wh/kg. However, this energy density is still substantially less than petrol (around 12500 Wh/kg) [88, 17]. Putting simply a larger battery pack in a car is not possible due to volume, weight and cost constraints. Currently, charging times have significantly improved. Being around 20 minutes for 322 km of range at fast charge stations with capabilities of 50 kW and 120 kW [84]. Comparable refueling times for conventional petroleum based vehicles is possible with extreme fast charging (400 kW). This exciting proposed upgrade for fast charging enables a 322 km charge in less than 10 minutes.

However, the road to this widespread adoption is full of engineering challenges. As EVs rely on the technological progress of LIBs, good performance and a long cycle life of this energy storage method is essential. The current technology of the battery pack is where the fast charging obstacle is located [84]. Furthermore, a desire for automotive energy storage systems to be environmentally friendly produced and low cost is increasing [65].

Electrodes of LIBS contain binder material consisting of polymer material. These binder materials are an important part of the LIBs as they contribute to the overall electrochemical performance. The binder assures integrity of the structural formation and binds the conducting and active materials with the current collector. Optimizing the right formulation for the electrode configuration is crucial for the development of high performance batteries [65]. Higher charging rates introduce electrochemical and material obstacles. These obstacles have to do with transport and kinetic processes that occur during cycling of the battery. The binder imposed porous electrode structure has a great influence on the mitigation of these obstacles by aiding these transport and kinetic processes [59].

## 2.3. Role of binder

The primary function of a binder is to hold all the constituents of an electrode together. This includes the anode or cathode active material, conductive additives and the current collector [12]. Through chemical or physical interactions, these separate components are held together, maintaining the mechanical integrity of the electrode without interfering with electronic or ionic conductivity [15]. For manufacturing electrodes, polymeric binders are used, along with the appropriate solvent, to disperse the electrode active materials and form a viscous slurry. The manufacturing process of the electrode slurry has significant influence on the electrochemical performance of the produced electrode. This has to do with the active material distribution throughout the electrode and the structure of the electrode

itself [54, 7].
Polymeric binders have been recognised for its impact on cell aging, irreversible capacity loss, and coulombic efficiency (CE [9, 107]). Binders serve the purpose of linking the active materials and carbon additives, as well as securing the adhesion of the electrode slurry to the current collector, rather than contributing electrochemically. Typically, the main factor contributing to the rapid deterioration of a cell is the loss of lithium and active materials, because of dissolution, lacking interconnectivity, electrical breakdown among the electrode components and the delamination of electrode components from the current collector [18]. Using polymeric binders with the presence of reactive functional groups, such as COOH, on the polymeric binder backbone, contributes to a heightened adsorption capacity onto the surface of electrode materials through hydrogen bonding. This property proves beneficial for aiding a strong adhesive force between the binder, active materials, and the current collector [54, 68]. Using the right binder, in the optimal weight ratio compared to the electrode active material, can prove effective to prevent electrical contact loss and hinder self-agglomeration of active materials by sufficient dispersion [54].
The key requirement for binders in LIBs lies in their electrochemical stability (0-5V vs $Li/Li^+$), especially when the battery is in a fully charged state. Binders must exhibit chemical inertness towards electrode materials, electrolytes and separators. Interactions between the binder and other components inevitably give rise to new chemical reactions, ultimately leading to the degradation of electrochemical performance [54].

## 2.4. Fluorine free processing

In the current processing for LIBs, fluorine is present in the commonly used polymeric binder polyvinylidene fluoride (PVDF) and the electrolyte $LiPF_6$. For electrodes in LIBs, fluorine is incorporated due to its high resistance to oxidation. For fluorine being highly inert and having a weak polarity [99]. While PVDF and $LiPF_6$ are generally used, they have shortcomings that have to do with processing, toxicity and stability. This part will have focus on the drawback of using PVDF as a binder, a further explanation on $LiPF_6$ will be given in chapter 2.10.
Although PVDF is popular due to its attractive properties (chapter 2.6.1), excess heat produced within the cell tends to melt the PVDF binder (melting point is 177°C) [54]. At elevated temperatures PVDF reacts with $LiC_6$ and the lithium metal in an exothermic reaction to form LiF and this can cause a thermal runaway [21, 16, 56, 102]. The chance of a thermal runaway could be avoided by substituting PVDF with a non-fluorinated binder [16, 102]. In addition, some other disadvantages are the use of a organic solvent, such as N-methyl-2-pyrrolidone (NMP). NMP is toxic and can cause carcinogenic and negative reproductive effects. It has strict humidity control during processing and needs to be fully recovered in electrode production. Also, PVDF is difficult and costly to dispose at the end of life of the LIBs [65, 16, 29, 46, 73, 102].
Moreover, the European Union (EU) has already started to put restraints on the use of NMP. According to Annex XVII:REACH (Regulation concerning the Registration, Evaluation, Authorisation and Restriction of Chemicals; EU) states that from May 9th 2020 on *"NMP shall not be used as a substance on its own or in mixtures in a concentration equal to or greater than 0.3% unless manufacturers and downstream users take the appropriate risk management measures and provide the appropriate operational conditions to ensure exposure of workers is below the Derived No-Effect Levels (DNELs) of 14.4 mg/m$^3$ for exposure by inhalation and 4.8 mg/kg per day for dermal exposure"* [66].
Water soluble binders, or aqueous binders, are found to be incorporated as a fluorine free binder substitution for PVDF in electrodes. Recently, Yuan et al. conducted a life cycle assessment on the manufacturing of water-based LIB's. Here, they stated that the specific energy consumption was 43% lower for water-based electrode processing compared to that of NMP-based electrode processing considering realistic electrode conditions (2 mAh/cm$^2$ and 35% porosity) [103]. Also, using aqueous binders has a lower impact potential on global warming than NMP based binders. Although a higher solid content is achievable, for this assessment, only 35% solid content was assumed. Meaning that a higher reduction of the global warming potential is possible by reducing the amount of water and therefore the drying energy [49, 103].
Another advantage of water soluble binders over PVDF is their moderate swelling ability in electrolytes based on carbonate [54]. In a basic electrolyte swelling test, conducted by Jeschull et al., the degree of swelling for the PVDF and the fluorine free and aqueous binders styrene butadiene rubber (SBR),

carboxymethyl cellulose (CMC) and polyacrylic acid (PAA) among others was estimated. The degree of swelling was quantified as the mass ratio between swollen and pristine polymer films. After soaking in 1M $LiPF_6$ in EC:DEC (1:1) for three days, fluorine containing polymers were found to be swollen the most, with around a 60% mass increase. SBR and CMC around 20% mass increase and PAA denoted a negligible increase in mass [40]. Furthermore, a cost comparison already promotes the use of aqueous binders by being cheaper than the conventional PVDF-NMP combination [54]. Compared to water (0.015 $/kg), NMP is quite costly being 1–3 $/kg. While aqueous binders are often in the range of 2–5 $/kg compared to PVDF with 8–10 $/kg [8, 15]. Hence, there is a strong interest in the current Li-ion battery research and industrial battery production community to substitute these components with more cost-effective, environmentally friendly solvents and binders that are also less toxic. Using water as a solvent has the potential to lower the manufacturing expenses of electrodes and lessen their environmental footprint. However, this approach introduces distinctive hurdles for cathodes, including the potential for the dissolution of lithium and transition metals from the active material, as well as corrosion of the current collector [32, 73, 46, 102].

## 2.5. Battery components

### 2.5.1. Negative electrode

For the negative electrode, graphite has been exclusively used in lithium ion batteries. Using graphite for the anode of the battery has several benefits. These have to do with its high specific capacity (372 mAh/g), low operating potential (0.1 V vs. $Li/Li^+$), long cycle life, low cost, high abundance and environmental friendliness [105, 101]. Graphite will be the main choice until a better candidate is found, however, alternatives such as silicon are still not ready for practical application [101]. When graphite is lithiated, $Li^+$ is transfered into graphite. The positive ions are stored in the host lattices of the material and settles in the middle of the Van der Waals space between graphite layers [69, 2]. The creation of Van der Waals spaces is possible due to the weakness of the Van der Waals interaction, which allows cohesion between graphite layers themselves, and enables the layers to move apart. This in turn allows for Li-intercalation due to a Li-ion concentration gradient at the surface of the active material, creating a driving force into the graphite. With each extra $Li^+$ that is stored the graphite layers shift and eventually form a phase [2]. This process can also be seen in figure 2.2, from left to right.

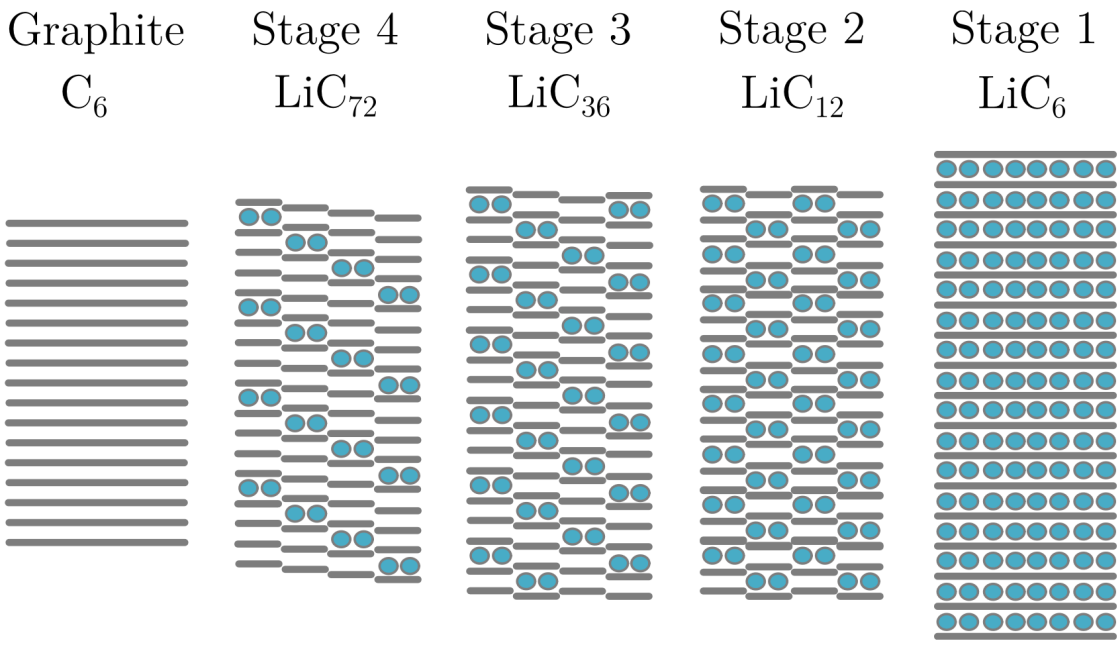


**Figure 2.2:** Intercalation state of Li into graphite [69].

**Solid electrolyte interphase**
To ensure lithiating and delithiating remains a stable and reversible process, a passivating film needs to be formed on the surface of the negative electrode. This film needs to be chemically and mechanically stable, electron insulating and lithium-ion conducting [101]. During the initial cycles of a Li-ion battery cell, a protective layer forms at the surface of the negative electrode called the solid electrolyte interphase (SEI) due to reductive side reactions. Lithium ions can transfer through this layer, however, electrons cannot. Because of the formation of this SEI, charge is lost and is referred to as irreversible charge consumption [24, 60]. The origin of this charge consumption is because the Li-ions react with the reduced electrolyte constituents, thereby resulting in electrolyte side products containing lithium [3]. Consequently, loss of the lithium inventory from the cathode negatively affects the energy density. A well formed SEI should have high $Li^+$ conductivity and low electron conductivity. Further SEI formation on the graphite surface is prevented because of the electron insulating property which would otherwise allow for the electrolyte reduction. The high ionic conductivity of the SEI layer allows for the permeation of Li-ions to the surface of the graphite and facilitates pathways for intercalation [3]. Li-ion loss in the electrolyte lowers the mass transport in the liquid phase and increases the resistance in the electrolyte, resulting in a lower power density. In addition it also affects the cycle life, self-discharge characteristics and rate capability. During the first cycle, 10% of the original available capacity is lost due to the irreversible charge consumption [4, 60].
Novak et al. proposes a simple model in figure 2.3 to distinguish three voltage levels of charge consumption. The first one associated with the reduction of the graphite surface groups around 3 and 0.8 V versus Li/Li+. The second one associated with the SEI formation through the decomposition of the electrolyte between around 0.8 and 0.2 V. The third one associated with the side reactions alongside the reversible intercalation and de-intercalation of lithium ions corrosion-like reactions of $Li_xC_6$ which contribute to the growth of the SEI film between around 0.2 and 0 V [60].

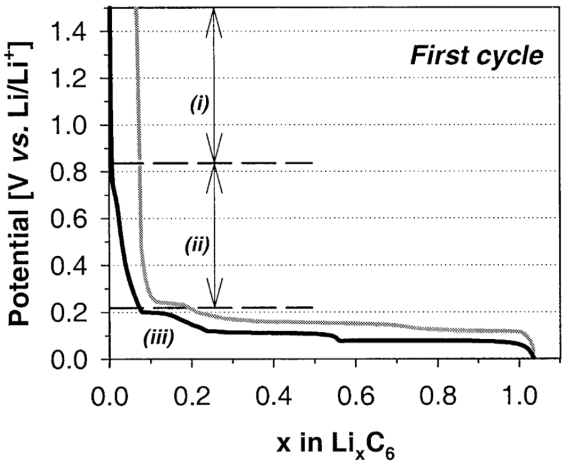


**Figure 2.3:** First charge & discharge voltage curve of a graphite electrode at C1/40 [61].

## 2.5.2. Positive electrode

Unlike the almost predestined choice of material for the negative electrode, various alternatives (NMC532, LFP & LCO) for positive electrodes exist for the various applications they are used for. However, in the field of battery research and large-scale battery production, the incorporation of nickel-rich cathode active materials (CAM) has gained significant importance, with one of the most promising being $LiNi_{0.8}Mn_{0.1}Co_{0.1}O_2$ or the more common used expression NMC811. The incorporation of nickel rich cathode active materials is primarily aimed at boosting the specific capacity of the positive electrode, thereby elevating the overall energy density of the battery. NMC811 has a high specific capacity of 200 mAh/g when charged up to 4.2 and operating potential of 3.7V [39, 57]. However, as the nickel content increases, the CAM becomes increasingly susceptible to moisture and is more prone to reacting with water, resulting in a loss of activity and stability. This complicates the transition from NMP-based to

water-based electrode manufacturing [73].
For processing cathodes, aluminium current collectors are used. Aluminium is stable in the pH range of 4 to 9, according to the Pourbaix diagram [74]. Corrosion can occur at the surface if the pH is not controlled properly[73, 67, 46, 32, 49]. This oxidation can form hydrogen, which in turn can crack and deform the dried electrode slurry. Oxidation is possible due to the high alkaline properties of NMC811 when being processed with water (because of aqueous binders), the pH of the solvent-bases slurry can rise to a pH of 12-13. This increase is also referred to as Li-Leaching. In this process, the Li on the surface of the NMC811 is replaced by $H^+$ and forms LiOH. This reaction predominantly takes place at the particle surface, leaving the particles in the bulk unaffected. However, a decrease in the amount Li content of the cathode active material is the result of the interaction between the lithium and the hydrogen and reduces the overall capacity of the battery [73, 49, 47]. For this reason, when using neutral binders, an acidic component, such as phosphoric acid, nitric acid, citric acid or acetic acid could be added to lower the pH of the electrode slurry [73, 49]. Currently, PVDF continues to serve as the primary binder for the positive electrodes, and a complete adoption of an alternative aqueous binder has not been accomplished [37].

## 2.6. Polymeric binder types

Below in table 2.1 an overview on the pros (advantages) and cons (disadvantages) of fluorine free polymeric binders used for electrode fabrication is provided. Based on the pros and cons of the binders in the overview, a selection was made for the electrode fabrication in this research. Polyacrylic acid (PAA) and polyethersulfone (PES) were chosen for the negative electrode. PAA had in general good reported properties and is able to be processed with water. Despite PES not being researched that much for electrode fabrication, it was reported on phase inversion electrode fabrication. This made it interesting to research its potential further. The composite binders carboxylic methyl cellulose & styrene butadiene rubber (CMC/SBR) and CMC/PAA and only PAA were chosen for the fabrication of the positive electrodes. CMC/SBR is an often researched aqueous binder combination on which promising properties were reported. The aqueous binder combination CMC/PAA is reported to be used for thicker positive electrodes, which made it an attractive composite binder. PAA was also chosen for cathode fabrication due to the good adhesive properties with the cathode active material. PVDF was used as the positive control binder for both the negative and positive electrodes. The chemical structure (figure 2.5) and further elaboration on the properties of PVDF, PAA and CMC/SBR can be found below the table.

| Binder | Pros | Cons | Ref |
|---|---|---|---|
| Polyacrylic acid[b] | Aqueous binder, helps protection from aluminium corrosion, good dispersant and adhesive properties due to hydrogen bonding | Lower adhesion to graphite compared to PVDF | [48, 15, 54, 64, 74] |
| Carboxylic methyl cellulose[a] | Aqueous binder, good dispersant, good adhesive and mechanical properties, inexpensive | Brittle and stiff | [48, 77, 15, 54, 64, 74] |
| Styrene butadiene rubber | High thermal stability, good mechanical and flexible properties | Prone to oxidation at higher voltage | [15, 54, 74] |
| Polyethersulfone | High mechanical strength, hydrophilicity | Organic solvent (e.g. NMP), low amount of research | [87] |
| Alginate-based binder | Aqueous binder, high binding strength, crosslinking properties, good mechanical properties | Varying performance reported | [77, 54, 15] |
| Guar gum | Ability to promote $Li^+$ transfer, mechanical tolerance to dramatic volume expansion | Low amount of research | [54] |
| Chitosan | Good adhesion, able to copolymerise | Lower performance for anodes, low amount of research | [54] |

**Table 2.1:** Overview of the pros and cons of fluorine free binders. [a]Commonly used in combination with styrene butadiene rubber. [b]Sometimes combined with CMC to create thick electrodes.

### 2.6.1. Polyvinylidene fluoride

Polyvinylidene fluoride (PVDF) is a widely used polymeric binder for LIBs. Properties that make it so popular are the great electrochemical stability and the adhesive properties to the active material and current collector [21, 16, 56, 73, 46, 102]. Using PVDF as a binder gives a high binding strength, however it shows low flexibility. This low flexibility during cycling can easily induce a decrease in the battery cycle life. Due to consequent expansion and contracting of the active and graphite material the bond between active materials may break upon cycling [29].

### 2.6.2. Polyacrylic acid

PAA is a water soluble binder that provides high adherance to the copper current collector. The adherance is a property coming from its hydrogen bonding carboxyl groups [54]. Furthermore, graphite electrodes using PAA as a binder have a lower heat evolution compared to CMC/SBR and PVDF based electrodes [64]. Polymeric binders also have an effect on the deformation of graphite and its thermal stability when applied in anodes of LIBs [65]. Park et al. applied different roll-press pressures on different electrodes made with the binders PVDF, PAA and a composite binder of CMC/SBR (1:1). Figure 2.4 shows the electrode density with increasing pressure. The ability of a binder being able to withstand higher pressures, results in a higher porosity content within the electrode structure. The ability of PAA being a more rigid polymeric binder, compared to CMC/SBR and PVDF, and therefore maintaining better the porous structure, results in better electrochemical performance in PAA based electrodes [65].

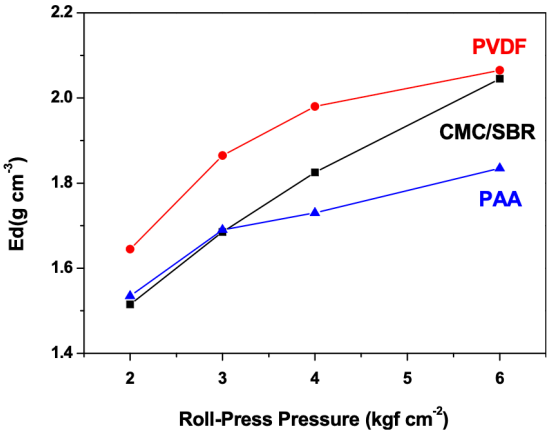


**Figure 2.4:** Densities of graphite electrodes made with different binder as function of the roll-press pressure [65].

PAA contains -COOH functional groups, giving it weak acidity, which can potentially reduce the alkalinity of the water-based slurry during preparation and makes the pH drop below 9. [73, 67, 48, 47]. Moreover, alike in negative electrodes, PAA has good binding properties due to the hydrogen bonds it can form with most inorganic powders, simultaneously acting as electrostatic dispersants by adsorbing to the charged active material particle surfaces, and due to crosslinking originating from the hydrogen bonds between the carboxylic groups [47, 48, 100, 15]. Furthermore, in theory, the carboxyl groups in PAA could facilitate the dispersion of most oxides, suggesting that it might enhance the overall dispersion of the water-based slurry [47, 67].
PAA with a low molecular weight lacks the ability to provide the necessary rheological properties for the slurry preparation and adequate mechanical strength for the dried electrode. As a result, a high-molecular-weight PAA (greater than 200,000 g $mol^{-1}$) is essential [47, 54].

### 2.6.3. Carboxylic methyl cellulose & styrene butadiene rubber

Carboxylic methyl cellulose is a polymeric derivative of cellulose. And is, through the substitution of some -OH groups for carboxymethyl groups ($CH_2COOH$), made water soluble [8]. CMC has the potential to replace PVDF as a binder for positive electrodes [37]. It can provide high mechanical strength and is stable towards oxidation. However, as an electrode binder it is brittle and inelastic. For this reason styrene butadiene rubber is added [38, 100]. SBR is flexible and suppresses crack formation in the electrode and also possesses a stronger binding force and a higher heat resistance capability than the commonly used PVDF. [100, 9]. Although CMC is stable towards oxidation, it should be noted that SBR is able to oxidise when exposed to higher voltages (>4.3 V vs. $Li/Li^+$) [100, 37]. Moreover, similar to PAA, the mixture of CMC/SBR acts as an effective dispersing agent for the CAM in the electrode slurry mixture and also demonstrates good adhesion onto Al foil [100, 37, 40]. While the carboxyl groups adsorb to the charged active-material particle surfaces and act as electrostatic dispersants [48, 100].

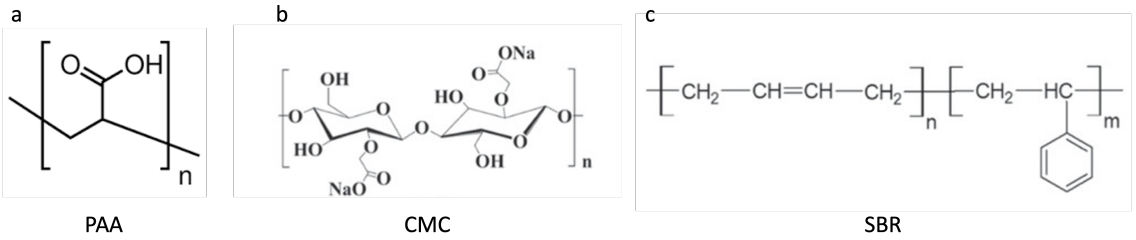


**Figure 2.5:** The chemical structure of the polymeric binders polyacrylic acid [19] (a), carboxymethyl cellulose [63] (b), styrene butadiene rubber [63](c).

## 2.7. Charging limitations

Obviously, there are limitations due to several thresholds when charging and discharging a battery. These thresholds mainly have to do with the applied current density and the operating voltage a certain electrode can support. Above the threshold, the highest achievable capacity decreases exponentially. Several factors influence the amount of power a battery can deliver, or store at higher current densities. This has to do with the electrode, the electrolyte and the separator [81]. When considering a different polymeric binder for an already optimised system, the most important aspect is that this new binder contributes to the electrode performance at least as well as the current prevailing polymeric binder. The binder has a great influence on the structure morphology and integrity and the dispersion of the active material of the electrode. Therefore, it is important that at higher rates this new binder can keep the electrode structure intact.

It is important to identify the factors that increase the degradation rate of a polymeric based structure at higher performance rates. These factors include: mechanical expansion and contraction due to high or low $Li^+$ content inside the active material, heat generation accelerating unwanted side reactions and Li plating at the anode side due to low ionic transport [35]. A brief explanation on these factors and how they can be mitigated follows below:

**Mechanical stress**. When Lithium ions intercalate into the graphite structure, each intercalation induces an expansion in the local structure. At fully charged state, the volume expansion of the graphite is 10% [69]. In figure 2.2 you can see this increase clearly. At higher current densities, a binder with strong adhesive properties to the active material and the current collector can prevent cracks and loss of contact between the active material and the current collector.

**Heat generation**. Heat generation in an electrode predominantly caused by overpotential needed to drive the electrochemical reaction. The overpotential is the added up effect of various energetic barriers, such as the resistance of the charge transfer at the solid/electrolyte interfaces and diffusion limitations in the active materials and the electrolyte. Meaning that the mass and kinetic transport limitations are directly related to the heat generation [35]. Consequently, mitigation can be done by providing a binder induced polymeric structure that allows for high kinetic and mass transport within the electrode.

**Lithium metal plating**. The process of intercalation is determined by migration and diffusion through the electrolyte phase and diffusion in the active material of the anode [84]. The latter diffusional process occurs quite slow and as batteries are to be charged at increasingly faster rates, an increase in current rates give rise to a mismatch between the transport rate through the electrolyte and the lower intercalation rate at the anode. However, with increasing electrode thickness, the lithium diffusion in the electrolyte phase has a bigger impact and becomes rate limiting [48]. For both rate limiting diffusional processes, it increases the overpotential, driving the electrode potential below the $Li/Li^+$ redox potential (0V)[35, 84, 57, 72]. Eventually resulting in lithium metal plating at the anode [10]. Plated lithium does not take part in the electrochemical reactions, resulting in capacity loss [26, 84]. Plating is more likely when the capacity ratio between the anode and cathode is lower than 1.1. Having a Li cathode inventory equal, or larger than equal, will probably drive the reaction beyond the capacity of the anode, resulting in plating. Furthermore, plating is also more likely when pores in the separator become more narrow and lead to the formation of concentrated current hot spots, leading to

a significant overpotential [84, 35]. After prolonged metal plating, lithium metal dendrites may form. These dendrites are able to puncture the separator and over time eventually cause a short circuit, build up of heat or even a fire. A cut-off voltage can prevent plating. However, this still results in capacity loss because of the smaller operating potential window. Mitigating the reduced capacity, can be done by for example decreasing the electrode thickness or by increasing the electrode porosity [81].

NMC811 has the advantage of a larger available capacity over other nickel-rich layered oxides, but their capacity and voltage fading rate is higher compared to these other layered oxides. Consequently, care has to be taken at the high state of charge (SOC) regions. Capacity fade is more severe when charging beyond 4.2V vs $Li/Li^+$ [42]. Märker et al. reports at this stage of charging (70% SOC) a sudden collapse in the crystal structure is observed. At a SOC of 75% the lithium layer spacing collapses and consequently a decrease in Li vacancy ordering and Li mobility is the result. The remaining fraction of capacity related Lithium is therefore not available any more. Over prolonged cycling this process could result in particle crack formation [57].
In figure 2.6b, a differential capacity plot of the first charge and discharge cycle of a lithium/NMC811 half cell is shown. This cell demonstrates a capacity, at full charge, of 240 mAh/g when cycled between 3 and 4.4V vs $Li/Li^+$. The four regions, I, II, III and IV correspond to the capacity contribution of the charge and discharge. The majority of the capacity is gained in region I to III as region IV contributes less than 20 mAh/g. Figure 2.6a shows the first charge and discharge cycle and region IV starts after 4.2V. Mitigation of the said capacity loss can be done by cycling up to a cut-off potential of around 4.2, as the majority of the capacity will be maintained, while preserving the mobility of lithium ions in the positive electrode. However, opting for this lower cutoff voltage diminishes the accessible capacity and thereby eliminating one of the benefits associated with the use of NMC811. Staying in this voltage range would allow for higher charging rates and keeps out significant drawbacks such as uneven lithiation throughout the electrode or heat formation [57].

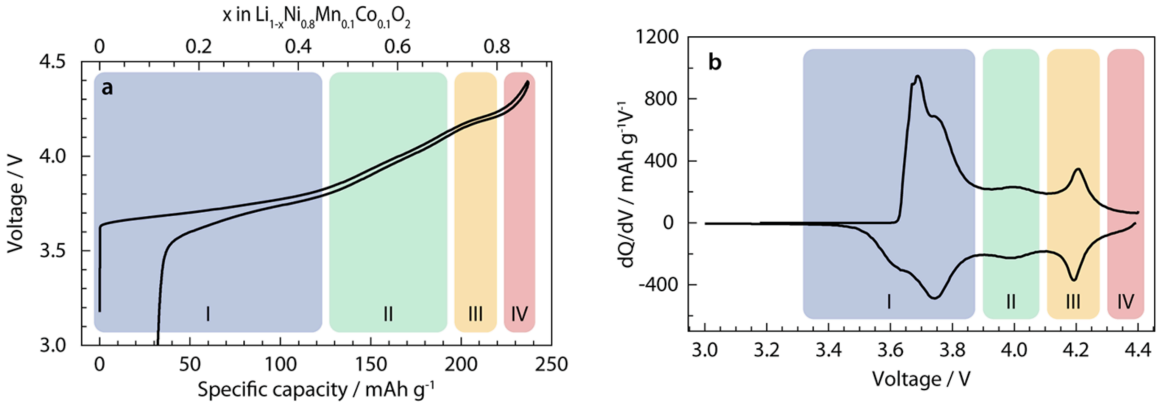


**Figure 2.6:** The first charge and discharge cycle voltage curve of a Li/NMC811 half cell (a) and the corresponding differential capacity plot (b) [57].

Conductive additives are often added to the formulation of the anode and cathode electrode to allow for enough electronic conductivity and lower ohmic resistance. On the cathode side, this mainly has to do with the low conductivity the cathode active material possesses. For the anode side, graphite is conductive, but not sufficiently. The conductivity has great influence on how fast a battery cell can be charged and discharged. Otherwise the overpotential will increase due to the increased current densities. For the conductive additive to aid good conductivity, dispersing of these agents is very important and this is governed by the properties of the binder. Carbon black is an often used conductive additive and is carbon based as the name already suggests [35].

With these limitations in mind, various experiments can be performed in order to test these limits. Electrical impedance spectroscopy (see chapter 2.5.1) measurements can be done to allocate the resistive bottleneck(s) of the system and rate capability tests can be carried out to determine the extent to which rate current an electrode can be charged for which it is still beneficial to the performance of the cell.

A rate capability test is an experiment in which the current density of charging and discharging is set and becomes incrementally higher at different cycles. Starting for example at 0.1C and ending at 4C. The increase in rate can be done for the intercalation step, but also for the deintercalation step. In the latter benefitting from the absence of lithium metal plating on the anode surface.

## 2.8. Energy versus power density

There is a trade off between the energy and power density in a battery cell and this can be tuned by altering the electrode density. On the one hand, a higher energy density is desired to minimise the volume a battery pack requires. For this, the areal capacity should be maximised. On the other hand, a large enough power density is desired for the battery to deliver a high enough charge and discharge rate, for which a lower areal capacity is wanted.
Electrode density primarily emphasises achieving a balance between electron transport within the electrode and ion transport through the pores filled with electrolyte. However, in electrodes with high loading, the density becomes a crucial factor in the trade-off between power and energy during the design process [49]. This is because with increasing electrode thickness, the diffusion limited ionic resistance increases exponentially. Limiting the ion transport through the electrode's intricate porous structure, leading to a lower electrochemical performance and to a large reduction in energy and power capabilities. To obtain a high areal capacity, you would want an as thick as possible electrode, as this increases the overall energy density in a battery pack. However, this is limited by whether the battery performance meets the power requirements of the battery for a certain application [31, 45]. Furthermore, the fundamental principle behind designing high-power cells is to either enhance the active interface area between electrodes and electrolyte or reduce the overall distance for charge transport between electrodes. However, the decrease in resistance to aid high power output also increases the self-discharge rate. Consequently, the reduction in resistance intended for high-power operation can result in an elevated self-discharge rate [49].
Other common strategies for increasing battery performance are oriented towards lowering porosity, and minimizing the volume proportion of non-active constituents, consequently elevating the active material's volume fraction [45]. To alter the density of an electrode, the electrode is calendered to decrease the porosity. There is an optimal porosity, around 35%, for which the diffusion length of the Li-ions in the liquid electrolyte and conductivity of the electrode is balanced. However, lower porosities (20-25%) can be found in commercial grade electrodes. In the commercial ones, the cell-level volumetric energy density is of greater importance [49]. For calendering anodes, the graphite particles have better mechanical properties which allow them to be calendered to a lower porosity compared to cathode electrodes without risking disintegration or particle fracture. A lower porosity gives a lower internal electrode surface area, resulting in a thinner electrode with a higher energy density and allowing for a lesser amount of electrolyte used, which also saves costs [49].

## 2.9. Inversed phase processing for electrodes

In this thesis, a novel method is being applied in the production process of the Li-ion battery electrodes, the so-called phase inversion treatment or method. In the phase inversion method, before drying the casted electrode in an oven, the anode or cathode is immersed in an anti-solvent bath for 5 seconds. This leads to a thermodynamically unstable system. By doing this, you get a two phase system. A polymer-rich solid phase, which becomes a membrane structure, and a polymer-poor liquid phase, which induces the pore formation in the polymer membrane [30]. In figure 2.7 a schematic of this process is shown. However, in this case longer immersion times were used which results in a delamination of the electrode.
Harks et al. states that the kinetics involved are affected by the exchange rate of the anti-solvent in, and solvent out of the casted electrode, which in itself depends on several factors such as the miscibility and the molecule size of the solvents [31]. The induced phase separation generates an alternate binder precipitation process which generates a high porosity profile. The porosity profile is long and connected, because the anti-solvent diffuses all the way from the top to the bottom of the electrode. As a result, a higher power output and good binding characteristics between the active materials of the electrode are obtained [86, 31]. In the conventional drying process (no anti-solvent), the pore formation is a much more random process that occurs through the (slower) vaporisation of the solvent [30].

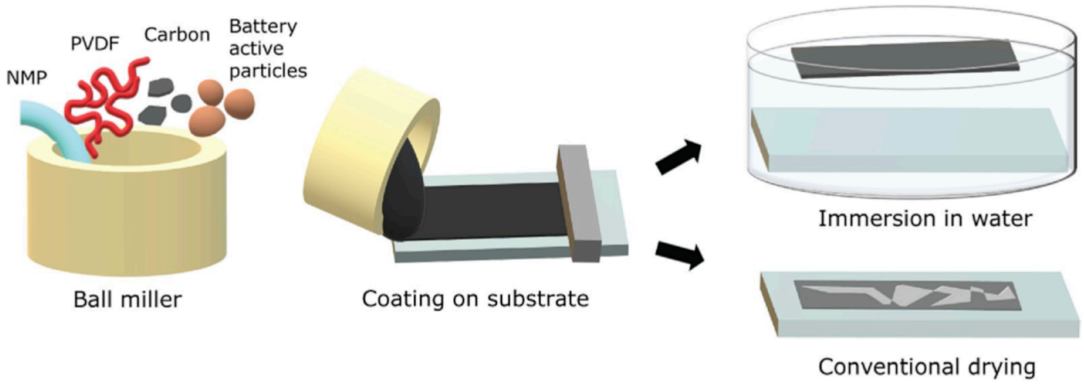


**Figure 2.7:** Schematic processing of phase inversed electrodes [30].

## 2.10. Electrolyte salts: $LiPF_6$ and LiBOB

In LIBs, the electrolyte accommodates the Li+ transfer between the positive and the negative electrode. The electrolyte is a key component, having a huge impact on the overall battery performance. However, it is not directly participating in the redox reactions for charge storing or either the capacity or the voltage of a battery [34].

Electrochemical reactions fundamentally rely on the compensation of positive charges via ionic currents. Having an electrolyte that accommodates ion transfer quick and efficient is key. Given that ion transport shows considerably slower rates compared to electron transport, the power output of a system is dependent on the ion transport rate of the electrolyte [34].

Additionally, the electrolyte itself possesses mass, volume, and cost considerations, hence giving substantial impact on not only the battery's performance but also on the volumetric and gravimetric energy densities, as well as the overall cost of energy storage. Although the electrolyte is not directly involved in the aforementioned charge storing redox reactions, it does contribute to redox side reactions [76, 34].

A variety of electrolyte chemistries are being used for the ionic transport inside the active material of electrodes, however, the composition relatively remains the same, typically consisting of a solution containing the salt $LiPF_6$ dissolved in a blend of organic carbonate solvents. Moreover, the incorporation of fluorine appears to be a necessity in highly performing electrolyte systems, not only as fluorinated anions, but also electrolyte additives and as co-solvents aimed at enhancing their functionality. The reason for this is the high electronegative nature of fluorine, making it very stable towards oxidation [85]. $LiPF_6$ provides excellent ionic conductivity, along with the quasistable electrochemical stability (important for SEI formation). However, the use of fluorine in electrolyte solutions gives rise to several concerns. It is sensitive to high temperature operations [75, 90] and also toxic [83] which in turn gives rise to further concerns which have to do with environmental en occupational safety issues through the lifecycle of LIBs [34].

Replacing $LiPF_6$ for fluorine free electrolyte salts demands that these salts provide good conductivity. One of the most promising and researched electrolyte salt is LiBOB [94, 95, 96, 97, 98]. Research was predominantly focused in the combination with graphite anodes. LiBOB contains the anion bis(oxalato)borate (BOB). With this salt, high ionic conductivity and solubility can be achieved because the carbonyl groups withdraw the electrons which helps delocalise the charge and in turn induces dissociation of the salt in organic solvents.

Comparing LiBOB against $LiPF_6$ gives the following insights. The main limitation from the LiBOB salt is the lower solubility in carbonate solvents and higher cell resistance due to the lower conductivity [50, 33]. However, these shortcomings are surpassed as LiBOB based electrolytes are able to form an oxygen rich and stable SEI [94, 33], have a lower reactivity in lithiated graphite and are able to passivate the aluminium current collector just as $LiPF_6$ based electrolytes are [98, 41], LiBOB has more favourable and less toxic byproducts (e.g. $LiBO_2$ and LiOOCCOOH) which are less harmfull, LiBOB also has a higher thermal stability and a higher water tolerance [34, 41]. In addition, LiBOB has been classified as biodegradable by the European Chemicals Agency [1].

Due to instabilities at the lower potentials associated with anode materials, such as graphite, the electrolyte must possess the capability to form a protective layer (the SEI). This can be achieved by the incorporation of ethylene carbonate (EC) within the solvent blend [34]. Fluorinated compounds such as LiF originating from fluorine containing salts have been identified as stabilising SEI components and play part in increased battery performance [51, 44].
Other means for enhancing the SEI stability can be done by electrolyte additives. In this research additive variants are considered: vinylene carbonate (VC) and 1,3,2-dioxathiolane-2,2-dioxide (DTD). VC has the ability to successfully enhance the stability of carbon based electrodes due to its ability of radical polymerisation on the lithiated anode surface which surpresses electrolyte anion and solvent reduction. Furthermore, addition of VC decreases the irreversible capacity and improves the cycling performance and thermal stability of the Li-ion battery [93, 28, 22, 5]. DTD in turn enriches the SEI with sulfide components. These components allow for a stable SEI formation, resulting in a uniform $Li^+$ deposition on the SEI. Also, it has a beneficial effect on the degradation of the electrolyte salt, which could lead to improved lifetime [93, 36].

## 2.11. Characterisation techniques

### 2.11.1. Electrochemical impedance spectroscopy

Electrochemical impedance spectroscopy (EIS) is a characterisation technique used to obtain the resistive and capacitive electrochemical properties at a certain frequency. This method applies an alternating potential at different frequencies to the electrochemical system and assesses changes in alternating current, phase shift, and amplitude. Distinct observation of different chemical processes taking place at different rates is possible due to the variation in frequencies, ranging from 10 kHz to $10^-5$ Hz. The high frequency region (10k - 100 Hz) is related to migration of ions in the bulk and thus the electrolyte resistance, the medium frequency region (1000-10 Hz) is related to the charge transfer resistance (+ double layer capacitance) and the low frequency region ($10^-2$ - $10^-5$ Hz) is related to the diffusion resistance (+ chemical capacitance) [25]. The resulting impedance is comprised of complex numbers, with a real (Re(Z)) and a imaginary (Im(Z)) part. The real part representing the resistance. A way to visualise the experimental EIS measurements is by using a Nyquist plot and it is constituted of several elements such as the Re(Z), Im(Z) [82].

### 2.11.2. Scanning electron microscope

Scanning electron microscope (SEM) is a characterisation technique used to obtain information about the composition and provide a topographical image of the analysed material. The technique collects backscattered electrons to abtain information about the local composition while also collecting secondary electrons to provide an image of the material up to nanometer level [15]. Surface morphology changes, such as the formation of an SEI layer, can observed through post mortem SEM images.

# 3

# Method & Materials

In this chapter, an elaboration on the negative and positive electrode preparation will given in chapter 3.1. Then, the cycling regimes will be explained in chapter 3.2 and lastly a short explanation on the used characterisation technique will be given in chapter 3.3.

## 3.1. Electrode preparation

### 3.1.1. Anode

The negative electrode consists of the ingredients graphite (SLS 30, Imerys), Carbon Black (Super C45, TIMCAL) and a polymeric binder. The binder was either polyvinylidene fluoride (PVDF, Syensqo) or polyethersulphone (PES, Goodfellow) or poly acrylic acid (PAA, Sigma Adlrich). For PVDF and PES 2 N-Methyl-2-pyrrolidone (NMP, Acros Organics) was used and for PAA water was used as a solvent.
First, a mixture of the graphite, Carbon black and the binder was made with a weight ratio of 90:5:5, after which the solvent was added. The solvent had a solvent to polymer weight ratio of 14:1 for NMP and 22:1 for water. Then, the mixture was stirred for an hour with a top stirrer (IKA) using a holed paddle blade at 1000 rpm. After mixing, a homogeneous slurry was obtained. Two separate casting were made for each binder type. They were casted on separate copper electrode sheet ($d_{Cu} = 14\mu m$) with a doctor blade. The height of the doctor blade was set to $200\mu m$ for PAA and 200 or $250\mu m$ for PVDF, this depended on the desired loading of the electrode. Then, one of the two castings was left to dry by air. The other casting was subjected to a phase inversion step, after which it was left to dry by air. Water and acetone were used as the anti-solvent for the slurries containing PVDF and PAA, respectively. The casted electrodes were then dried in an oven at 70 °C. After half an hour, the casted electrodes were put in a vacuum oven at 60 °C and 10mBarA for 16 hours.

### 3.1.2. Cathode

The positive electrode consisted of the ingredients NMC811 (Umicore), graphite (SLS 30, Imerys) or KS4 (Imerys) for PVDF, carbon black (Super C45, TIMCAL) and a polymeric binder. The binder was either PVDF, PAA, a mixture (1:1) of carboxymethyl cellulose and styrene butadiene rubber (CMC, Sigma Aldrich/SBR, Targray) or a mixture (3:1) of CMC and PAA (CMC/PAA). NMP solvent was used for PVDF and water for PAA, CMC/SBR and CMC/PAA.
A mixture of the NMC, graphite, carbon black and binder was made with a weight ratio of 92:1:3:4 for PVDF, 94:1:3:2 for CMC&SBR, 94:1:2:3 for PAA, 93:1:2:4 for PAA&CMC. The corresponding solvent was added with a solvent to polymer weight ratio of 14:1 for PVDF, 30:1 for PAA, 12:1 for CMC&SBR and 20:1 for PAA&CMC.
Then, the mixture was stirred for an hour with a top stirrer using a holed paddle blade at 1000 rpm. After mixing, a homogeneous slurry was obtained. Two separate castings were made for each binder type, they were casted on a separate aluminium electrode sheet ($d_{Al} = 11\mu m$) with a doctor blade. The doctor blade was set to a height between 150 and $200\mu m$ for CMC/SBR, $100\mu m$ for PVDF and $250\mu m$ for PAA and CMC/PAA. The height difference depended on the electrode loading that would be obtained. Then, one of the two castings was left to dry by air. The other casting was subjected to a phase inversion step, after which it was left to dry by air. Water, acetone and isopropanol were used as the anti-solvent for the slurries containing PVDF, PAA, CMC/SBR, respectively. For CMC/PAA phase inversion was done with acetone and isopropanol for 2 separate casting.
The casted electrodes were then dried in an oven at 70 °C. After half an hour, the casted electrodes

were put in a vacuum oven at 60 °C and 0.1 atmospheric pressure for 16 hours. A secondary drying step was performed (for the aqueous processed electrodes) after cutting the electrode sheets in discs. This was done at 80 °C 10mBarA for 16 hours

The dried negative and positive electrodes were cut in discs (12.7mm diameter) and calendered (only anodes). Calendering was done using a rolling press. The height of the press was set to such a value that it would compress the electrode to obtain, in theory, an electrode porosity of 35%. This height was specific for each electrode disc and was calculated using the density, weight and surface area of the electrode. Thereafter, the half cell batteries were assembled using a coin cell configuration. Build up from the bottom can of the coin was as follows; anode or cathode disc, fiber glass separator to soak up the electrolyte (16mm diameter, Whatman), Celgard 2400 separator (16mm diameter, Celgard), lithium metal (15.6mm diameter, 0.25mm thickness, TOB) together with a stainless steel current collector (16mm diameter, 1.0mm thickness) and then a spring ring along with the top cap. 100 $\mu$L of 1 M $LiPF_6$ in EC:EMC (3:7) (Elyte) + 2 volume% (V%) VC (Elyte) was used as the electrolyte.

| Compound | Binder | NMC811 | Graphite | Carbon black | Solvent |
|---|---|---|---|---|---|
| PAA an | 0.05 | - | 0.9 | 0.05 | 1:22 |
| PES an | 0.05 | - | 0.9 | 0.05 | 1:16 |
| PVDF an | 0.05 | - | 0.9 | 0.05 | 1:14 |
| PAA cat | 0.03 | 0.93 | 0.01 | 0.02 | 1:30 |
| CMC/PAA cat | 0.04 | 0.93 | 0.01 | 0.02 | 1:20 |
| CMC/SBR cat | 0.02 | 0.94 | 0.01 | 0.03 | 1:12 |
| PVDF cat | 0.04 | 0.92 | 0.01[a] | 0.03 | 1:14 |

**Table 3.1:** Relative quantities overview of the different binder based electrodes. For the NMC811 PVDF electrode the graphite type KS4 was used, for the other electrodes this was the graphite type SLS 30.

## 3.2. Cycling regimes

After assembly of the coin cells, electrochemical testing of the different binder based electrode half cells was done using a MACCOR Series 4000. Before each electrochemical measurement, the cells were subjected to a resting period of 24 hours to give the electrolyte sufficient time to wet the electrodes. Then, 3 formation cycles were performed at 0.1C, after each cycle a resting step of 0.5 hours was inserted. These cycles were carried out at a voltage range between 0-2V (long term cycling) or 3V (rate performance cycling) (vs $Li/Li^+$) for the graphite/Li half cells (anode half cell) and between 2.7-4.2V (4.3V for rate performance cycling, vs $Li/Li^+$) for the Li/NMC811 half cells (cathode half cell) and the graphite/NMC811 cells (full cell).

### 3.2.1. Half cell cycling

Rate performance cycle tests were performed on anode and cathode half cells. The anode half cells cycle between 0V-3V and the cathode half cell cycles between 2.7V-4.2V. The half cells were cycled at increasing C-rate, being the charging (de-intercalation for anodes) step for the electrodes. The successive charging C-rates were 0.33C, 1C, 2C, 3C and a final step of 4C. Discharging was done at a rate of 0.33C. Each increasing C-rate cycle is performed three times. In between the 3C and 4C cycles, two recovery cycles at 0.1C were done. After each cycle, a resting period of 0.5 hours was taken.

Long term cycling tests were also performed. For anode half cells this consisted of 100 charge/discharge cycles at C-rate of 0.1C, with a CV step till < 0.05C, from 0V to 2V. For cathode half cells this consisted of 100 cycles by charging at 0.33C, followed by CV charging till <0.05C, and discharging was done at 0.5C in a voltage range of 2.7V and 4.3V. After cycle 52 (2 formation cycles in the beginning shift the total amount of cycles) and cycle 104 , 2 recovery cycles at 0.1C were performed.

After cycling, the electrochemical impedance using electrochemical impedance spectroscopy (EIS) was measured to determine the resistance profile of the half cells. For the cathode half cells, EIS was also

performed prior to the rate performance tests.

### 3.2.2. Full cell cycling

Conducting rate performance and long term cycling tests provided the results to determine which fluorine free electrode would be the most suitable to be tested for the full cell configuration tests. The positive electrode based on the CMC/SBR binder proved to be the most promising. The negative electrode based on the PAA binder was the only thoroughly tested fluorine free electrode formulation and, therefore, chosen as anode. PVDF based anodes and cathodes were used as the positive control electrode.

Full cell configuration was constructed similar to the anode half cell in a coin cell. For this configuration the lithium metal counter electrode was replaced with the CMC/SBR or PVDF formulated electrode as the cathode.

An anode/cathode "combination test" with regard to the binder type was performed as follows: a PAA anode paired with a PVDF cathode, a PVDF anode paired with a CMC/SBR cathode, a PAA anode paired with a CMC/SBR cathode and a PVDF anode paired with a PVDF cathode as the positive control. All the electrodes were cut in discs with a diameter of 12.7 mm. As electrolyte, 100 $\mu$L of 1M LiPF6 in EC:EMC (3:7) + 2 V% VC was used. Before cycling, the cells were put in a climate chamber and subjected to a 24 hour period of electrowetting at 1.5V and a temperature of 40 °C. Then, 3 formation cycles at 0.1C were followed by long term cycling by charging at 0.1C, followed by a CV step till <0.05C, and discharging at 0.33C in a voltage range of 2.7V to 3.8V for 100 cycles. After each cycle, a resting step of 0.5 hours was inserted. Then, with the same protocol, cycling at a voltage window of 2.7-4.2V was done for 50 cycles at room temperature.

Furthermore, 1M LiBOB (Chemetall) was used as the fluorine free electrolyte salt dissolved in EC:DMC (1:1) + 2 V% VC + 1 W% DTD (Sigma Aldrich). Two separate tests were done to test the performance of the LiBOB salt and the additive DTD. The performance of the LiBOB salt was tested using 100$\mu$L 1M LiBOB in EC:DMC (1:1) + 2 V% VC in a coin cell with commercial $LiFePO_4$ or LFP (12.7 mm diameter, Customcells) as the model cathode against a lithium counter electrode (15.6 mm diamter, 0.25 thickness). As reference, the same coin cell was assembled using 100 $\mu$L of 1M LiPF6 in EC:EMC (3:7) + 2 V% VC. The cells were subjected to a simple 0.1C charge/discharge protocol in a voltage range of 2.5V to 3.65V. After each cycle, a resting step of 0.5 hours was inserted. The performance of the additive DTD was tested using 100$\mu$L 1M LiBOB in EC:DMC (1:1) + 2 V% VC + 1 weight% (W%) DTD in a coin cell using a graphite anode formulated with PVDF (12.7 mm diameter) and commercial LFP as the model cathode. As reference, the same coin cell was assembled, but without DTD. Before cycling, the cells were subjected to a 24 hour period of electrowetting at 1.5V. Then, 3 formation cycles at 0.1C were followed by long term cycling by charging at 0.1C and discharging at 0.33C in a voltage range of 2.5V to 3.65V. After each cycle, a resting step of 0.5 hours was inserted.

Ultimately, a completely fluorine free battery cell was constructed using an experimental 3-point electrode flange cell in which the third electrode was a small lithium piece on a copper wire as the reference electrode. A PAA graphite anode (12.7 mm diameter) and a CMC&SBR NMC811 cathode (12.7 mm diameter) where the working electrodes and 100$\mu$L of 1M LiBOB EC:DMC (1:1) + 2 V% VC + 1 W% DTD was used as the electrolyte. The reference electrode remained in the middle of a hole (4 mm diameter) punctured in the graphite electrode. Before cycling, the cells were subjected to a 24 hour period of electrowetting at 1.5V. Then, 3 formation cycles at 0.1C were followed by long term cycling by charging at 0.1C, followed by a CV step till <0.05C, and discharging at 0.33C in a voltage range of 2.7V to 3.8V for 100 cycles. After each cycle, a resting step of 0.5 hours was inserted. Then, with the same protocol, cycling at a voltage window of 2.7-4.2V was done for 50 cycles at room temperature.

## 3.3. Characterisation techniques

### 3.3.1. SEM & EIS

To observe the surface morphology of the (un)cycled electrodes, small pieces of the electrode were cut and stuck on a substrate with carbon tape. Then, the substrate was brought into the SEM machine and the samples were observed under vacuum using the JEOL JSM-IT700HR Scanning Electron Microscope.

To determine the impedance of the (un)cycled cells, EIS measurements were performed using a PARSTAT MC PMC-200 in a frequency range from 10 kHz to 0.01 Hz. Graphite half cells were measured at an applied voltage level of 0.1V and NMC811 half cells and full cells (graphite vs NMC811) were measured at an applied voltage level of 3.7. The cells were measured at their active materials operating voltage to measure the charge transfer resistance more accurately.

# 4

# Results and discussion

In this chapter the results of performed experiments will be discussed. First, an explanation on the electrode processability will be given in chapter 4.1, then, an elaboration on the electrode fabrication process will be given in chapters 4.2 and 4.3.3 for the anode and cathode, respectively. Each chapter on fabrication is followed by a discussion on its respective electrochemical characterisation, for graphite based half cells in chapter 4.3 and for NMC811 based half cells in chapter 4.4. After that, the electrochemical characterisation of full cells will be shown and discussed in chapter 4.5.

## 4.1. Processability of the negative and positive electrodes

In table 4.1 below, an overview on the properties of the different type of electrodes electrodes used in this study is provided. The abbreviations in the table are constituted by the the binder abbreviation followed by its processing method. The processing method consisted of conventional drying (CONV) or phase inversion (PI), as explained in chapter 2.9, by a certain solvent; water (HPI) or aceton (API) or isopropanol (IPI) or ethanol (EPI). For example, PAA_CONVA is the abbreviation for the poly acrylic acid based negative electrode that was conventionally dried. The appended "A" at the end of the abbreviation refers to anode, "C" refers to cathode. Numbers are appended to the abbreviations, like this PAA_CONVA1, to distinguish the different cells.
An explanation on the grading in table 4.1 can be found below:

- Low (L): trait was not sufficient and therefore making the electrode completely unfit for further battery preparation.
- Sufficient (S): trait was good enough for further battery preparation.
- Good (G): trait was very good and made the ease of processing higher.

| Binder | Electrode adhesion | Electrode surface | Casting thickness ($\mu$m) | Electrode flexibility |
|---|---|---|---|---|
| Graphite electrodes | | | | |
| PAA_CONVA | G | smooth | 200 | S |
| PAA_CONVA | S | smooth | 200 | S |
| PES_CONVA | L | smooth | 200 | L |
| PES_HPIA | L | smooth | 200 | L |
| PVDF_CONVA | G | smooth | 200 & 250 | S |
| PVDF_HPIA | G | smooth | 200 | S |
| NMC811 electrodes | | | | |
| PAA_CONVC | G | uneven, rigid | 200 | S |
| PAA_APIC | L | smooth | 250 | L |
| PAA/CMC_CONVC | G | uneven, rigid | 250 | S |
| PAA/CMC_APIC | L | smooth | 250 | L |
| PAA/CMC_IPIC | L | smooth | 250 | L |
| CMC/SBR_CONVC | S | smooth | 150 & 200 | S |
| CMC/SBR_IPIC | S | smooth | 200 | S |
| PVDF_CONVC | G | smooth | 100 | G |
| PVDF_EPIC | G | smooth | 100 | G |

**Table 4.1:** Property grading overview of the different binder based electrodes.

## 4.2. Fabricating graphite electrodes

Below, an elaboration on how the different negative electrodes were fabricated is given along with SEM images of the surfaces for PAA and PVDF based negative electrodes in figure 4.1.
In general, using the roll press for calendering did not give the desired height for the electrodes. Although in theory the height of the roll press was set to the right height to obtain an electrode porosity of 35%, the graphite electrodes possessed enough mechanical stability to bounce back a little bit. Because of this, no graphite electrode produced obtained a porosity of 35%. the Actual porosities can be found in the electrode specification tables in the appendix. For the anode rate performance cycling this can be found in table A.1, for the anode long term cycling in table A.3, for the cathode rate performance cycling in table A.2 and for the cathode long term cycling inA.4.

Electrodes based on the binder PAA needed a solvent-to-binder ratio of 22:1 to obtain an electrode slurry with a low enough viscosity to be well mixed and homogeneously casted. Adherence to the copper current collector was sufficient. However, when cutting the electrode disc, a piece of the casted electrode could separate from the current collector. This would not immediately result in total delamination of the electrode material as the majority of the electrode still adhered. Comparing the two PAA based electrodes by examining the surface of the conventionally and phase inversion treated electrodes shows that the graphite flakes have an equal distribution of the carbon black particles on their surface. Furthermore, the phase inversion treated electrode does have more visible holes on the surface. This could aid the ionic diffusion from the bulk of the electrode to the cathode side.

For electrodes based on the binder PVDF, a solvent-to-binder ratio of 14:1 was used to obtain an electrode slurry with good viscosity to be well mixed and homogeneously casted. Also, the casted electrode slurry showed very good adherence to current collector, maintaining adherence after cutting electrode discs. A big difference in surface coverage by the carbon black can be seen between the two electrode surfaces. A higher surface coverage on the graphite flakes of electron conducting material could aid in the recombination process for the electrons and $Li^+$.

For PES, a solvent-to-binder ratio of 14:1 was used to obtain an electrode slurry with a low enough viscosity to be well mixed and homogeneously casted. This resulted in poor to no adherence to current collector, giving a fragile electrode material which could easily break in shards when trying to cut electrodes. For this reason, apart from a single rate performance test, no further experimentation was done

with PES as a binder material for electrodes in this study.

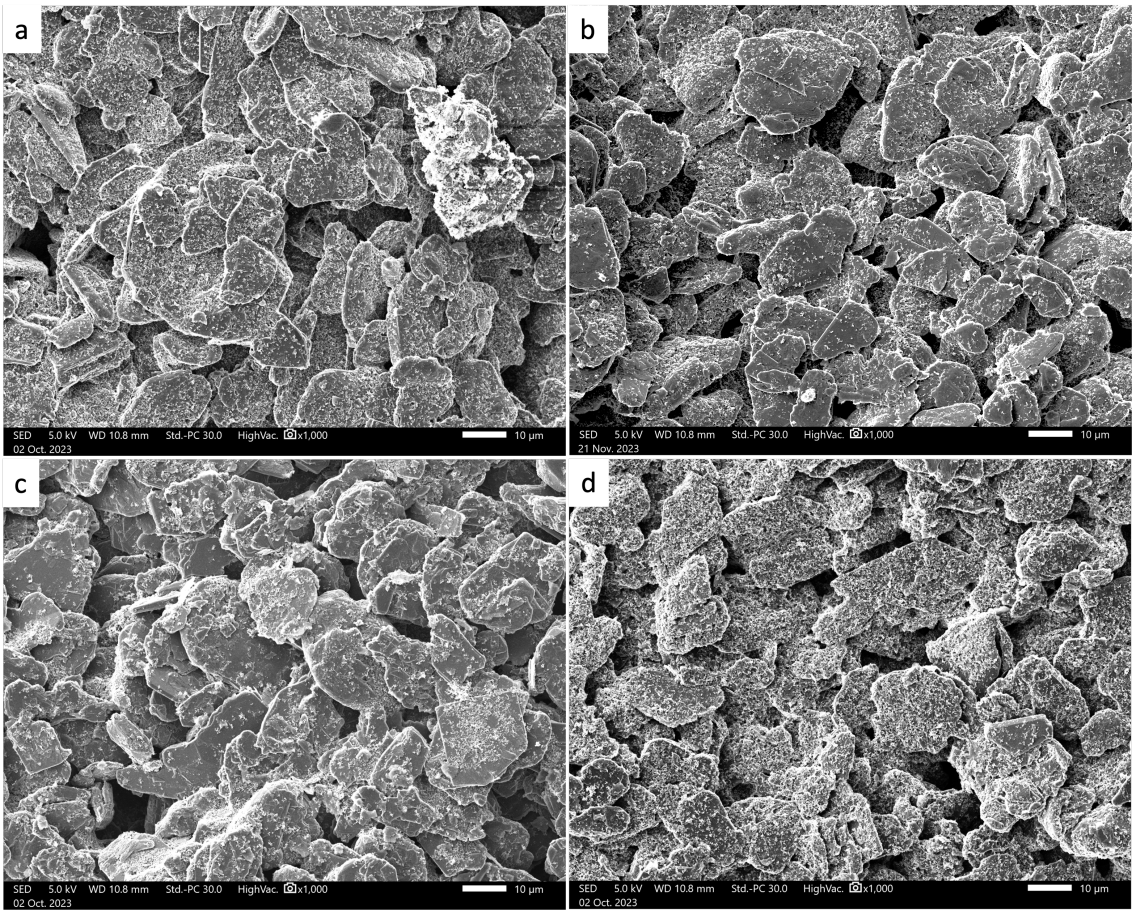


**Figure 4.1:** SEM images of the anode electrode surfaces based on PAA_CONVA (a), PAA_APIA (b), PVDF_CONVA (c), PVDF_HPIA (d).

## 4.3. Electrochemical characterisation of graphite half cells

### 4.3.1. Rate performance cycling of graphite half cells

Rate performance cycling tests were performed to observe the capacity retention for graphite vs. lithium half cells based on different polymeric binders at increasing discharge rate cycles. The discharge rate increased from 0.33C to 4C. Prior to the last cycles at 4c, two recovery steps at 0.1C were done to see to what extend the capacity was retained. Electrode loading can be found in table 4.2; Additional specifications on the thickness and porosity of the electrode are stated in table A.1. The rate performance test was done as explained in chapter 3.2.1 and the results can be seen in figure 4.2.The power plot provided allows for a better comparison between the half cells when having different theoretical capacities. In this plot, for each applied current density, the resulting discharge capacity is a measure for its performance. The higher the delivered capacity at high current densities, the better the cell performs.

| | Capacity ($mAh/cm^2$) |
|---|---|
| PAA_CONVA1 | 4.23 |
| PAA_APIA1 | 4.28 |
| PVDF_CONVA1 | 3.46 |
| PVDF_HPIA1 | 3.93 |
| PES_HPIA | 5.54 |

**Table 4.2:** Loadings of the different binder based anodes used in the rate performance test.

All the cells show a higher discharge capacity for the first 0.33C cycle, after which they stabilise for two cycles. The reason for this is that in the rate performance protocol, the charge-discharge, in that order, cycles are a set for each C-rate. However, charging on the Maccor machine means going to a higher voltage (de-intercalating for graphite) and discharging to a lower voltage (intercalating for graphite). Normally, in a charge-discharge set, the order would be an intercalating step followed by a de-intercalating step. For this protocol it meant that the last discharge of the last formation cycle was actually an intercalation step. Consequently, the next cycle begins with lithiated graphite. The formation cycles were performed at a C-rate of 0.1C, providing for a higher intercalation capacity compared to the other two 0.33C intercalation capacities. The higher intercalation capacity consequently resulted in a higher de-intercalaction capacity compared to the other two 0.33C de-intercalation capacities. Hence, the first discharge capacity of the 0.33C and the 4C cycle is higher. The first recovery cycle has for the same reason a lower discharge capacity compared to the second recovery cycle. In hindsight, the protocol should have had a different formulation.

The PAA based half cells showed a the highest capacity retention at the 0.33C and 1C cycles, with respect to their theoretical capacity, as opposed to the PVDF electrodes. However, for PAA_CONVA1 at the cycles 2C and 3C, the capacity fade is worst. This is also visible by the steeper curves in the power plot. Distinct plateaus can be observed for the set of the cycles at a different rate for the PVDF based cells, this is not the case for the PAA and PES based cells. Moreover, PES_HPIA performed the worst at the higher rates in general. The PES_HPIA electrode a similar thickness as the PAA based electrodes. Therefore, it is suspect that this cell suffered from initial capacity depletion.
Apart apart from cycles at 3C, the half cells based on phase inversion treated electrodes, showed an overall lower capacity retention at all the cycles compared to their conventionally dried counterpart. At the last recovery cycle, capacity recovery with regard to the theoretical capacity is 83% for PAA_CONVA1, 68% for PAA_HPIA1, 78% for PVDF_CONVA1, 60% for PVDF_HPIA1 and 65% for PES_HPIA. In terms of capacity recovery, the phase inversion treated electrodes (PES_HPIA, PAA_HPIA1 and PVDF_HPIA1) perform similar to each other. In comparison to the conventionally treated electrodes, PAA_CONVA1 and PVDF_CONVA1, they performed worse.

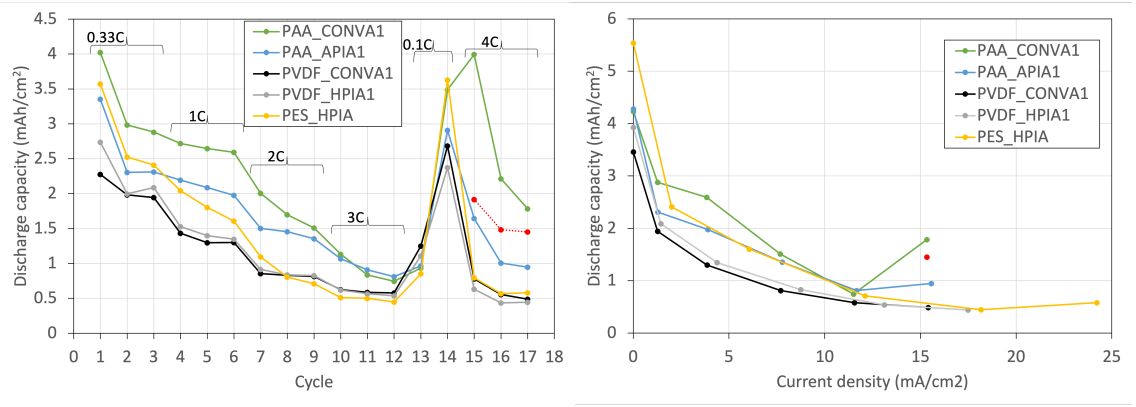


**Figure 4.2:** Rate performance cycles of anode half cell configurations based on the binders PAA, PVDF and PES (a), a corresponding power plot of the third data point of each C-rate step except 0.1C(b).

This lower performance of the phase inversion treated cells can be owed to the higher charge transfer resistance. Provided in figure 4.3a, are the impedance resistance results after the rate performance test. The semi-circles roughly start on the same point of the x-axis. But as a surprise, PAA_APIA1 has a larger semi-circle. Meaning that this electrode has a higher charge transfer resistance compared to the PVDF based electrodes, despite having a lower voltage drop (polarisation voltage) at open circuit potential (OCP) after the de-intercalation step of the cycles. In figure 4.3b the voltage level at OCP can be seen 0.5 hours after the de-intercalation step. Generally, the voltage drop is the highest for the PVDF based electrodes. A large polarisation voltage could entail that a thicker SEI film is formed on the graphite surface and in this way protects the the graphite and the electrolyte. On the other hand, through the formation of thicker SEI layer, the cell has a lower performance at higher applied current densities. This thicker SEI film causes a more complicated internal structure which hampers ionic diffusivity and electron conductivity and increases the polarisation voltage [3]. This assumption is confirmed by the voltage profile of the de-intercalation step. In figure A.2 the voltage curves of the the rate performance test can been seen. The overpotential induced by higher ohmic polarisation voltages (because of the thick SEI) are the main reason for the overall lower discharge capacity for the PVDF based electrodes. Because of this overpotential, the voltage at OCP drops significantly more for PVDF based electrodes after discharging, thereby leaving less ”room” for the charging step [20]. For example, when looking at the 0.1C cycle of PAA_CONVA1 and PVDF_CONVA1. At the lower end, they overlap quite neatly. However, at the other end, the PVDF_CONVA1 curve bails out much earlier and reaches the cut-off potential.

At higher current densities the concentration polarisation voltage plays a bigger part for the difference in discharge capacities between the tested half cells (but also in general, when comparing the discharge capacities at each rate for a single cell). In addition, at higher charging rates, the non-uniformity of the reaction-rate distribution is increased [14]. From this, a higher polarisation voltage caused by concentration differences of $Li^+$ in the active material particles makes the cell potential reach the cut-off early [13]. This in turn prevents the use of the total available active material. Moreover, a larger voltage drop at OCP after discharging could lead to increased electrode degradation or electrolyte decomposition [91]. A binder that provides better dispersion of the active material and reduced ionic diffusion pathways can reduce the polarisation voltage. From this, it can be deduced that the PAA based electrode is the most superior compared to the other binders. Because, it facilitates the electrochemical reaction better due to a better internal electrode structure and therefore performs better at higher current densities.

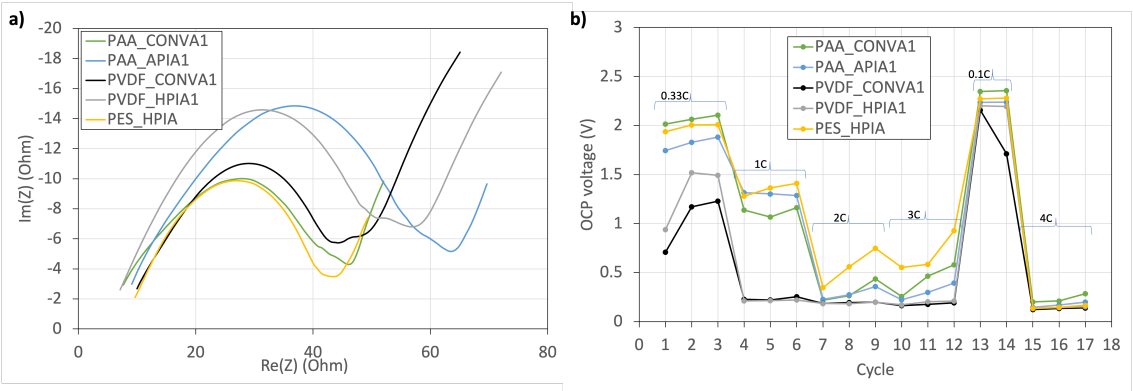


**Figure 4.3:** EIS measurement after rate performance cycling (a). Voltage at OCP at the end of relaxation after the de-intercalation step during the rate performance cycling (b).

The first 4C cycle of PAA conv deviates from the retention behaviour of all the other samples. When observing the voltage curve (figure A.1) of these cycles, it becomes apparent that the additional capacity is registered by the Maccor due to side reactions which are represented by the spiky parts in the graph. The last 4C cycle shows the least amount of side reactions with respect to the two former steps. By manually correcting the discharge capacities obtained by the charge consuming side reaction. An estimate on the real discharge capacity values (shown by the red data points in figure4.2) are about 1.9, 1.5 and 1.5 mAh/cm$^2$. By this, obtaining a capacity retention of 39% at the highest C-rate. PAA_APIA1 did not suffer from side reactions at the 4C cycles and showed at these cycles a capacity retention of 24%. The best performing PVDF cell, PVDF_CONVA1 had a capacity retention of 13% at this C-rate. The side reactions in the PAA_CONVA1 cell may have been the result of the high cut-off potential (3V). A higher cut-off voltage may induce certain side reactions. However, generally, binders in a battery should be electrochemically stable up to 5V vs Li/Li$^+$ [54]. None of the other half cells in this rate performance test showed these side reactions at any certain C-rate.
Furthermore, the PAA and PES based half cells have a higher discharge capacity at the end of the 4C cycles than their last 3C cycle. The PVDF based half cells do not show this kind of capacity retention by ending up at a lower capacity value compared to their last 3C cycle. The reason for this could be the higher mechanical elasticity that the PAA and PES binders posses and therefore contribute to the memory effect of the graphite active material.
**Conclusion:** When taking the results of anode rate performance test in consideration, it can be stated that PAA based electrodes showed enhanced rate performance characteristics compared to PVDF and PES based electrodes at higher charging rates. PAA_CONVA1 exhibited a capacity retention of 39% at a C-rate of 4C. At the recovery cycles (0.1C), PAA_CONVA1 also exhibited the highest capacity retention, being 83%, whilst showed PVDF_CONVA1 the second best capacity retention at 78%. Due to the recovery cycles, the subsequent 4C cycles obtained a higher capacity retention than the 3C cycles for the PAA based cells. The enhanced performance by PAA based cells was achieved by the suspected increased dispersion of the electrode materials and reduced ionic diffusion pathways. PVDF based electrodes suffered more from polarisation voltages and therefore performed worse at higher current densities. For PES_HPIA, initial capacity loss was suspected. Furthermore, in this experiment, the supposed enhanced electrode structure, formed by the phase inversion treatment, did not yet increase the discharge capacity retention at higher discharge rates.

### 4.3.2. Long term cycling of graphite half cells

Long term performance cycling tests were performed to observe the capacity retention for anode half cells based on different polymeric binders over a longer time period. The binders that were tested consisted of PAA and PVDF, and for both conventional and phase inversed electrode species. Each species has two samples, which refers to the appended ”2” (V2) and ”3” (V3) to abbreviated cell name. The appended number 1 was already used for the anode rate performance cells. However, the samples do not always have similar loading. Prior to (only for samples with ”3”) and after cycling, EIS measurements were performed. The theoretical capacities of the cells can be found in table 4.3. Additional information on the thickness and porosity of the electrodes can be found in table A.2.//

| | Capacity (mAh/cm$^2$) |
|---|---|
| PAA_CONVA2 | 4.72 |
| PAA_APIA2 | 3.96 |
| PVDF_CONVA2 | 2.94 |
| PVDF_HPIA2 | 3.66 |
| PAA_CONVA3 | 4.20 |
| PAA_APIA3 | 3.89 |
| PVDF_CONVA3 | 3.07 |
| PVDF_HPIA3 | 3.67 |

**Table 4.3:** Theoretical capacity of the graphite half cells used for long term performance cycling.

In figure 4.4 the discharge capacity per cycle can be seen for the different PAA and PVDF based half cells. All electrode species show an initial capacity that is corresponding with their theoretical capacity along with a very high coulombic efficiency. The first thing that becomes apparent from the long term cycling is that there is a clear correlation between the theoretical capacity and the capacity retention of the electrode over time. The higher the theoretical capacity of the electrode, the worse it performed. PAA_CONVA2 had the highest decrease in capacity retention stability around cycle 30 and PVDF_CONVA3 the lowest decrease around cycle 70 and retained a capacity of 24% after 100 cycles.
The PVDF_HPIA half cells have the sub lowest theoretical capacity. However, capacity retention stability wise, they perform very similarly to the remaining half cells and lose their capacity retention stability around cycle 55. This could indicate that the phase inversion treatment is not beneficial for the PVDF electrode formulation. The remaining PAA and PVDF based half cells have similar performance. In general, the cycling retention behaviour that the half cells show is no surprise as electrodes with a higher loading can suffer more from transport limitations in the electrolyte phase and internal resistance in the solid phase, while having an electrode porosity in the same range. The transport limitations come from the ionic resistance of the electrolyte in the pores of the electrode. The internal resistance causes overpotentials which can induce side reaction during cycling by oxidizing the electrolyte [106].

Interestingly, all V3's outperform their earlier version. Which could mean that another factor has influence on the cycling stability, such as the ambient temperature or the grade of the electrolyte. This could be the case as V3 was cycled a month after V2 and they were cycled in a room in which the temperature can be influenced due to the weather outside. Regarding the electrolyte, there was a presumption that the electrolyte degrades over time due to the influence of light and it could be that the batch used for V2 was an older batch. If you compare V2 and V3 separately, then there is a clear top 4 consisting of PVDF_CONVA in the first place, followed by PAA_APIA, PVDF_HPIA and PAA_CONVA, respectively.
Curiously, every half cell's capacity curve produces a dip at the beginning, after which the capacity steadily increases. This can not be traced back to a malfunction of the Maccor as this does not happen for any half cell at the same cycle. Therefore, it is difficult to explain why this occurs.

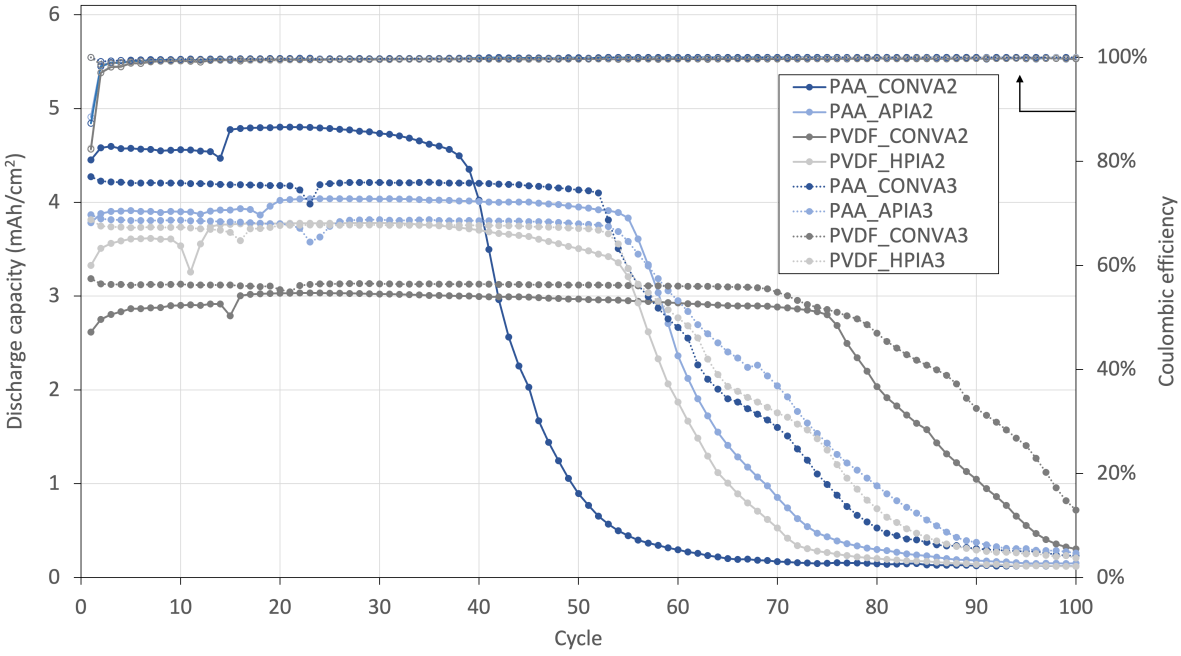


**Figure 4.4:** Discharge capacity per cycle for long term performance cycling for PAA and PVDF based electrodes.

A closer look at the most stable cycling phase of the half cells can give a better understanding on the cycling behaviour. In figure 4.4, cycle 25 appears to be a mutual stable cycling phase for all half cells. The voltage curves of cycle 25 for each half cell can be seen in figure 4.5. The voltage curves behave quite similar, showing very slight differences considering the voltage plateaus. These plateaus represent the intercalation and de-intercalation of lithium into the graphite. Overall, the PVDF based half cell seem to have the least internal resistance, this can be concluded from the fact that the charge and discharge curve lay closer to each other compared to the ones from the PAA based half cells. Moreover, PAA_APIA3 has the lowest intercalation curve. The constant voltage step provides for significant additional charge capacity (+149 mAh/g) after reaching 0.0001 V and a charged capacity of 210 mAh/g. Despite the larger polarisation and consequent OCP voltage shift (straight line upward) at the end of charging, the capacity retention of this half cell is the third to last to degrade.

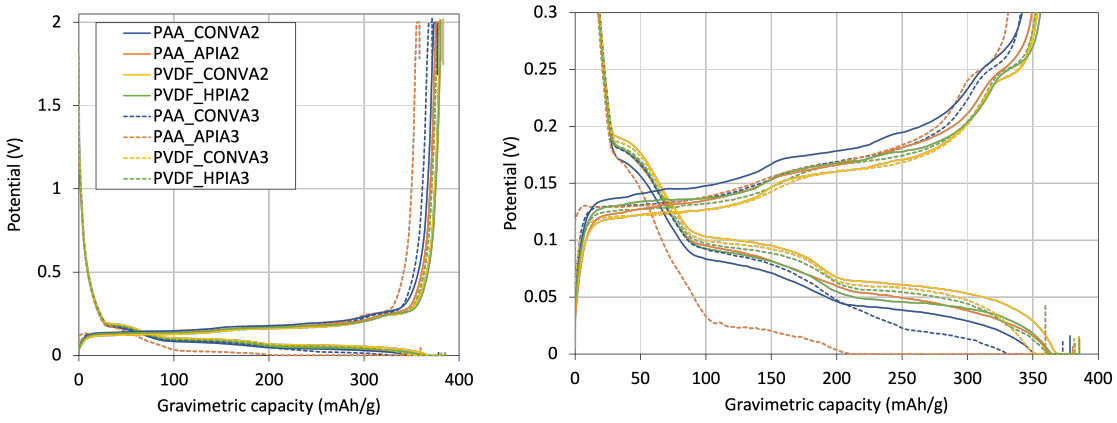


**Figure 4.5:** Voltage curves of the 25th cycle during long term cycling. The graph on the right hand side is focused on the lower potential area of the voltage curves.

A reason for the capacity retention to decrease is the depletion of electrolyte salt and therefore its performance. This is backed up by the fact that the half cells did not stay at the applied potential when CCCV charged to 0.1V for impedance measurements due to electrolyte polarisation [43]. For this

reason, only the high frequency regions of the impedance results are discussed. Additionally, the V2 half cells appeared very dry upon opening them up after cycling . In figure 4.6, before and after EIS measurements are shown. To help the interpretation, the x- and y-axis do not have the same scale.
A difference between V2 and V3 can be seen when considering the high frequency region of the EIS measurements after cycling. The start of the semi-circle at the high frequency region is shifted towards the left for the V3 half cells. Backing up the assumption of a degraded electrolyte batch used for V2. However, no definite conclusions can be drawn from this, because there are no EIS measurements before cycling for V2 half cells.

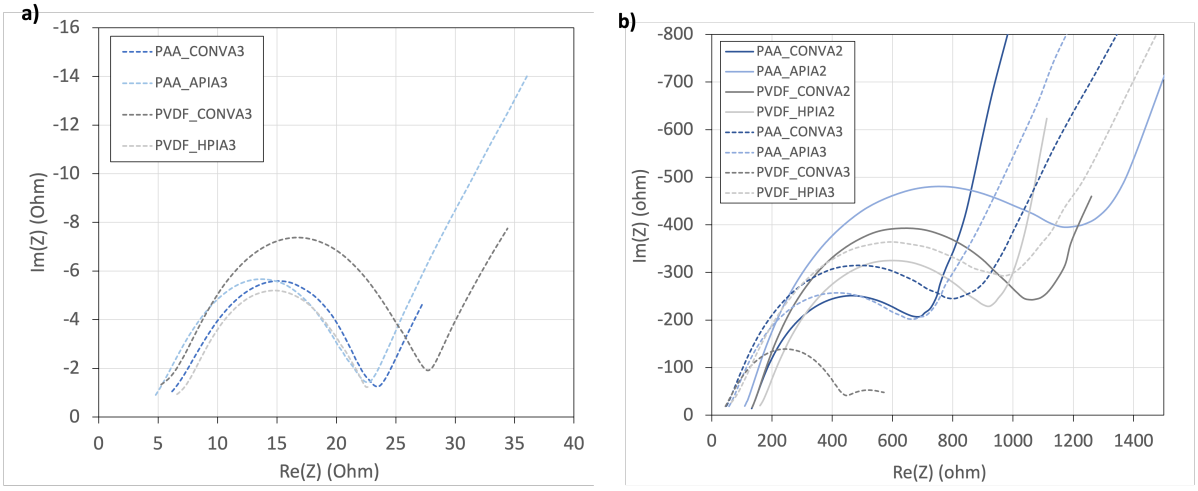


**Figure 4.6:** EIS results for anode half cells before long term cycling (a) and after long term cycling (b).

A difference in surface morphology due to cycling can be seen in figure 4.7. Here, post mortem SEM images are shown, with the white strands being residues of the fiber glass separator. For PAA_CONVA2 and PVDF_HPIA2, the distinct graphite flakes are clearly visible. But for PAA_APIA2 and PVDF_CONVA2, this is not the case. A thicker SEI layer appears to be covering the flakes, which could have protected the electrodes better for decomposition of the electrolyte.

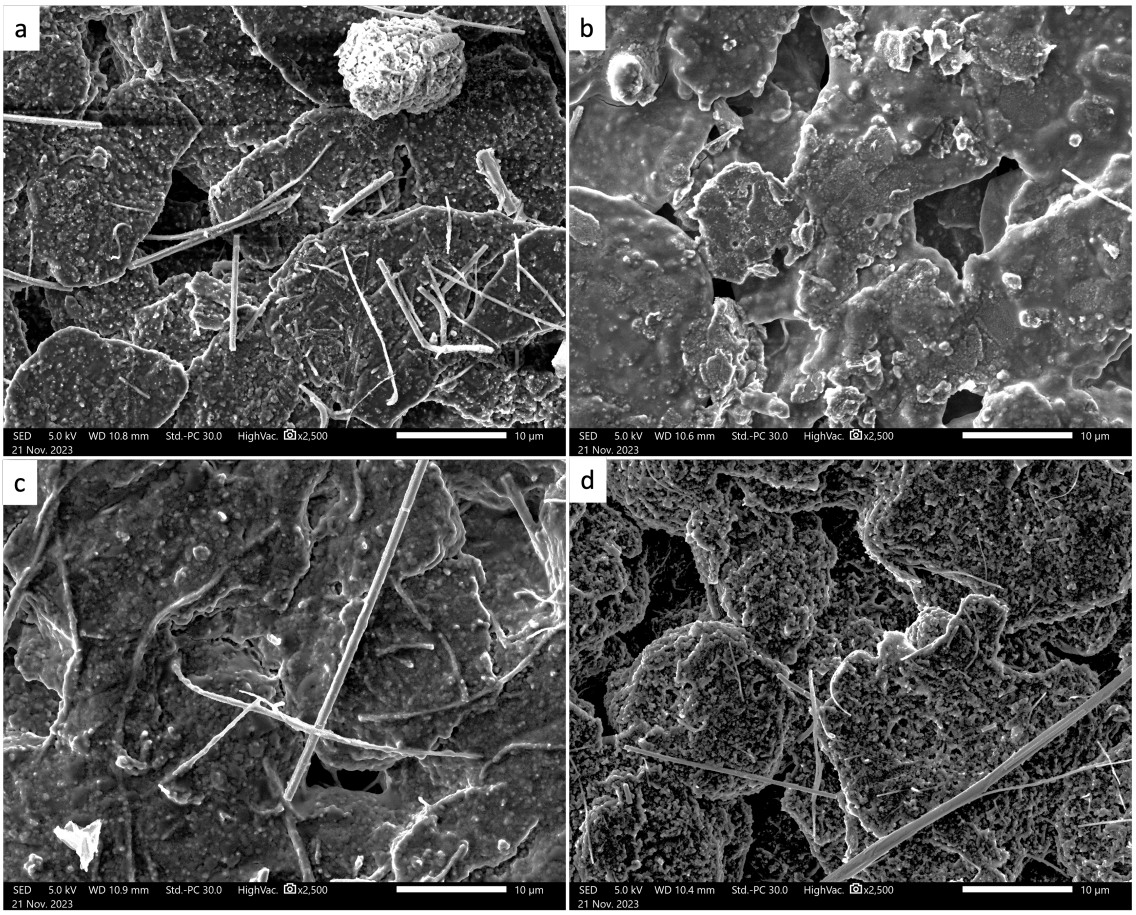


**Figure 4.7:** Post mortem SEM images of the graphite electrodes PAA_CONVA2 (a), PAA_APIA2 (b), PVDF_CONVA2 (c), PVDF_HPIA2 (d).

**Conclusion:** When considering the results of the long term performance cycling and the fact that the grade of the electrolyte played a major role between the two versions (2 and 3), the conventionally dried PVDF based electrodes appeared to have the best capacity retention stability over a longer cycling period. PVDF_CONVA3 performed the best by having a stable capacity retention up to cycle 70 and ending up with a retained capacity of 24% after 100 cycles. Phase inversion treated PVDF electrodes performed less well, indicating that this treatment is not beneficial for the cycling performance. On the other hand, the phase inversion treatment appeared not to have a very large impact on the long term cycling stability for the PAA based electrodes. In general, the loading of the electrodes had a large impact on the capacity retention.

### 4.3.3. Fabricating NMC811 electrodes

For CMC/SBR a solvent-to-binder ratio of 12:1 was used to obtain an oil-like electrode slurry which allowed to be well mixed and homogeneously casted. For this kind of electrode the phase inversion treatment resulted in a more top-to-bottom tunnel structure. This can be seen when comparing the SEM images in figure 4.8a and b for the conventionally and phase inversion treated one, respectively. The imposed electrode structure by the phase inversion treatment could be beneficial for battery performance by aiding ionic diffusion in the electrolyte phase.

Although adherence to the current collector was good, for some area's of the electrode a top layer would separate from the adhered layer beneath. Allowing to see the internal structure of the electrode. The parts of the electrode where this was the case were avoided for making the electrode discs. SEM images of this can be seen in figure 4.8 c for the conventionally dried electrode and d for the phase inversion treated electrode. The red line indicates the edge between the part where there is still a top layer and where there is not. The images reveal a distinct structure for the conventionally dried electrode, which is not present anymore for the phase inversion treated electrode. Furthermore, the edges of the circles

are more electron conducting due to brighter white colour compared to the the middle regions of the circles in figure .

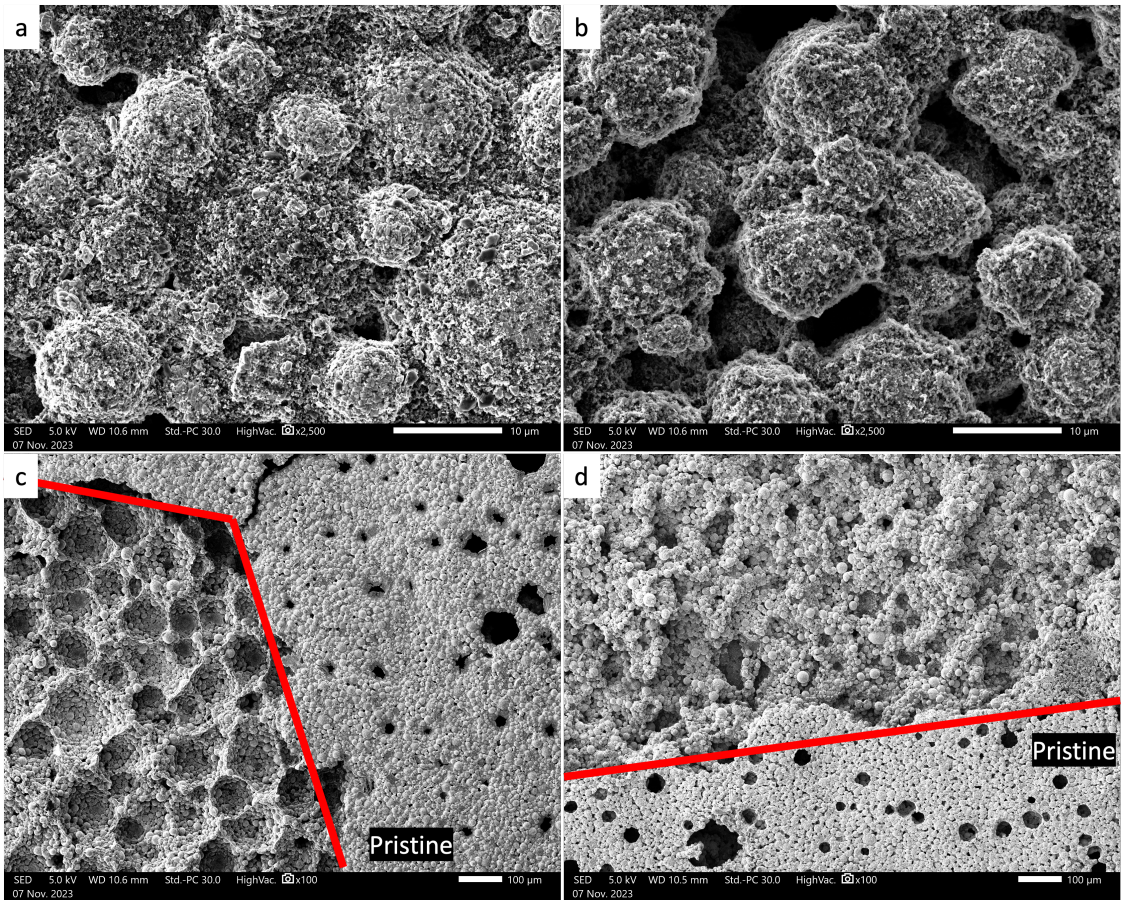


**Figure 4.8:** SEM images of CMC/SBR based NMC811 electrodes processed by conventional drying (a,c) and with phase inversion treatment (b,d). The figures (c) and (d) give a better view of the electrode surface and the red line is the border between the pristine electrode surface and electrode surface without a top layer.

Positive electrodes based on the binder PAA needed a solvent-to-binder ratio of 30:1 to obtain an electrode slurry which allowed to be well mixed and homogeneously casted. SEM images of an conventionally dried PAA positive electrode is provided in figure 4.9. NMC811 can be better distinguished by using the back scattered electron signal to produce an SEM image. The reason for this is that the high atomic number of the metals in NMC811 result in a higher back scattered electron intensity that is picked up by the detector. The higher intensity makes the metals appear white on the image. Compounds with a low atomic number appear darker like grey or black, such as the carbon black and the used binder materials. In figure 4.9b, you can clearly see the NMC811 particles without much coverage of the carbon black or binder material.

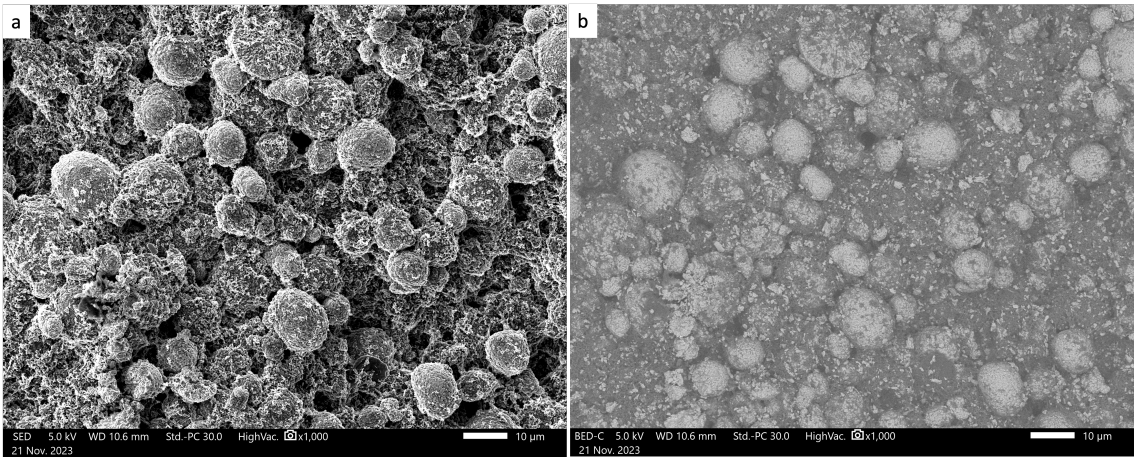


**Figure 4.9:** SEM images of PAA based NMC811 electrode. Made using the secondary electron signal (a) and the back scattered electron signal (b).

For the PAA based electrode, adherence to the current collector was very strong. When fully dried, this resulted in a network-like structure on the back of the current collector as can be seen in figure 4.10b. On the electrode surface, this strong adherence made broken lines along the edges of the network structure, see figure 4.10a. Normally, electrodes surfaces should be flat and smooth. But because of the aggressive deformation of the electrode by the binder, the surface was rigid like a mountain range. This made measuring the thickness of the electrode very difficult. Measuring the thickness of the electrode would by done by laying the electrode on a flat surface and consequently dropping a measuring tip from above. The flat surface would act as the reference height. When placing the electrode on a flat surface, it would not lay flat on the surface, but still have gaps between the electrode and the surface. Dropping the tip on the curved and rigid CMC/PAA electrode would push the electrode to the flat surface beneath (because the flat surface is the reference height), but would also crack the electrode further by trying to make it flat to measure accurately. Therefore, no usable results from measurements on the thickness were obtained.
After applying the phase inversion method, the casted electrode let go of the current collector. This resulted a brittle, free standing, electrode and could easily break upon further handling. For this reason, no further experimentation was performed on the electrode sample treated with the phase inversion method.

For positive electrodes based on the composite binder CMC/PAA, a solvent-to-binder ratio of 20:1 was used to obtain an oil-like electrode slurry which allowed to be well mixed and homogeneously casted. The addition of CMC to the binder mixture helped dispersing the electrode slurry, allowing for a lower solvent content compared to using solely PAA. Adherence to the current collector was also very strong and provided a similar result to electrodes produced with the binder PAA.
An SEM image of CMC/PAA electrode, treated with phase inversion, can be seen in figure 4.11. The back scattered electron image reveals an intricate binder structure imposed by the phase inversion treatment. In figure 4.11c, the carbon black particles (very white and tiny particles) appear well dispersed. An electrode with good dispersion of electron conducting particles and an intricate porous structure could provide for great charge transfer and ion transport kinetics, respectively. However, the

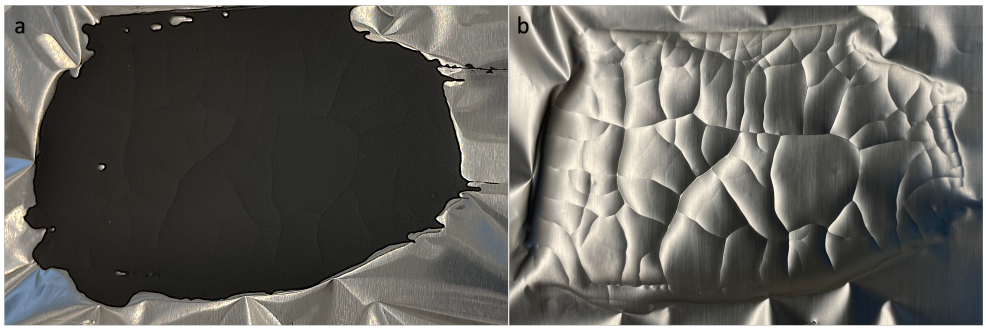


**Figure 4.10:** Front (a) and back (b) of the PAA positive electrode.

phase inversion treatment on the CMC/PAA based electrode resulted in delamination from the current collector. Because of this, a free-standing, and hence a very fragile, electrode was obtained. For this reason, no further experimentation was performed on the samples treated with the phase inversion method.

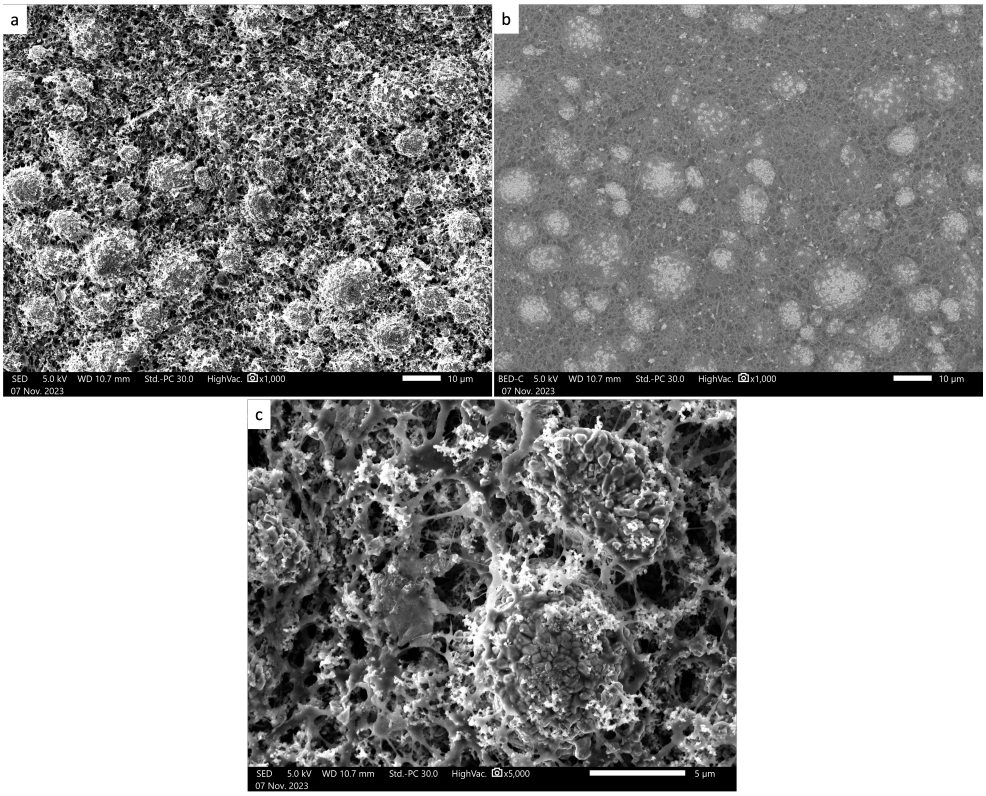


**Figure 4.11:** SEM images of the composite binder CMC/PAA based NMC811 electrode. Two images from the same electrode area using the secondary electron signal (a) and the back scattered electron signal (b). (c) displays a closer look onto the electrode surface.

For positive electrodes made with the binder PVDF, a solvent-to-binder ratio of 14:1 was used to obtain an oil-like electrode slurry which allowed to be well mixed and homogeneously casted. Adherence to the current collector was good, also after applying the phase inversion method. In figure 4.12, SEM images are shown for the two electrode samples. Better coverage of the NMC811 particles is achieved on the electrode surface, similar to the previous phase inversion treated electrode samples. However, the conventionally dried electrode appears to have a more porous structure. The greater coverage of the NMC811 particles seem to act as a barrier for the structure on the electrode surface.

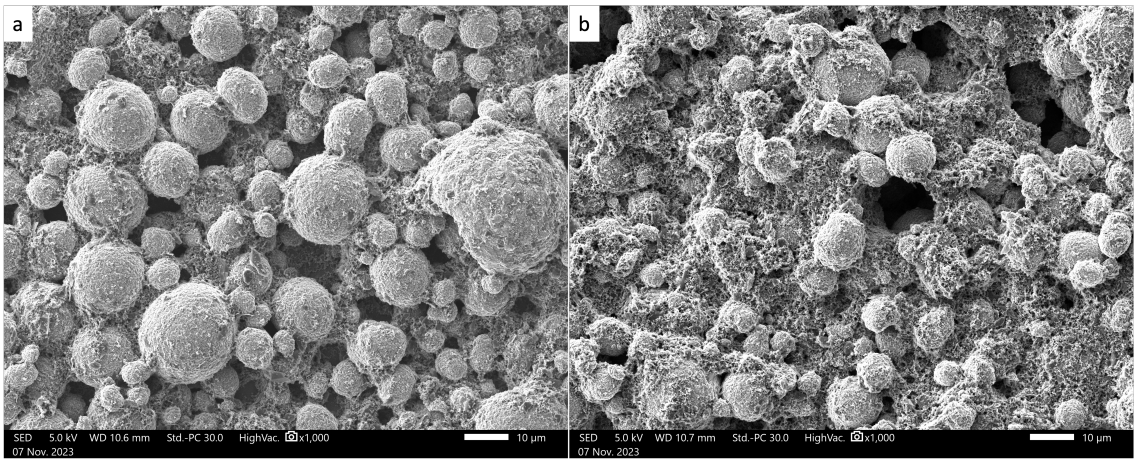


**Figure 4.12:** SEM images of NMC811 electrodes based on the binder PVDF; conventionally treated (a), treated with phase inversion (b).

# 4.4. Electrochemical characterisation of NMC811 half cells

## 4.4.1. Rate performance cycling of NMC811 half cells

Parallel to the anode half cells, rate performance cycling tests were performed on cathode half cells. This was done to observe the capacity retention for positive electrodes at increasing charging rate cycles. Chapter 3.2.1 elaborates on the performed procedure and an overview on the loading, thickness and porosity of the electrodes can be found in table A.3.

In figure 4.13 experimental results of the rate performances tests are shown. Additionally, a power plot is presented. For all the cathode half cells, except the PAA based one, the half cell rate performance tests were done in twofold.

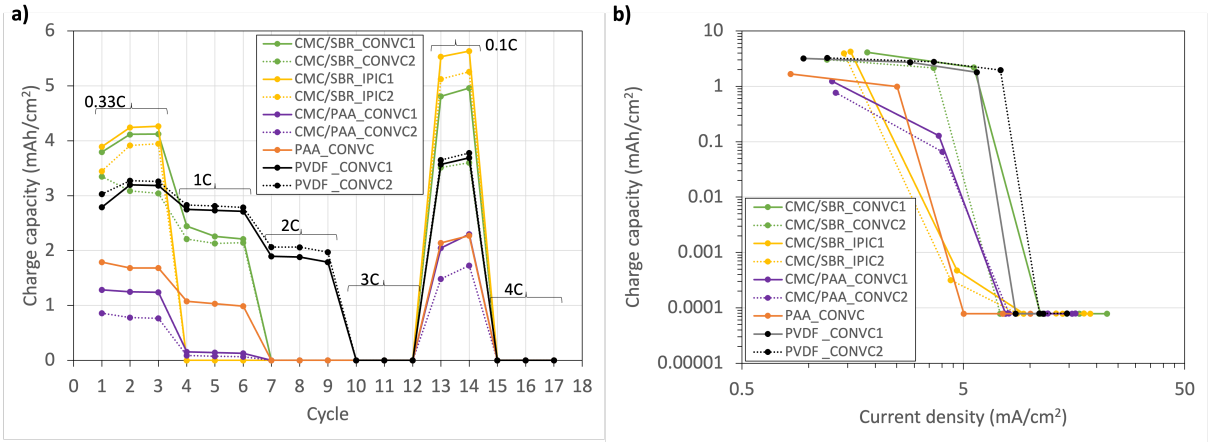


**Figure 4.13:** Charge capacity plotted per rate cycle of the NMC811 half cells. Cell configurations based on the binders CMC/SBR, PAA, CMC/PAA and PVDF (a) and a corresponding power plot of the third data point of each C-rate step except 0.1C(b).

In this rate performance test you can see the distinct C-rate plateaus. This was not the case for the anode rate performance test. Although there is an OCP voltage shift during cycling NMC811 half cells (graph not provided), this drop is not large enough to come close to the nominal voltage of the NMC811 (3.7V). By this, the charge capacities, at different rates are less affected by the discharge cycle that happened before.

In general, the PVDF based NMC811 half cells (V1 3.64 mAh/cm$^2$, V2 3.68 mAh/cm$^2$) performed the best in the rate performance test. This becomes evident from the fact that these were the only two cells capable of showing reasonable capacity in the 2C cycles. Capacity retention at 2C was 49% and 54% for PVDF V1 and V2. CMC/SBR_CONVC1 (5.57 mAh/cm$^2$) had similar loading to the CMC/SBR half cells treated with phase inversion method. But for the CMC/SBR_IPIC (V1 5.91 mAh/cm$^2$, V2 5.54 mAh/cm$^2$) based half cells, the different processing treatment did not turn out to enhance the performance at higher current densities. In any case, it deteriorated the ability to perform better at higher current densities. However, at lower current densities (C-Rate of 0.1C and 0.33C) the half cells did show capacity values much closer to their theoretical capacity. For CMC/SBR_IPIC1 this was 95% at 0.1C (recovery cycle) and 72% at 0.33C and for this was CMC/SBR_IPIC2 95% at 0.1C (recovery cycle) and 72% at 0.33C. Despite the lower charge capacity values during cycling, they slightly outperformed CMC/SBR_CONVC1 (89%) at the recovery cycles. However, this is not the case for CMC/SBR_CONVC2 with a capacity retention of 98%. PVDF_CONVC1 and PVDF_CONVA2 showed a capacity retention of 100%. It could be argued that a lower loading, like it is the case for CMC/SBR_CONVC2 (3.67 mAh/cm$^2$), is of positive influence at larger current densities. Not necessarily meaning that this is also the case at lower current densities when considering the other CMC/SBR based half cells. The fact that the increase of loading decreases the charge capacity at higher rates is confirmed by research of Zheng et al. [106]. According to their study, when the electrode reaches a specific thickness, the characteristic ionic diffusion length of the electrode becomes equal to the electrode thickness at the maximum working C-rate. For their research, the maximum working C-rate is the threshold where the electrode

can obtain 70% of its charge capacity. If the C-rate is increased beyond this point, the characteristic diffusion length becomes smaller than the electrode thickness. As a consequence, the active material on the electrode surface becomes inactive. This leads to a loss in capacity because the electrochemical reaction primarily occurs at the electrode surface, which is no longer electrochemically active at higher rates. The maximum working C-rate is for most binders in this experiment already achieved somewhere between a C-rate of 0.33C and 0.1C. To find this maximum working C-rate properly for each electrode, smaller increments of current density would be needed. For this experiment, the capacity fade is the most severe in a current density range of 5-12 mA/cm$^2$ as can ben seen in figure 4.13b.
The PAA and CMC/PAA based half cells performed poorly. PAA had the lowest loading (2.51 mAh/cm$^2$) of the tested cell, but did not manage to show this charge capacity at the recovery cycles (0.1C). At these rates, it showed only 90% of its rated capacity. Also, the CMC/PAA based half cells had similar theoretical capacity to that of the PVDF based cells, but performed the worst of all the cells. A better understanding about the internal resistances could give insights for the low performance of the CMC/PAA based cells.

Below, results of EIS measurements before (a) and after (b) the rate performance test can be seen in figure 4.14. EIS measurements were performed at a potential of 3.7V. However, not all measurements were carried out in the same frequency range, this is indicated by the frequency indication at the end of the impedance curves. Some impedance curves show double semi-circles after another. The first one, at high frequency, is related to the migration of $Li^+$ through the SEI layer. The second one, at lower frequency, is related to the charge transfer reaction and the double layer capacitance [52]. The resistance value at the end of the semi-circle for PAA_CONVC is lower compared that of the CMC/SBR_CONVC2, despite performing worse in terms of capacity.

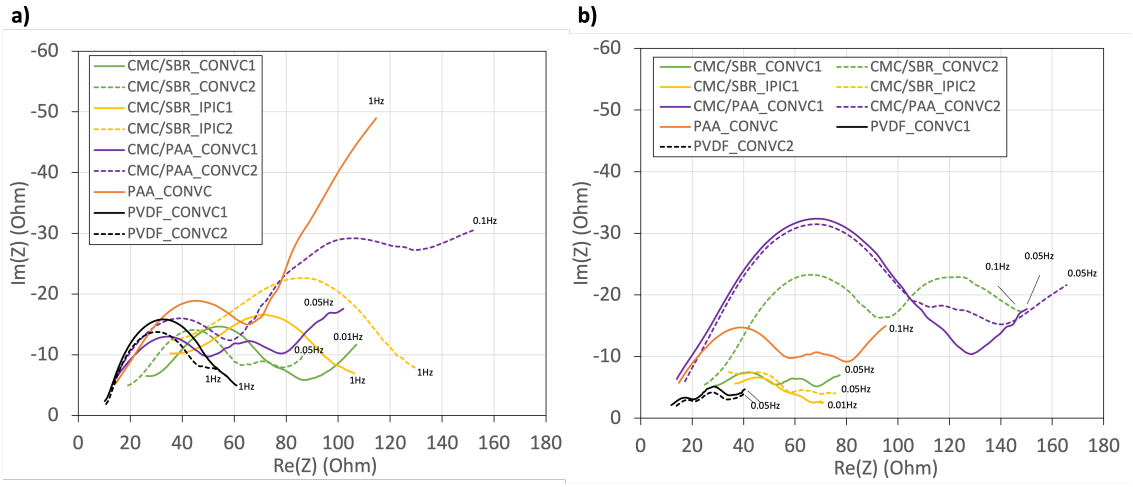


**Figure 4.14:** EIS results before rate performance test (a) and after rate performance test (b).

Moreover, during cycling a higher polarisation for PAA_CONVC makes the cell voltage reach the cut-off early (see figure 4.15). A reason for the early cut-off could be the surface morphology of the PAA_CONVC electrode, which was not flat due to the strong adherence of PAA binder to the surface of the aluminium current collector. A non-flat surface would also mean that the internal structure of the electrode is non-uniform. The non-uniformity may have decreased the available active material due to contact loss between the active material particles. Accordingly, the even poorer performance of the half cells based on CMC/PAA could be explained by high charge transfer resistance values. In the end, adding the CMC polymer to the binder mixture increased the dispersion of the electrode mixture, but did not contribute to the performance of the cell.

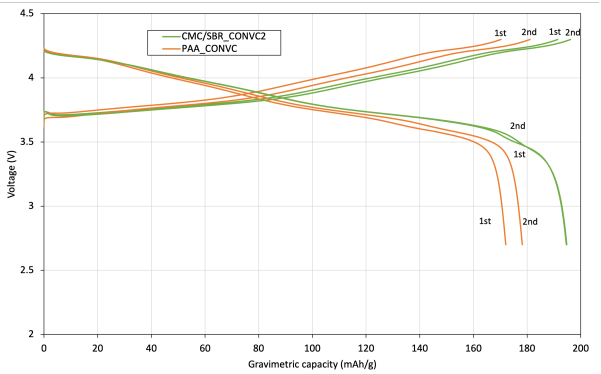


**Figure 4.15:** Voltage curves of the recovery cycles of PAA_CONVC and CMC/SBR_CONVC2. First and second recovery cycle marked with "1st" and "2nd".

The high performance of PVDF based half cells is the result of a lower resistance at the end point of the semi-circles as can be seen by the EIS measurements before cycling. Moreover, in the same graph it can be pointed out that a higher loading affected the resistance at high frequencies for CMC/SBR_CONVC1 and _IPIC1 and _IPIC2 compared to CMC/SBR_CONVC2. A higher loading increases the ionic diffusion distances which results in a higher ionic resistance in the electrolyte within the electrode pores [106]. In addition, the CMC/SBR_IPIC electrodes have a higher ionic resistance in the solid phase, which is the main driver for the capacity decrease at higher rates. This ionic resistance can be attributed to the imposed morphology through phase inversion.
EIS measurements after rate performance testing for CMC/SBR_CONC1, CMC/SBR_IPIC1 and CMC/SBR_IPIC2 and PVDF_CONVC1 and PVDF_CONVC2 were performed a long time after the experiments were done. This resulted in impedance results which are dominated by charge transfer kinetics as at high frequencies the tail does not show. In addition, the resistance and capacitance are very low, lower than before cycling, which is odd. A as consequence, these measurements are not representative and are therefore not taken into account.

**Conclusion:** With the results in mind, PVDF based positive electrodes performed the best in the rate performance cycling tests. These cells retained a capacity of around 52% at a C-rate of 2C, but the other cells showed 0%. At higher C-rates no capacity was shown by any cell. CMC/SBR based electrodes showed predominantly at the lower C-rate rates high capacities. Showing still 95% of the theoretical capacity at a C-rate of 0.33C. At higher rates, the capacity fade was severe. This was especially the case for the phase inversion treated CMC/SBR electrodes, which suffered from high loading and an electrode structure that did not contribute to the ionic diffusion in the solid phase. PAA and CMC/PAA based electrodes suffered from the fact that the electrode structure was non-uniform due to the high binding strength of PAA to the current collector. For this reason, these electrodes showed lower charge capacities at every rate.

### 4.4.2. Long term cycling of NMC811 half cells

Long term cycling tests were performed on CMC/SBR and PVDF based NMC811 half cells. Table A.4 provides more specifications on the properties of the electrodes used in this experiment. The results of this long run experiment can be found in figure 4.16. There, you can see the gravimetric discharge capacities per cycle with the corresponding coulombic efficiencies. Also, there were 2 formation cycles in the beginning and 2 sets of recovery cycles, halfway and in the end of the experimental procedure.

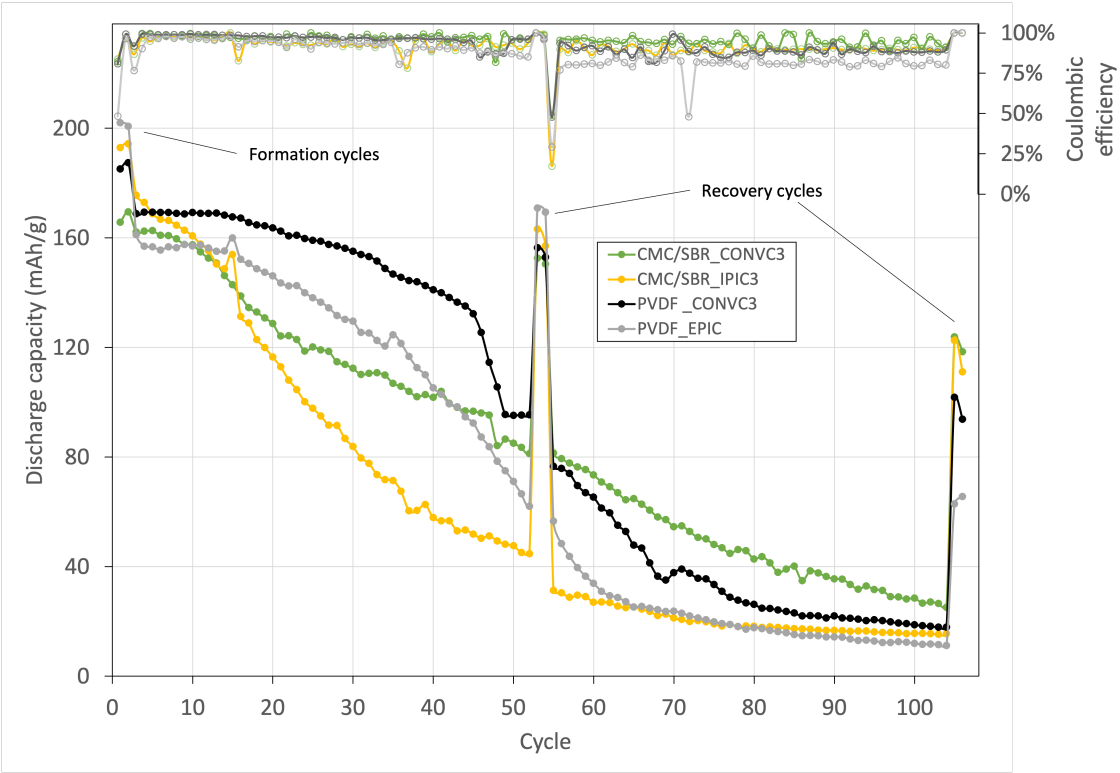


**Figure 4.16:** Gravimetric discharge capacity per cycle for CMC/SBR and PVDF based positive electrodes (conventional and phase inversion treated). Including coulombic efficiency per cycle.

The recovery cycles indicate that still a significant amount of capacity can be retrieved upon cycling the half cells at a C-rate of 0.1C. In table 4.4 and overview of the capacity retention is provided. The PVDF_CONVC3 cell is the most stable and shows the highest discharge capacity in the early phases of cycling, but towards the end its curve drops below the capacity curve of CMC/SBR_CONVC3. At the same time, for PVDF_CONVC3 the coulombic efficiency drops slightly and resonates around 89%, while the coulombic efficiency of CMC/SBR_CONVC3 resonates around 95%. The fact that CMC/SBR_CONVC3 is outperforming PVDF_CONVC3 in the long run could be considered impressive as CMC/SBR_CONVC3 is thicker and much larger the porosity (52%), with PVDF_CONVC3 porosity value close 30%. High values belonging to thickness and porosity can impede ion transfer because of the longer diffusional path in the electrolyte within the electrode and thus hampering the performance of the cell [106]. Although PVDF_EPIC and CMC/SBR_IPIC3 show the highest decrease in capacity retention during cycling, they still recover a great amount of capacity during the recovery cycles. Indicating that the capacity fade is not due to contact loss of the active material particles.

High overpotentials in the later cycles prevent capacity increase by the regular charging, almost all the charge comes from the CV charging step. The point where this occurs is where the charging curve goes above the discharging curve in figure A.3. In that graph, the charge capacity from the CV step is plotted against the discharge capacity of the cells. The crossing of the charge and discharge curve is happening earliest for the samples PVDF_EPIC and CMC/SBR_IPIC3. The CMC/SBR_CONVC3 cell provides the longest in terms of CC charging out of all cells. If you look closely at the first charge capacity of the recovery cycles of the CMC/SBR based half cells, the capacity is lower than the previous cycle. This is because the recovery cycle does not have a CV step which would otherwise provide for additional capacity in the charging step. The lower charging capacity is a result of the high polarisation. A thicker electrode, accompanied with higher porosity are the main reason for this [106]. The higher discharge capacity at the recovery cycles probably comes from the remaining capacity in the cells that was not discharged due to the polarisation during cycling. The polarisation for the PVDF based half cells is less high and therefore no dip in the charge capacity is visible.

Phase inversion treated electrodes show worse results when comparing them to their conventionally treated counterparts. When comparing PVDF_EPIC and PVDF_CONVC3, it shows a more rapid decline in capacity for PVDF_EPIC. After cycle 36, the decline is the steepest for PVDF_EPIC between all cells. Notably, at the first two recovery cycles, this half cell shows a higher discharge capacity than the other half cells. However, a the last 2 recovery cycles, the capacity recovery is the least of all cells for PVDF_EPIC. Moreover, the biggest difference in discharge capacity between CMC/SBR_IPIC3 and CMC/SBR_CONVC3 happens from cycle 15. This is where the discharge capacity fades very quickly for CMC/SBR_IPIC3. On the other hand, CMC/SBR_IPIC3 does show similar discharge capacities to that of best performing half cell during the recovery cycles, being CMC/SBR_CONVC3. Similar to the rate performance cycle test of the NMC811 half cells (chapter 4.4.1), in this experiment, the imposed electrode structure (via phase inversion) of CMC/SBR_IPIC3 did not contribute to the performance of the cell due to increased internal resistance in the solid phase (assuming the tail appears at a lower frequency and therefore at a higher resistance). Moreover, as discussed in chapter 4.3.3, the greater coverage of conducting particles for PVDF_EPIC by the phase inversion method did not turn out to provide for enhanced charge transfer kinetics. This is also confirmed by the EIS measurement and this will be discussed below.

| Capacity retention | vs. rated capacity | | vs. last formation cycle | |
|---|---|---|---|---|
| After cycle | 54 | 106 | 54 | 106 |
| CMC/SBR_CONVC3 | 76% | 60% | 89% | 70% |
| CMC/SBR_IPIC3 | 79% | 56% | 81% | 57% |
| PVDF_CONVC3 | 77% | 47% | 82% | 50% |
| PVDF_EPIC | 85% | 33% | 84% | 33% |

**Table 4.4:** Capacity retention after 54 and 106 cycles when comparing the last cycle of the recovery cycles with the rated capacity and the last formation cycle.

EIS measurements were performed at the end of the long term cycling experiment. For these measurements, all the half cells were brought to a voltage level of 3.7V. However, not every cell was measured up to the same frequency value as can be seen in figure 4.17. For this reason, only a tail appears for CMC/SBR_CONVC3. Two semi-circles can be observed in the graph, but for CMC/SBR_CONVC3 and CMC/SBR_IPIC3 the beginning of the semi-circle at the high frequency is not visible. Processes responsible for this impedance behaviour could be the dominating migration of the $Li^+$ to the surface layer from the electrolyte phase in this frequency range. The charge transfer resistance for PVDF_CONVC3 is lower compared to CMC/SBR_CONVC3, meaning that other resistive processes are dominating, leading to the lower capacity retention. Regional degradation of the electrode structure might be a reason for this, leading to a lower overall capacity retention and at the same other regions that are still intact might contribute to a lower overall resistance.

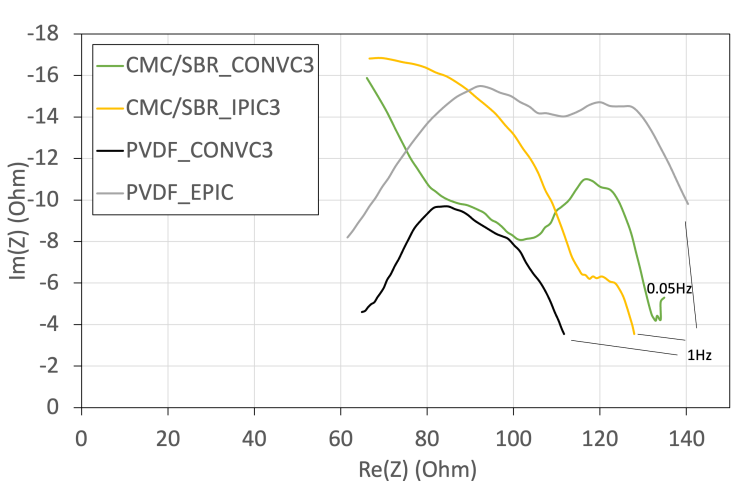


**Figure 4.17:** Nyquist plot of the EIS results after long term cycling for NMC811 half cells.

**Conclusion:** By taking the results of the long term cycling in consideration, CMC/SBR_CONVC3 showed the highest capacity retention during cycling. This cell obtained a capacity retention of 60% at the last recovery cycle (cycle 106). In addition, the results indicate that the CMC/SBR based electrodes can provide better properties in the long run performance and the consequent recovery steps, despite suffering from a higher polarisation voltage compared to PVDF based cells. Thickness and porosity were suspected to be the main driver behind this polarisation. In general, conventionally treated electrodes showed the highest capacity retention and phase inversion treated electrodes showed the lowest capacity retention.

## 4.5. Full cell electrochemical characterisation

Electrochemical characterisation was done for full cells (graphite vs NMC811). Multiple full cells were tested in a "binder combination test". In the binder combination test, positive and negative electrodes based on different binders were tested together in a coin cell. In these cells, $LiPF_6$ was used as the electrolyte salt. In addition, a complete fluorine-free cell was tested in 3-point electrode flange cell. The fluorine-free flange cell consisted of a PAA anode and a CMC/SBR cathode, both electrodes conventionally dried and LiBOB was used as the electrolyte salt. For all full cells the anode/cathode capacity ratio was around 1.2. The higher anode capacity prevents Li-plating on the anode side [78]. Furthermore, after cycling the full cells did not stay a the applied voltage level of 3.7V for impedance measurements, but dropped immediately to 3.0V or lower after CCCV charging. The impedance is very responsive to the state of charge of a battery cell, because it determines the transfer resistance in the cell [80]. Therefore, the impedance results were not taken into consideration as they do not accurately reflect the impedance at a voltage level of 3.7V.

Only conventionally dried electrodes were used in the combination tests. For the anode, PAA and PVDF based electrodes were used. For the cathode, CMC/SBR and PVDF based electrodes were used. The electrodes combinations that were tested are as follows: PAA based anode with a PVDF based cathode (A:PAA_C:PVDF), PVDF based anode with a CMC/SBR based cathode (A:PVDF_C:CMCSBR), PAA based anode with a CMC/SBR based cathode (A:PAA_C:CMCSBR) and a cells consisting of only PVDF as a binder (A:PVDF_C:PVDF). The latter combination acting as the positive control cell. The results of the combination tests are shown in figure 4.18. The discharge capacities are averaged from the results of two cells for each species of full cell. Theoretical capacities of the anodes and cathodes as well as the thickness and porosity can be found in table A.5.

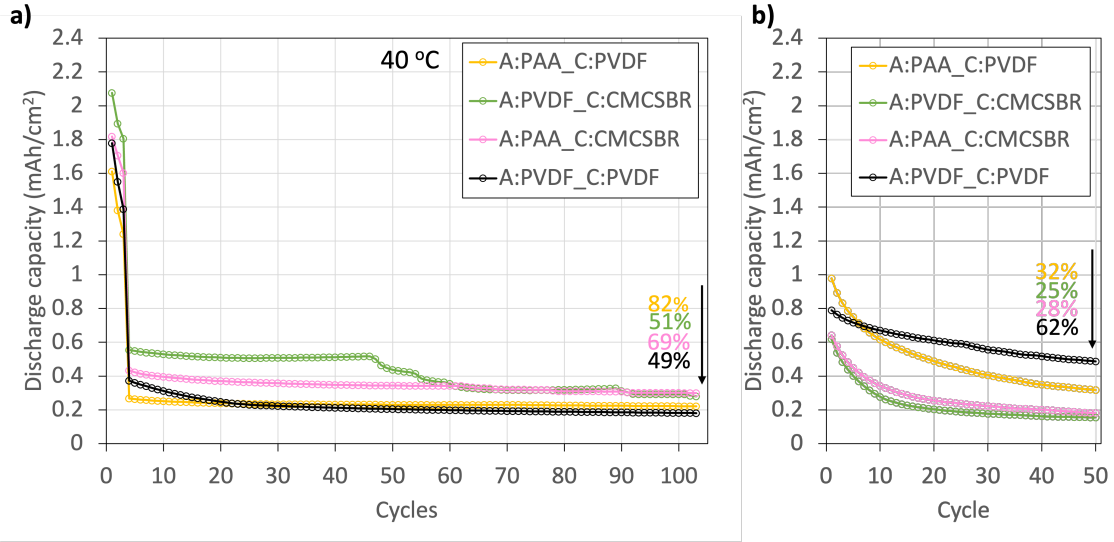


**Figure 4.18:** Discharge capacity per cycle for full cell using different binders. 3 formation cycles (2.7-4.2V) followed by cycling between 2.7-3.8V (a) and the subsequent cycling between 2.7-4.2V to observe capacity in larger window (b). The he capacity retention for each full cell is shown for each operating voltage window.

In figure 4.18a, the discharge capacities are shown during 100 cycles (discharge at 0.33C) with a cut-off voltage at 3.8V after three formation cycles (2.7-4.2V) at a temperature 40 °C. During the formation cycles, a decrease in discharge capacity associated with the SEI formation can be seen. However, the discharge capacities are already at around 60% of their theoretical capacity. 40% of $Li^+$ loss is a severe depletion of the available capacity. Generally, 10% is irreversibly consumed by formation of the SEI [55]. Moreover, there is a significant capacity drop after the formation cycles, because the cells operate at a smaller voltage range (2.7-3.8V). The smaller voltage range puts less stress on the cell and increases cycle life, but prevents a significant capacity gain at the higher voltage region (3.8-4.2V). Usually, the capacity decrease is around 37.5% when considering that NMC811 can deliver a capacity of 200 mAh/g (up to 4.2V) [57].
The formation cycles show a decreasing trend in terms of capacity and are already much lower than the theoretical average capacity of the cells (table 4.5). The consequent capacity drop when transitioning to the smaller voltage window is around 78%, ,70%, 73% and 73% for A:PAA_C:PVDF, A:PVDF_C:CMCSBR, A:PAA_C:CMCSBR and A:PVDF_C:PVDF, respectively. The severe capacity drop may be attributed to the available intercalation sites in the graphite. A decrease in intercalation sites may be caused by transport limitations inside the negative electrode structure. After the initial capacity fade, the capacity retention slowly stabilises. After 100 cycles in a voltage window of 2.7-3.8V, the capacity retention is the lowest for A:PVDF_C:PVDF (49%) and the highest for A:PAA_C:PVDF (82%). However, A:PAA_C:PVD suffered from a higher capacity depletion in the smaller operating window, thereby giving a wrong impression on the performance. Compared to the theoretical capacity, A:PAA_C:CMCSBR showed the highest capacity retention in the smaller operating window, being only 9%. Up till now, this kind of initial capacity depletion has not been observed for the graphite or NMC811 half cells during the rate performance cycles and long term cycles. However, this is mainly because of the large lithium inventory of the counter electrode in these half cells.

For each full cell combination, one of the cells showed a higher initial discharge capacity. On the basis of this, the voltage curves of the formation cycles are compared. The voltage is plotted against the gravimetric capacity of these cells in figure 4.20. The first charge, which is the de-lithiation of the cathode, is higher than 200 mAh/g for every cell. Theoretically this is not possible and would suggest that another reaction takes places during this charge. Around 2.8V a dip can be seen in the curves, suggesting another redox reaction. The electrons have to come from the cathode, otherwise this would not increase the first charge capacity by up to a 25% of the theoretical capacity. The reaction that takes place could have to do with the reduction and or oxidation of VC or EC. However, VC is more easily reduced at the anode side and more easily oxidised at the cathode side compared to EC. Would that mean that VC provides electrons for its own reduction at the anode trough oxidation? No, because VC is reduced at the anode at a reduction potential of around 2.5V in a full cell (this corresponds to 1.2 vs $Li/Li^+$ for the graphite negative electrode potential) and is oxidised above 4.3V vs $Li/Li^+$. VC driving its own reduction could therefore not be possible. [22, 70]. The reduction potential of VC at 2.5V vs $Li/Li^+$ could mean that the reduction of VC consumed the surplus of electrons in the first charge. However, is it difficult to determine which oxidation reaction takes place a the cathode. A study by Xia et al. determined the impact of additives to 1M $LiPF_6$ in EC/EMC (3:7) on graphite/NMC pouch cells [92].
In figure 4.19, the the differential capacities against the voltage of several cell are shown. In a) the best performing A:PVDF_C:PVDF cell (with 2%V VC) and best performing fluorine free full cell (with 2%V VC and 1%W DTD) and in (b) the pouch cells with various electrolyte additives of Xia et al. [92]. A more elaborate discussion on the results of the fluorine free cells can be found in chapter 4.5.1. The pouch cells had a capacity of 225 mAh and 728 $\mu$L of electrolyte was used, which is respectively 53 and 7.3 times the quantities used in this thesis. Moreover, in relation to the amount of capacity, they would have used 13.5 $\mu$L of electrolyte for the full cells in this thesis. In their 2% VC cell, they show that VC reacted at a potential of 2.6, having its peak at 14 mAh/V. Also, they reported that the fraction of irreversible capacity for the 2% VC cell was almost 0.1. For the A:PVDF_C:PVDF cell VC presumably reacted at a voltage of 2.8V, having its peak at 1.35 mAh/V. The fraction of irreversible capacity for VC in A:PVDF_C:PVDF is around 0.24. The 3PF-free_2 cell, which contains 2 V% VC and 1 W% DTD, has a similar voltage peak intensity decrease for DTD. This confirms that the peak observed at 2.8V is assigned to VC. The reason for this peak shift and intensity decrease is not clear [92].
In comparison Xia et al. had 7.4 times a lower amount of electrolyte (with regard to the amount of

cell capacity). When putting their research as the benchmark for the amount of electrolyte and the fact that the fraction of irreversible capacity for VC in A:PVDF_C:PVDF is only 0.24 and not higher, would suggest that another reason is the cause for this significant capacity increase in the first charge.

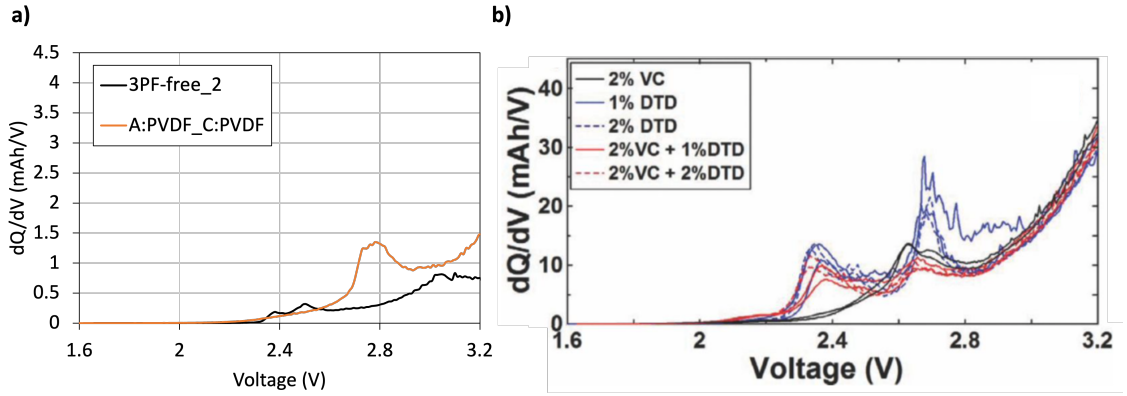


**Figure 4.19:** Differential capacity (dQ/dV) against the voltage during the formation cycle of 3PF-free_2 and A:PVDF_C:PVDF (a) and during the first charge of the graphite/NMC pouch cells with different electrolyte additives used in the study of Xia et al. (edited) [92].

Hydrogen evolution due to the residual moisture removal in the electrodes is another suspect for the charge consumption in the first cycle. Galushkin et al. states that it is generally accepted that hydrogen evolution in the first cycle of charge (up to 4.0V) is connected with the residual moisture removal from the electrolyte. This generated an $H_2$ concentration of 20.1 ppm, which is reasonable for battery grade battery grade carbonate electrolytes [58]. During longer cycling, the hydrogen evolution appeared to be potential independent as the hydrogen concentration grew independently on the cell voltage [27]. It was proven experimentally that this further hydrogen evolution was connected to electrolyte decomposition. However, the cells in this thesis were cycled up to 4.3V and electrolyte decomposition should not happen up to a voltage of 4.57V [27]. Metzger et al. proved their hypothesis that the diffusion of protic electrolyte oxidation ($R\text{-}H^+$) from the cathode to the anode and their subsequent reduction is the origin of increased $H_2$ formation when charging up to 4.2V (along with an increased first charge capacity). $H_2$ formation is further increased at higher charging potentials; where more electrolyte oxidation takes place, and at higher temperatures; where the SEI is unstable [58]. However, with the addition of electrolyte additives (2 W% VC or 1 W% DTD) the formation of $H_2$ was significantly reduced in a full cell configuration while charging up to 4.6V. Proving the effect of the reduction of VC to form a stable SEI.

Burns et al. showed that through "rollover failure" the oxidation of the electrolyte in graphite//NMC cells led to decreased coulombic efficiency during cycling, increased impedance, higher self-discharge rates during storage and consequently capacity loss [11]. In addition, Burns et al. proposed a plausible model for the rollover model. In this model, the diffusion of electrolyte oxidation products created at the NMC electrode to the anode reduce and form a layer of unwanted material. By this, leading to an increase in kinetic resistant for $Li^+$ intercalation and deintercalation [11].

The reported results by other authors show something similar to the results in this study. However, the question remains why in our case the electrolyte would be able to oxidise at the cathode side and why there was not a stable SEI formed on the anode to inhibit subsequent $H_2$ formation.

The increased charge capacity in the first formation cycle is also observed for the NMC811 half cells, this is highlighted for PVDF_CONVC3 and CMC/SBR_CONVC3 in figure A.4. The extra charge capacity is barely observed for CMC/SBR_CONVC3 and this could point to initial capacity depletion. The highest extra charge capacity is seen for the full cells which have a PVDF based NMC811 electrode (4.20a and d). For these cells, the discharge capacity depletion in consequent cycles is much more severe in comparison to the full cells which have a CMC/SBR based NMC811 electrode. Another correlation can be seen between the full cells with a PAA and PVDF based graphite electrode. The full cells which have a PAA based graphite electrode seem to have the highest capacity fade during the discharge. Regarding the initial capacity retention, this results in the worst combination being A:PAA_C:PVDF and the best combination A:PVDF_C:CMCSBR.

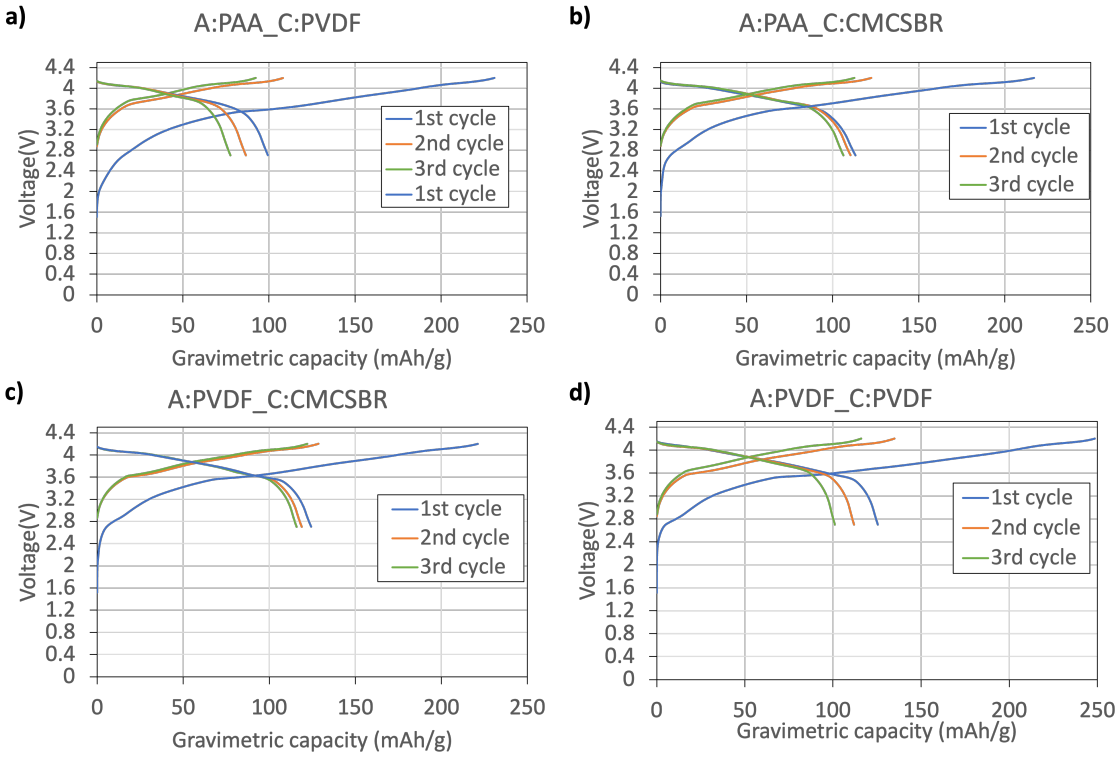


**Figure 4.20:** Voltage plotted against the gravimetric capacity of the formation cycles of the best performing full cell of A:PAA_C:PVDF (a), A:PVDF_C:CMCSBR (b), A:PAA_C:CMCSBR (c) and A:PVDF_C:PVDF (d).

After cycling the full cells in the combination test at a voltage range of 2.7-3.8V, the cells were cycled at a voltage range of 2.7-4.2V at room temperature to determine if increasing the potential window would increase the overall discharge capacity. Figure 4.18b depicts the results of the subsequent test. In general, no significant capacity increase in the larger voltage window can be observed. The capacity curve of A:PAA_C:PVDF shows the highest initial capacity, but the capacity retention stability decreased and eventually stabilised at a capacity retention of 14.4% (compared to the theoretical capacity for charging up to 3.8V). The A:PVDF_C:PVDF cell has the highest retained capacity (14%) despite showing poor discharge capacities in the smaller voltage window. Discharge capacities from the other two cells end up lower compared to prior discharge capacities in the combination test.

| | $\text{Capacity}_{AVG}$ (mAh/cm$^2$) | $\text{CE}_{AVG}$ (%) |
|---|---|---|
| A:PAA_C:PVDF | 3.38 | 96 |
| A:PVDF_C:CMCSBR | 3.51 | 91 |
| A:PAA_C:CMCSBR | 3.34 | 92 |
| A:PVDF_C:PVDF | 3.26 | 98 |

**Table 4.5:** Average theoretical capacities of the full cells and the average coulombic efficiency over 50 cycles in the capacity window 2.7-4.2V.

In table 4.5 the average CE of the cycles during cycling in a voltage of 2.7-4.2V can be seen. However, with these kind of coulombic efficiencies, there should not be that much capacity left after so many cycles. The $Li^+$ reservoir on the cathode side is not completely delithiated in each cycle. Consequently, the positive electrode can still provide capacity in the later cycles. Furthermore, the electrolyte salt is able to provide for relatively high CE's and is therefore not suspected to be the main bottleneck of the general capacity decrease.

**Conclusion:** When looking at the results of the previous half cell experiments, the best electrode combi-

nation in a full cell would be a PVDF based anode and a CMC/SBR based cathode (A:PVDF_C:CMCSBR). In the full cell combination test, this ideal electrode combination only performed the best in the early stages of cycling. In the smaller voltage operating window (2.7-3.8V), the A:PVDF_C:CMCSBR cell performed third best of the full cells. At cycle 100, A:PAA_C:CMCSBR showed the highest capacity retention: 14.4%. It could be argued, because the full cells all have to cope with the same degradation mechanism, that the fluorine free binder combination (A:PAA_C:CMCSBR) prevailed the best and the PVDF based full cell (A:PVDF_C:PVDF, the positive control) the worst.
After 50 subsequent cycles in the larger voltage window (2.7-4.2V), A:PVDF_C:PVDF eventually showed the highest capacity retained (14%). An initial capacity depletion of around 40% was observed and is suspected to be the result of electrolyte oxidation at the cathode and the subsequent reduction of these oxidative species at the anode. The question remains why this was possible in the first place with electrolyte additives within the electrolyte solution.

### 4.5.1. Fluorine free full cells

Full cells constituted of only fluorine free (F-free) compounds were tested in a 3-point electrode flange cell. The third electrode acted as the reference electrode and monitored the potential at the anode side. The reference electrode consisted of a copper wire with a the lithium piece at the end of this wire. However, the lithium piece stuck to the electrolyte wetted separator and was separated from the copper reference wire. Therefore, no usable reference signal was obtained during cycling of the flange cells.
Figure 4.21a depicts the discharge capacities per cycle for the F-free full cell. The same protocol was executed that was used for the binder combination test, but at room temperature: 3 formation cycles (0.1C, 2.7-4.2V) followed by 100 cycles (2.7-3.8V) with charging at 0.1 followed by a constant voltage charge step and discharging at 0.33C.

After the first charge, a lower capacity fade is observed when comparing it to the capacity fade for the fulls cells in the combination test. The F-free cells lose around 30% capacity after the first charge, while having a similar loading as the full cells with $LiPF_6$. Also, for the F-free cells, the formation cycles appear to be more stable with regard to capacity retention,but do not show a similar cycling stability. The cells end up at 6% capacity retained after 100 cycles in a operating voltage window of 2.7-3.8V and have only 2% capacity retained when comparing it to the theoretical capacity. In table 4.6 the theoretical capacity and the average coulombic efficiency per flange cell is shown.

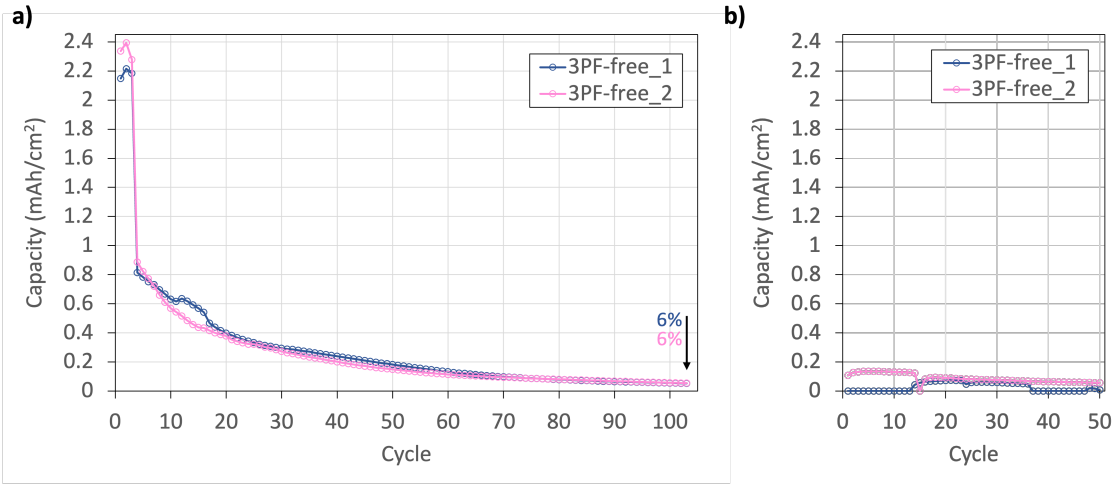


**Figure 4.21:** Discharge capacity per cycle for fluorine free full cells (flange cell), 3 formation cycles (2.7V-4.2V) followed by cycling between 2.7V and 3.8 (a) and the subsequent cycling between 2.7V and 4.2V (b).

To see if the capacity decrease had to do with the first charge, the voltage curves of the formation cycles are shown in figure 4.22. Here, two dips can be seen at around 2.5V and 3V, corresponding to the intended reduction of the DTD (figure 4.19. However, this does not explain the capacity fade. Moreover, 3PF-free_1 does not charge all the way to 200 mAh/g on the first charge, which could indicate that already a part of the active material was lost. 3PF-free_1 exhibits a first charge capacity

of 210 mAh/g.

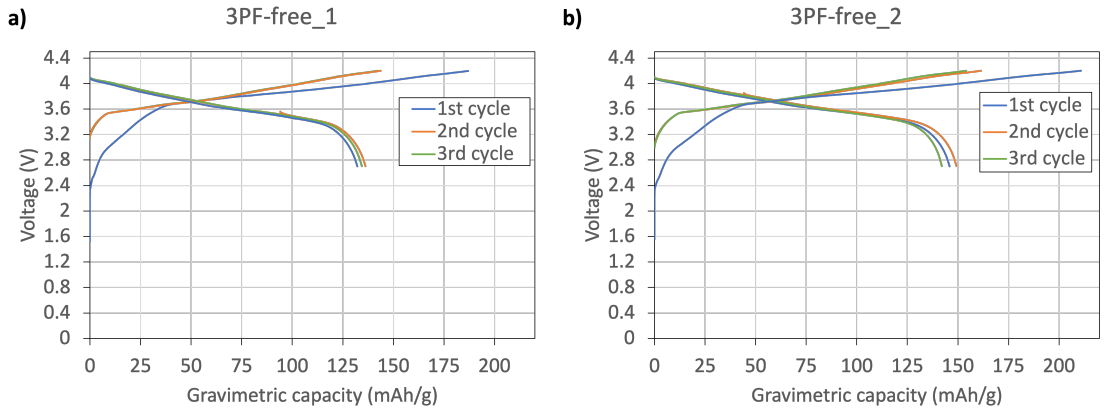


**Figure 4.22:** Voltage plotted against the gravimetric capacity of the formation cycles of the best performing full cell of 3PF-free_1 (a) and 3PF-free_2 (b).

After cycling, the flange cells were opened to see if the electrolyte had dried up. Dried up electrolyte is known for causing capacity decrease during cycling, because then the ionic diffusion from one side to the other of cell is not supported anymore. In initial test with the flange cell, the electrolyte would sometimes dry out. It was suspect that this was due to deficits on the surface of the flange which made contact with the O-ring. Because of these deficits, the cell would not be completely air tight. This in turn would allow for electrolyte to react with the oxygen and form byproducts, hence drying out. However, no apparent drying out was visible. After closing the the flange cells they were cycled for another 50 cycles at a larger voltage window (2.7-4.2V), but this resulted not in a significant capacity increase(see figure 4.21b). Notably, misalignment of the electrodes in the flange cell may have had a large negative impact on this last capacity retention test. The misalignment of electrodes prevents the full utilisation of the electrode surface, because only the aligned electrodes surfaces will interact in the redox reaction.

| | Capacity (mAh/cm$^2$) | CE$_{AVG}$ (%) |
|---|---|---|
| 3PF-free_1 | 3.2 | 91 |
| 3PF-free_2 | 3.3 | 90 |

**Table 4.6:** Theoretical capacities of the fluorine free full cells tested and average the coulombic efficiency over 100 cycles.

In figure 4.23 a comparison is made regarding the voltage profile between the last formation cycles of the fluorine free full cells of the combination test and the fluorine free flange cells. Higher overpotentials in the A:PAA_C:CMCSBR cells are the dominant factor for reaching the cut-off potential earlier.

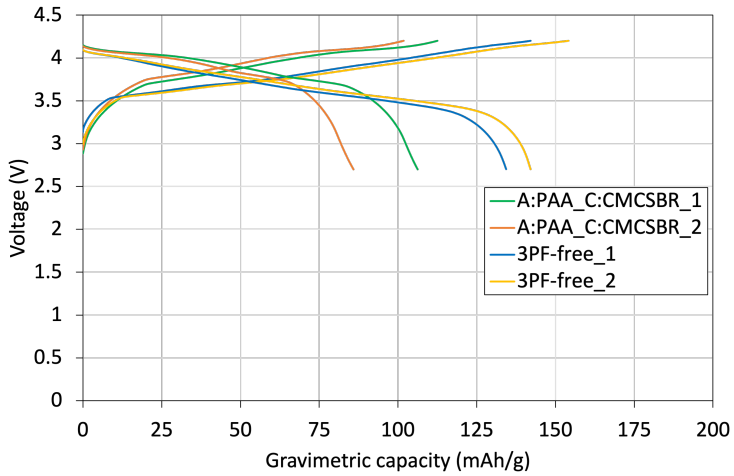


**Figure 4.23:** Voltage curves plotted against the gravimetric capacity of the last formation cycles of the half cell F-free flange cells and of the A:PAA_C:CMCSBR full cells

Apart from the used cell configuration, the electrolyte and the temperature at which they cycled, the cells are almost identical. Conventionally speaking, cycling at elevated temperatures enhances charge transfer kinetics in the cell and also increases the conductivity of the electrolyte [89]. In addition, the flange cell is a more experimental cell set-up than the commercially used coin cell. This risks the flange cell to be more prone for failure. Therefore, the difference in electrolyte composition is suspected of the main reason for the difference in capacity during the last formation cycle. Lack in providing ion transport can increase the degree of overpotentials in the cells. A study by Xu, Kang reports that LiBOB in an organic solvent results in higher resistance at the graphite-electrolyte interface when comparing it to $LiPF_6$ in a benchmark electrolyte solution (EC/EMC (50:50)) [94]. This contradicts the earlier made assumption that the electrolyte was the main bottleneck of the capacity depletion. In figure 4.24 similar discharge capacities can be observed between two LFP half cells (1.36 mAh/cm$^2$ that have LiBOB or $LiPF_6$ as the electrolyte. A large dip can be seen for the LiBOB cell, this was due to a voltage shift to 3.65V at OCP in the resting step. Because of this, a smaller charge step could be performed, resulting in a lower discharge capacity. Overall, $LiPF_6$ performs more stable in terms of capacity retention. The cycling stability of the LiBOB cell is restricted by the larger overpotentials. This corresponds also with the full cell using $LiPF_6$ as an electrolyte compared to the fluorine free full cell configuration which uses LiBOB as the electrolyte.

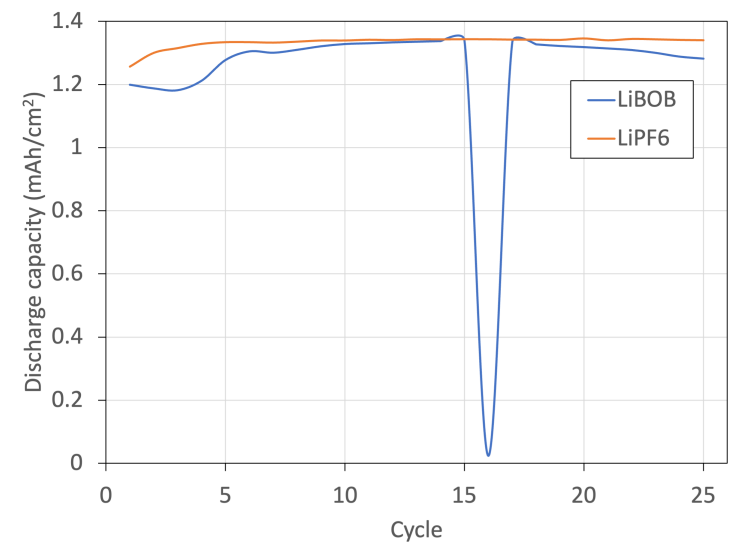


**Figure 4.24:** Discharge capacity per cycle for LFP half cells with LiBOB and $LiPF_6$ as the electrolyte salt.

In this current study, the electrolyte based on LiBOB additionally contained the additive DTD which enhances the SEI stability. In figure 4.25 the effect of the addition of DTD on the discharge capacity is shown. All the cells have a theoretical capacity of 1.36 mAh/cm$^2$. Initially, for both LFP v graphite cell variants the discharge capacity is around 45% of what the first charge could provide in terms of capacity. The initial drop in capacity retention is comparable to that of the NMC811 based full cells with $LiPF_6$ as the electrolyte. However, the first charge for the LFP cells does not overshoot its rated capacity. This indicates that the depletion of the capacity is related to the operating voltage of the CAM and thus with the release of electrons from the active material during the first charge.
The consequent cycles are more stable and show even an increase in discharge capacity for the LFP based full cells due to a lower polarisation. The cells without DTD (no DTD) show a higher discharge capacity in the early cycling stage, but in the later stages of cycling the capacity retention drops below that of the DTD containing cells. In addition, several dips can be seen in the discharge capacity curves. These dips originated from side reactions and became apparent by analysing the voltage curve. On average, the CE for the DTD containing cells is very close to 100%, for the cells without DTD it is around 97%. When considering the aforementioned differences between the cells with and without DTD, the addition of DTD shows to be beneficial for the overall performance of the cell.

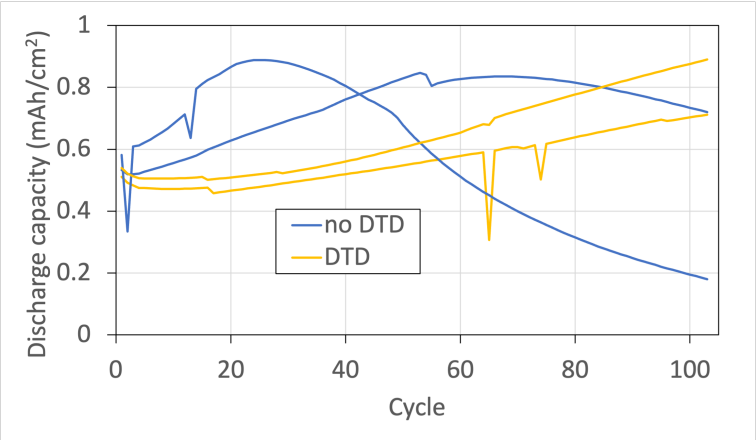


**Figure 4.25:** Discharge capacity per cycle for LFP vs graphite full cells with and without the additive DTD in the electrolyte solution

**Conclusion:** Considering the results of the fluorine free full cells and the LFP test cells, the following can be highlighted; The fluorine free full cells showed promising initial results This is because the fluorine free cells had relatively high initial discharge capacities compared to the "not completely fluorine free" full cells in the binder test, but showed a lower capacity retention over a longer period. The capacity retained after 100 cycles in a operating voltage window was only 2%. Furthermore, similar to the full cells in the binder combination test, the fluorine free cells suffered from an initial capacity fade in the first discharge. Using $LiPF_6$ as an electrolyte in the LFP test cells resulted in a higher capacity retention stability compared to the LiBOB test cell. In addition, the DTD containing LiBOB LFP test cells showed better performance than the LFP test cells without DTD in the electrolyte mixture. Further investigation would be needed to find out why the $LiPF_6$ based full cells in the binder combination test showed lower initial discharge capacities, compared to LiBOB based full cells.

# 5
# Conclusion

**Processing:**

In terms of general electrode fabrication, processing of the electrodes with different binders resulted in smooth and strong electrodes. However, when PAA containing cathodes were processed with the phase inversion treatment this resulted in delamination from the current collector. Moreover, conventionally dried PAA containing cathodes bound very strongly to the current collector. This resulted in a deformed electrode structure.

**Graphite vs Lithium:**

In the **anode rate performance** cycling test, the conventionally dried PAA based graphite half cell (PAA_CONVA1) showed enhanced rate performance characteristics compared to the other PAA, PVDF and PES based electrodes. PAA_CONVA showed a capacity retention of 39% at a C-rate of 4C. In general, PAA based electrodes showed the lowest polarisation voltages at higher current densities, resulting in higher discharge capacities. Phase inversion treated electrodes had a high charge transfer resistance and consequently did not facilitate enhanced performance at higher current densities compared to the conventionally dried electrodes.

In the **anode long term performance** cycling test, the PVDF based cells showed the highest capacity retention, but phase inversion treated PVDF based cells performed less well. The conventionally dried PVDF based graphite half cell retained a stable capacity up to cycle 70, after 100 cycles the retained capacity was 24%. The difference in electrode processing for PAA based electrodes did not have a conclusive alternate effect. The loading of PAA based cells seemed to have the largest impact on the capacity retention of the cells. The grade of the electrolyte played a major role between the two sample. Eventually, depletion of the electrolyte salt was the bottleneck of the overall performance of the cells.

**NMC811 vs Lithium:**

In the **cathode rate performance** cycling test, the PVDF based positive electrodes performed the best in the rate performance cycling tests, exhibiting a capacity retention of 54% at a C-rate of 2C and showing 100% in the recovery cycles (0.1C). Predominantly CMC/SBR based cathodes showed high discharge capacities a the recovery cycles, being around 95%. However, the capacity fade was from a C-rate of 1C already severe. Especially for the phase inversion treated CMC/SBR based cells the capacity fade was the highest due to decreased ionic diffusion in the liquid phase. These cell showed only reasonable capacity (72%) up to a C-rate of 0.33C. The non-uniform electrode structure of PAA and CMC/PAA based electrodes negatively impacted their overall available capacity and performance. PVDF based cells showed capacity at C-rates up to 2C, but the other cells showed complete capacity depletion at C-rate of 2C (or lower).

In the **cathode long term performance** cycling test, the conventionally dried CMC/SBR based cell showed the highest capacity retention (60%) after 106 cycles, despite suffering from higher a polarisation voltage compared to PVDF based cells. Thickness and porosity were suspected to be the main driver behind this polarisation. In general, conventionally treated electrodes showed better results than the phase inversion treated ones. However, the phase inversion treated CMC/SBR cell showed comparable

recovery discharge capacities compared to the conventionally treated electrode based cells.

**Graphite vs NMC811:**

Looking at the results of the half cell experiments, the best electrode combination in a full cell would be a PVDF based anode and a CMC/SBR based cathode (A:PVDF_C:CMCSBR). Only in the early stages of cycling this ideal combination showed enhanced performance. After 100 cycles in an operating window of 2.7-3.8V, (A:PAA_C:CMCSBR) showed the highest capacity retention (14.4%) and coped the best with the degradation of the performance. Subsequently, the full cells with a PVDF based anode and cathode showed the highest capacity retention after 50 cycles (2.7-4.2), being 14%. A severe initial capacity fade (40%) was observed for all cells in the first discharge. The capacity degradation is suspected to be the result of electrolyte oxidation at the cathode and subsequent reduction of these oxidative species at the anode. However, it is not yet clear why this was possible while using electrolyte additives. Consequently, it is difficult to compare the real performance various cells.

**Fluorine free full cell:**

Fluorine free full cells using a PAA based anode, a CMC/SBR based cathode and a LiBOB based electrolyte showed promising initial results by outperforming the equivalent ($LiPF_6$ containing) full cells in the first few cycles. However, for the fluorine free cells the capacity retention stability was much lower over a longer cycling period, being only 2% after 100 cycles in a voltage window of 2.7-3.8V. Similar to the full cells in the binder combination test, the fluorine free cells suffered from an initial capacity fade in the first discharge. LFP test cells containing $LiPF_6$ as electrolyte showed higher capacity retention stability opposed to cells containing LiBOB. DTD containing LiBOB LFP test cells showed enhance performance over cells without DTD in the electrolyte mixture.

**General:**

It is difficult to provide a definite conclusion to the research question: Are there viable alternatives for fluorine rich batteries?. The reason for this is that the positive control in the full cell configuration, also suffered from initial capacity degradation, making it difficult to determine the actual performance of the full cells based on the different binders. However, it can be stated that the electrodes based on fluorine free binders showed promising potential to be explored in future research.

# 6

# Recommendations

- Use more samples per test to increase the validity of the results.
- Use lower and comparable cell loadings to better understand the effects of the binder on the electrochemical performance of the cell.
- Analyse the internal structure difference between conventionally dried and phase inversion treated electrodes using SEM.
- Conduct analysis using X-ray photoelectron spectroscopy (XPS) before and after cycling to better understand the electrolyte degradation products as well as the formation of unwanted products on the surface of the anode and cathode.
- Investigate the reason for the initial capacity depletion of full cells utilising an electrolyte with SEI stabilising additives.
- Use three point electrodes to better understand the failure mechanisms in a full cell.

# References


[1] European Chemicals Agency. URL: https://echa.europa.eu/brief-profile/-/briefprofile/100.104.534. (visited 01/05/2024).

[2] David Allart, Maxime Montaru, and Hamid Gualous. "Model of Lithium Intercalation into Graphite by Potentiometric Analysis with Equilibrium and Entropy Change Curves of Graphite Electrode". In: *Journal of The Electrochemical Society* 165.2 (2018), A380–A387. ISSN: 0013-4651, 1945-7111. DOI: 10.1149/2.1251802jes. URL: https://iopscience.iop.org/article/10.1149/2.1251802jes (visited on 01/06/2024).

[3] Seong Jin An et al. "The state of understanding of the lithium-ion-battery graphite solid electrolyte interphase (SEI) and its relationship to formation cycling". In: *Carbon* 105 (Aug. 2016), pp. 52–76. ISSN: 00086223. DOI: 10.1016/j.carbon.2016.04.008. URL: https://linkinghub.elsevier.com/retrieve/pii/S0008622316302676 (visited on 09/13/2023).

[4] Seong Jin An et al. "The state of understanding of the lithium-ion-battery graphite solid electrolyte interphase (SEI) and its relationship to formation cycling". In: *Carbon* 105 (2016), pp. 52–76.

[5] D Aurbach et al. "On the use of vinylene carbonate (VC) as an additive to electrolyte solutions for Li-ion batteries". In: *Electrochimica Acta* 47.9 (Feb. 2002), pp. 1423–1439. ISSN: 00134686. DOI: 10.1016/S0013-4686(01)00858-1. URL: https://linkinghub.elsevier.com/retrieve/pii/S0013468601008581 (visited on 12/29/2023).

[6] Alberto Betancourt-Torcat, Tuhin Poddar, and Ali Almansoori. "A realistic framework to a greener supply chain for electric vehicles". In: *International Journal of Energy Research* 43.6 (May 2019), pp. 2369–2390. ISSN: 0363907X. DOI: 10.1002/er.4373. URL: https://onlinelibrary.wiley.com/doi/10.1002/er.4373 (visited on 01/06/2024).

[7] Boris Bitsch et al. "A novel slurry concept for the fabrication of lithium-ion battery electrodes with beneficial properties". In: *Journal of Power Sources* 265 (Nov. 2014), pp. 81–90. ISSN: 03787753. DOI: 10.1016/j.jpowsour.2014.04.115. URL: https://linkinghub.elsevier.com/retrieve/pii/S0378775314006168 (visited on 01/06/2024).

[8] Dominic Bresser et al. "Alternative binders for sustainable electrochemical energy storage – the transition to aqueous electrode processing and bio-derived polymers". In: *Energy & Environmental Science* 11.11 (2018), pp. 3096–3127. ISSN: 1754-5692, 1754-5706. DOI: 10.1039/C8EE00640G. URL: http://xlink.rsc.org/?DOI=C8EE00640G (visited on 01/03/2024).

[9] H. Buqa et al. "Study of styrene butadiene rubber and sodium methyl cellulose as binder for negative electrodes in lithium-ion batteries". In: *Journal of Power Sources* 161.1 (Oct. 2006), pp. 617–622. ISSN: 03787753. DOI: 10.1016/j.jpowsour.2006.03.073. URL: https://linkinghub.elsevier.com/retrieve/pii/S037877530600591X (visited on 12/30/2023).

[10] J. C. Burns, D. A. Stevens, and J. R. Dahn. "In-Situ Detection of Lithium Plating Using High Precision Coulometry". In: *Journal of The Electrochemical Society* 162.6 (2015), A959–A964. ISSN: 0013-4651, 1945-7111. DOI: 10.1149/2.0621506jes. URL: https://iopscience.iop.org/article/10.1149/2.0621506jes (visited on 01/04/2024).

[11] J. C. Burns et al. "Predicting and Extending the Lifetime of Li-Ion Batteries". In: *Journal of The Electrochemical Society* 160.9 (2013), A1451–A1456. ISSN: 0013-4651, 1945-7111. DOI: 10.1149/2.060309jes. URL: https://iopscience.iop.org/article/10.1149/2.060309jes (visited on 02/06/2024).

[12] Hao Chen et al. "Exploring Chemical, Mechanical, and Electrical Functionalities of Binders for Advanced Energy-Storage Devices". In: *Chemical Reviews* 118.18 (Sept. 26, 2018), pp. 8936–8982. ISSN: 0009-2665, 1520-6890. DOI: 10.1021/acs.chemrev.8b00241. URL: https://pubs.acs.org/doi/10.1021/acs.chemrev.8b00241 (visited on 01/07/2024).

[13] Zhiqiang Chen et al. “Overpotential analysis of graphite-based Li-ion batteries seen from a porous electrode modeling perspective”. In: *Journal of Power Sources* 509 (Oct. 2021), p. 230345. ISSN: 03787753. DOI: 10.1016/j.jpowsour.2021.230345. URL: https://linkinghub.elsevier.com/retrieve/pii/S0378775321008570 (visited on 01/29/2024).

[14] Zhiqiang Chen et al. “Reaction-rate distribution at large currents in porous electrodes”. In: *Journal of Power Sources* 581 (Oct. 2023), p. 233495. ISSN: 03787753. DOI: 10.1016/j.jpowsour.2023.233495. URL: https://linkinghub.elsevier.com/retrieve/pii/S0378775323008716 (visited on 01/29/2024).

[15] Aleksander Cholewinski et al. “Polymer Binders: Characterization and Development toward Aqueous Electrode Fabrication for Sustainability”. In: *Polymers* 13.4 (Feb. 20, 2021), p. 631. ISSN: 2073-4360. DOI: 10.3390/polym13040631. URL: https://www.mdpi.com/2073-4360/13/4/631 (visited on 11/15/2023).

[16] Fabrice M Courtel et al. “Water-soluble binders for MCMB carbon anodes for lithium-ion batteries”. In: *Journal of Power Sources* 196.4 (2011), pp. 2128–2134.

[17] Jie Deng et al. “Electric Vehicles Batteries: Requirements and Challenges”. In: *Joule* 4.3 (Mar. 2020), pp. 511–515. ISSN: 25424351. DOI: 10.1016/j.joule.2020.01.013. URL: https://linkinghub.elsevier.com/retrieve/pii/S254243512030043X (visited on 01/04/2024).

[18] Zhongwei Deng et al. “General Discharge Voltage Information Enabled Health Evaluation for Lithium-Ion Batteries”. In: *IEEE/ASME Transactions on Mechatronics* 26.3 (June 2021), pp. 1295–1306. ISSN: 1083-4435, 1941-014X. DOI: 10.1109/TMECH.2020.3040010. URL: https://ieeexplore.ieee.org/document/9268111/ (visited on 01/06/2024).

[19] V Dharmalingam et al. “Antagonistic effects of polyacrylic acid with Sodium gluconate and Zn2+ for corrosion control of mild steel in aqueous solution”. In: *Int. J. Nano. Corr. Sci. Engg* 2.5 (2015), pp. 11–24.

[20] Zhijia Du et al. “Understanding limiting factors in thick electrode performance as applied to high energy density Li-ion batteries”. In: *Journal of Applied Electrochemistry* 47.3 (Mar. 2017), pp. 405–415. ISSN: 0021-891X, 1572-8838. DOI: 10.1007/s10800-017-1047-4. URL: http://link.springer.com/10.1007/s10800-017-1047-4 (visited on 01/28/2024).

[21] A Du Pasquier et al. “Differential scanning calorimetry study of the reactivity of carbon anodes in plastic Li-ion batteries”. In: *Journal of the Electrochemical Society* 145.2 (1998), p. 472.

[22] L. El Ouatani et al. “The Effect of Vinylene Carbonate Additive on Surface Film Formation on Both Electrodes in Li-Ion Batteries”. In: *Journal of The Electrochemical Society* 156.2 (2009), A103. ISSN: 00134651. DOI: 10.1149/1.3029674. URL: https://iopscience.iop.org/article/10.1149/1.3029674 (visited on 12/29/2023).

[23] M Faizal et al. “A review on challenges and opportunities of electric vehicles (evs)”. In: *J. Mech. Eng. Res. Dev* 42.4 (2019), pp. 130–137.

[24] Miran Gaberscek et al. “Improved carbon anode for lithium batteries pretreatment of carbon particles in a polyelectrolyte solution”. In: *Electrochemical and Solid-State Letters* 3.4 (2000), p. 171.

[25] Miran Gaberšček. *IMPEDANCE SPECTROSCOPY: basic principles and simple analysis of bulk and interfacial properties.*

[26] Kevin G. Gallagher et al. “Optimizing Areal Capacities through Understanding the Limitations of Lithium-Ion Electrodes”. In: *Journal of The Electrochemical Society* 163.2 (2016), A138–A149. ISSN: 0013-4651, 1945-7111. DOI: 10.1149/2.0321602jes. URL: https://iopscience.iop.org/article/10.1149/2.0321602jes (visited on 01/04/2024).

[27] N. . Galushkin, N. N. Yazvinskaya, and D. N. Galushkin. “Mechanism of Gases Generation during Lithium-Ion Batteries Cycling”. In: *Journal of The Electrochemical Society* 166.6 (2019), A897–A908. ISSN: 0013-4651, 1945-7111. DOI: 10.1149/2.0041906jes. URL: https://iopscience.iop.org/article/10.1149/2.0041906jes (visited on 02/06/2024).

[28] Jean-Baptiste Gieu et al. “Influence of Vinylene Carbonate Additive on the Li $_4$ Ti $_5$ O $_{12}$ Electrode/Electrolyte Interface for Lithium-Ion Batteries”. In: *Journal of The Electrochemical Society* 164.6 (2017), A1314–A1320. ISSN: 0013-4651, 1945-7111. DOI: 10.1149/2.0111707jes. URL: https://iopscience.iop.org/article/10.1149/2.0111707jes (visited on 12/29/2023).

[29] A Guerfi et al. “LiFePO4 water-soluble binder electrode for Li-ion batteries”. In: *Journal of Power Sources* 163.2 (2007), pp. 1047–1052.

[30] Peter-Paul R.M.L. Harks et al. “Immersion precipitation route towards high performance thick and flexible electrodes for Li-ion batteries”. In: *Journal of Power Sources* 441 (Nov. 2019), p. 227200. ISSN: 03787753. DOI: 10.1016/j.jpowsour.2019.227200. URL: https://linkinghub.elsevier.com/retrieve/pii/S0378775319311930 (visited on 09/13/2023).

[31] Peter-Paul RML Harks et al. “Immersion precipitation route towards high performance thick and flexible electrodes for Li-ion batteries”. In: *Journal of power sources* 441 (2019), p. 227200.

[32] W Blake Hawley et al. “Lithium and transition metal dissolution due to aqueous processing in lithium-ion battery cathode active materials”. In: *Journal of Power Sources* 466 (2020), p. 228315.

[33] Guiomar Hernández et al. “Elimination of Fluorination: The Influence of Fluorine-Free Electrolytes on the Performance of LiNi $_{1/3}$ Mn $_{1/3}$ Co $_{1/3}$ O $_2$ /Silicon–Graphite Li-Ion Battery Cells”. In: *ACS Sustainable Chemistry & Engineering* 8.27 (July 13, 2020), pp. 10041–10052. ISSN: 2168-0485, 2168-0485. DOI: 10.1021/acssuschemeng.0c01733. URL: https://pubs.acs.org/doi/10.1021/acssuschemeng.0c01733 (visited on 01/05/2024).

[34] Guiomar Hernández et al. “Fluorine-Free Electrolytes for Lithium and Sodium Batteries”. In: *Batteries & Supercaps* 5.6 (June 2022), e202100373. ISSN: 2566-6223, 2566-6223. DOI: 10.1002/batt.202100373. URL: https://chemistry-europe.onlinelibrary.wiley.com/doi/10.1002/batt.202100373 (visited on 11/06/2023).

[35] Christian Heubner et al. “Recent Insights into Rate Performance Limitations of Li-ion Batteries”. In: *Batteries & Supercaps* 4.2 (Feb. 2021), pp. 268–285. ISSN: 2566-6223, 2566-6223. DOI: 10.1002/batt.202000227. URL: https://chemistry-europe.onlinelibrary.wiley.com/doi/10.1002/batt.202000227 (visited on 01/09/2024).

[36] Yi-Xin Huang et al. “1,3,2-Dioxathiolane 2,2-Dioxide as a Bifunctional Electrolyte Additive to Enhance the Stability of Lithium Metal Anodes”. In: *ACS Sustainable Chemistry & Engineering* 11.9 (Mar. 6, 2023), pp. 3760–3768. ISSN: 2168-0485, 2168-0485. DOI: 10.1021/acssuschemeng.2c06824. URL: https://pubs.acs.org/doi/10.1021/acssuschemeng.2c06824 (visited on 12/29/2023).

[37] Hayata Isozumi et al. “Application of modified styrene-butadiene-rubber-based latex binder to high-voltage operating LiCoO2 composite electrodes for lithium-ion batteries”. In: *Journal of Power Sources* 468 (Aug. 2020), p. 228332. ISSN: 03787753. DOI: 10.1016/j.jpowsour.2020.228332. URL: https://linkinghub.elsevier.com/retrieve/pii/S0378775320306364 (visited on 12/30/2023).

[38] Hayata Isozumi et al. “Impact of Newly Developed Styrene–Butadiene–Rubber Binder on the Electrode Performance of High-Voltage LiNi $_{0.5}$ Mn $_{1.5}$ O $_4$ Electrode”. In: *ACS Applied Energy Materials* 3.8 (Aug. 24, 2020), pp. 7978–7987. ISSN: 2574-0962, 2574-0962. DOI: 10.1021/acsaem.0c01334. URL: https://pubs.acs.org/doi/10.1021/acsaem.0c01334 (visited on 12/30/2023).

[39] Søren Højgaard Jensen, Kurt Engelbrecht, and Carlos Bernuy-Lopez. “Measurements of Electric Performance and Impedance of a 75 Ah NMC Lithium Battery Module”. In: *Journal of The Electrochemical Society* 159.6 (2012), A791–A797. ISSN: 0013-4651, 1945-7111. DOI: 10.1149/2.088206jes. URL: https://iopscience.iop.org/article/10.1149/2.088206jes (visited on 02/08/2024).

[40] Fabian Jeschull, Matthew J. Lacey, and Daniel Brandell. “Functional binders as graphite exfoliation suppressants in aggressive electrolytes for lithium-ion batteries”. In: *Electrochimica Acta* 175 (Sept. 2015), pp. 141–150. ISSN: 00134686. DOI: 10.1016/j.electacta.2015.03.072. URL: https://linkinghub.elsevier.com/retrieve/pii/S0013468615006696 (visited on 01/03/2024).

[41] J. Jiang and J. R. Dahn. "Comparison of the Thermal Stability of Lithiated Graphite in LiBOB EC/DEC and in LiPF[sub 6] EC/DEC". In: *Electrochemical and Solid-State Letters* 6.9 (2003), A180. ISSN: 10990062. DOI: 10.1149/1.1592911. URL: https://iopscience.iop.org/article/10.1149/1.1592911 (visited on 01/05/2024).

[42] Roland Jung et al. "Oxygen Release and Its Effect on the Cycling Stability of LiNi $_x$ Mn $_y$ Co $_z$ O $_2$ (NMC) Cathode Materials for Li-Ion Batteries". In: *Journal of The Electrochemical Society* 164.7 (2017), A1361–A1377. ISSN: 0013-4651, 1945-7111. DOI: 10.1149/2.0021707jes. URL: https://iopscience.iop.org/article/10.1149/2.0021707jes (visited on 01/05/2024).

[43] Felix Katzer et al. "Analyses of polarisation effects and operando detection of lithium deposition in experimental half- and commercial full-cells". In: *Electrochimica Acta* 436 (Dec. 2022), p. 141401. ISSN: 00134686. DOI: 10.1016/j.electacta.2022.141401. URL: https://linkinghub.elsevier.com/retrieve/pii/S0013468622015584 (visited on 02/13/2024).

[44] Kyung Hoon Kim et al. "A key strategy to form a LiF-based SEI layer for a lithium-ion battery anode with enhanced cycling stability by introducing a semi-ionic C F bond". In: *Journal of Industrial and Engineering Chemistry* 99 (July 2021), pp. 48–54. ISSN: 1226086X. DOI: 10.1016/j.jiec.2021.04.002. URL: https://linkinghub.elsevier.com/retrieve/pii/S1226086X21001775 (visited on 12/29/2023).

[45] Hiroki Kondo and Venkat Srinivasan. "Simulation study of rate limiting factors of Li-ion batteries using experimental functions of electronic and ionic resistances". In: *Electrochimica Acta* 371 (Mar. 2021), p. 137834. ISSN: 00134686. DOI: 10.1016/j.electacta.2021.137834. URL: https://linkinghub.elsevier.com/retrieve/pii/S0013468621001237 (visited on 11/13/2023).

[46] Jia-He Kuo and Chia-Chen Li. "Water-based process to the preparation of nickel-rich Li (Ni0. 8Co0. 1Mn0. 1) O2 cathode". In: *Journal of The Electrochemical Society* 167.10 (2020), p. 100504.

[47] Jia-He Kuo and Chia-Chen Li. "Water-Based Process to the Preparation of Nickel-Rich Li(Ni $_{0.8}$ Co $_{0.1}$ Mn $_{0.1}$ )O $_2$ Cathode". In: *Journal of The Electrochemical Society* 167.10 (June 1, 2020), p. 100504. ISSN: 1945-7111. DOI: 10.1149/1945-7111/ab95c5. URL: https://iopscience.iop.org/article/10.1149/1945-7111/ab95c5 (visited on 10/24/2023).

[48] Jianlin Li et al. "From Materials to Cell: State-of-the-Art and Prospective Technologies for Lithium-Ion Battery Electrode Processing". In: *Chemical Reviews* 122.1 (Jan. 12, 2022), pp. 903–956. ISSN: 0009-2665, 1520-6890. DOI: 10.1021/acs.chemrev.1c00565. URL: https://pubs.acs.org/doi/10.1021/acs.chemrev.1c00565 (visited on 10/23/2023).

[49] Jianlin Li et al. "From materials to cell: state-of-the-art and prospective technologies for lithium-ion battery electrode processing". In: *Chemical Reviews* 122.1 (2021), pp. 903–956.

[50] Ming-Qi Li et al. "Electrochemical Performance of Si/Graphite/Carbon Composite Electrode in Mixed Electrolytes Containing LiBOB and LiPF[sub 6]". In: *Journal of The Electrochemical Society* 156.4 (2009), A294. ISSN: 00134651. DOI: 10.1149/1.3076196. URL: https://iopscience.iop.org/article/10.1149/1.3076196 (visited on 12/29/2023).

[51] Tao Li et al. "Fluorinated Solid-Electrolyte Interphase in High-Voltage Lithium Metal Batteries". In: *Joule* 3.11 (Nov. 2019), pp. 2647–2661. ISSN: 25424351. DOI: 10.1016/j.joule.2019.09.022. URL: https://linkinghub.elsevier.com/retrieve/pii/S2542435119304829 (visited on 12/29/2023).

[52] Xifei Li et al. "Atomic layer deposition of solid-state electrolyte coated cathode materials with superior high-voltage cycling behavior for lithium ion battery application". In: *Energy Environ. Sci.* 7.2 (2014), pp. 768–778. ISSN: 1754-5692, 1754-5706. DOI: 10.1039/C3EE42704H. URL: http://xlink.rsc.org/?DOI=C3EE42704H (visited on 01/19/2024).

[53] Yong Li, Jie Yang, and Jian Song. "Design structure model and renewable energy technology for rechargeable battery towards greener and more sustainable electric vehicle". In: *Renewable and Sustainable Energy Reviews* 74 (July 2017), pp. 19–25. ISSN: 13640321. DOI: 10.1016/j.rser.2017.02.021. URL: https://linkinghub.elsevier.com/retrieve/pii/S136403211730223X (visited on 01/06/2024).

[54] Niranjanmurthi Lingappan, Lingxi Kong, and Michael Pecht. "The significance of aqueous binders in lithium-ion batteries". In: *Renewable and Sustainable Energy Reviews* 147 (Sept. 2021), p. 111227. ISSN: 13640321. DOI: 10.1016/j.rser.2021.111227. URL: https://linkinghub.elsevier.com/retrieve/pii/S1364032121005141 (visited on 11/14/2023).

[55] Hossein Maleki et al. "Thermal Stability Studies of Binder Materials in Anodes for Lithium-Ion Batteries". In: *Journal of The Electrochemical Society* 147.12 (2000), p. 4470. ISSN: 00134651. DOI: 10.1149/1.1394088. URL: https://iopscience.iop.org/article/10.1149/1.1394088 (visited on 09/04/2023).

[56] Hossein Maleki et al. "Thermal stability studies of binder materials in anodes for lithium-ion batteries". In: *Journal of the Electrochemical Society* 147.12 (2000), p. 4470.

[57] Katharina Märker et al. "Evolution of Structure and Lithium Dynamics in LiNi $_{0.8}$ Mn $_{0.1}$ Co $_{0.1}$ O $_{2}$ (NMC811) Cathodes during Electrochemical Cycling". In: *Chemistry of Materials* 31.7 (Apr. 9, 2019), pp. 2545–2554. ISSN: 0897-4756, 1520-5002. DOI: 10.1021/acs.chemmater.9b00140. URL: https://pubs.acs.org/doi/10.1021/acs.chemmater.9b00140 (visited on 01/05/2024).

[58] Michael Metzger et al. "Origin of H $_{2}$ Evolution in LIBs: H $_{2}$ O Reduction vs. Electrolyte Oxidation". In: *Journal of The Electrochemical Society* 163.5 (2016), A798–A809. ISSN: 0013-4651, 1945-7111. DOI: 10.1149/2.1151605jes. URL: https://iopscience.iop.org/article/10.1149/2.1151605jes (visited on 02/06/2024).

[59] Aashutosh N. Mistry, Kandler Smith, and Partha P. Mukherjee. "Secondary-Phase Stochastics in Lithium-Ion Battery Electrodes". In: *ACS Applied Materials & Interfaces* 10.7 (Feb. 21, 2018), pp. 6317–6326. ISSN: 1944-8244, 1944-8252. DOI: 10.1021/acsami.7b17771. URL: https://pubs.acs.org/doi/10.1021/acsami.7b17771 (visited on 01/04/2024).

[60] Petr Novák et al. "The complex electrochemistry of graphite electrodes in lithium-ion batteries". In: *Journal of power sources* 97 (2001), pp. 39–46.

[61] Petr Novák et al. "The complex electrochemistry of graphite electrodes in lithium-ion batteries". In: *Journal of Power Sources* 97-98 (July 2001), pp. 39–46. ISSN: 03787753. DOI: 10.1016/S0378-7753(01)00586-9. URL: https://linkinghub.elsevier.com/retrieve/pii/S0378775301005869 (visited on 08/31/2023).

[62] C. J. Orendorff. "The Role of Separators in Lithium-Ion Cell Safety". In: *Interface magazine* 21.2 (Jan. 1, 2012), pp. 61–65. ISSN: 1064-8208, 1944-8783. DOI: 10.1149/2.F07122if. URL: https://iopscience.iop.org/article/10.1149/2.F07122if (visited on 01/06/2024).

[63] Gordon T. Pace et al. "Comparative study of water-processable polymeric binders in LiMn $_{2}$ O $_{4}$ cathode for aqueous electrolyte batteries". In: *Nano Select* 2.5 (May 2021), pp. 939–947. ISSN: 2688-4011, 2688-4011. DOI: 10.1002/nano.202000167. URL: https://onlinelibrary.wiley.com/doi/10.1002/nano.202000167 (visited on 01/05/2024).

[64] Yoon-Soo Park, Eun-Suok Oh, and Sung-Man Lee. "Effect of polymeric binder type on the thermal stability and tolerance to roll-pressing of spherical natural graphite anodes for Li-ion batteries". In: *Journal of Power Sources* 248 (Feb. 2014), pp. 1191–1196. ISSN: 03787753. DOI: 10.1016/j.jpowsour.2013.10.076. URL: https://linkinghub.elsevier.com/retrieve/pii/S0378775313017424 (visited on 08/31/2023).

[65] Yoon-Soo Park, Eun-Suok Oh, and Sung-Man Lee. "Effect of polymeric binder type on the thermal stability and tolerance to roll-pressing of spherical natural graphite anodes for Li-ion batteries". In: *Journal of Power Sources* 248 (2014), pp. 1191–1196.

[66] European Parliament, Authorisation the Council concerning the Registration Evaluation, and 2006. Restriction of Chemicals (REACH). URL: https://echa.europa.eu/nl/substances-restricted-under-reach/-/dislist/details/0b0236e1827f617f. (visited 22/11/2023).

[67] Sireesha Pedaballi and Chia-Chen Li. "Effects of surface modification and organic binder type on cell performance of water-processed Ni-rich Li (Ni0. 8Co0. 1Mn0. 1) O2 cathodes". In: *Journal of Power Sources* 472 (2020), p. 228552.

[68] S. Pejovnik et al. "Electrochemical binding and wiring in battery materials". In: *Journal of Power Sources* 184.2 (Oct. 2008), pp. 593–597. ISSN: 03787753. DOI: 10.1016/j.jpowsour.2008.02.046. URL: https://linkinghub.elsevier.com/retrieve/pii/S0378775308003790 (visited on 01/06/2024).

[69] Hartmut Popp et al. "Mechanical methods for state determination of Lithium-Ion secondary batteries: A review". In: *Journal of Energy Storage* 32 (Dec. 2020), p. 101859. ISSN: 2352152X. DOI: 10.1016/j.est.2020.101859. URL: https://linkinghub.elsevier.com/retrieve/pii/S2352152X20316960 (visited on 01/06/2024).

[70] Daniel Pritzl et al. "Analysis of Vinylene Carbonate (VC) as Additive in Graphite/LiNi $_{0.5}$ Mn $_{1.5}$ O $_{4}$ Cells". In: *Journal of The Electrochemical Society* 164.12 (2017), A2625–A2635. ISSN: 0013-4651, 1945-7111. DOI: 10.1149/2.1441712jes. URL: https://iopscience.iop.org/article/10.1149/2.1441712jes (visited on 02/04/2024).

[71] H. Qiao and Q. Wei. "Functional nanofibers in lithium-ion batteries". In: *Functional Nanofibers and their Applications*. Elsevier, 2012, pp. 197–208. ISBN: 978-0-85709-069-0. DOI: 10.1533/9780857095640.2.197. URL: https://linkinghub.elsevier.com/retrieve/pii/B9780857090690500100 (visited on 02/01/2024).

[72] Maxwell D. Radin et al. "Narrowing the Gap between Theoretical and Practical Capacities in Li-Ion Layered Oxide Cathode Materials". In: *Advanced Energy Materials* 7.20 (Oct. 2017), p. 1602888. ISSN: 1614-6832, 1614-6840. DOI: 10.1002/aenm.201602888. URL: https://onlinelibrary.wiley.com/doi/10.1002/aenm.201602888 (visited on 01/05/2024).

[73] S Radloff et al. "Applying established water-based binders to aqueous processing of LiNi0. 83Co0. 12Mn0. 05O2 positive electrodes". In: *Journal of The Electrochemical Society* 168.10 (2021), p. 100506.

[74] S. Radloff et al. "Applying Established Water-Based Binders to Aqueous Processing of LiNi $_{0.83}$ Co $_{0.12}$ Mn $_{0.05}$ O $_{2}$ Positive Electrodes". In: *Journal of The Electrochemical Society* 168.10 (Oct. 1, 2021), p. 100506. ISSN: 0013-4651, 1945-7111. DOI: 10.1149/1945-7111/ac2861. URL: https://iopscience.iop.org/article/10.1149/1945-7111/ac2861 (visited on 10/24/2023).

[75] Johan Scheers et al. "All fluorine-free lithium battery electrolytes". In: *Journal of Power Sources* 251 (Apr. 2014), pp. 451–458. ISSN: 03787753. DOI: 10.1016/j.jpowsour.2013.11.042. URL: https://linkinghub.elsevier.com/retrieve/pii/S0378775313018697 (visited on 11/06/2023).

[76] Richard Schmuch et al. "Performance and cost of materials for lithium-based rechargeable automotive batteries". In: *Nature energy* 3.4 (2018), pp. 267–278.

[77] Kazunari Soeda, Masaki Yamagata, and Masashi Ishikawa. "Alginic Acid as a New Aqueous Slurry-Based Binder for Cathode Materials of LIB". In: *ECS Transactions* 64.18 (Feb. 10, 2015), pp. 13–22. ISSN: 1938-5862, 1938-6737. DOI: 10.1149/06418.0013ecst. URL: https://iopscience.iop.org/article/10.1149/06418.0013ecst (visited on 02/05/2024).

[78] Botao Farren Song, Abirami Dhanabalan, and Sibani Lisa Biswal. "Evaluating the capacity ratio and prelithiation strategies for extending cyclability in porous silicon composite anodes and lithium iron phosphate cathodes for high capacity lithium-ion batteries". In: *Journal of Energy Storage* 28 (Apr. 2020), p. 101268. ISSN: 2352152X. DOI: 10.1016/j.est.2020.101268. URL: https://linkinghub.elsevier.com/retrieve/pii/S2352152X19313799 (visited on 01/31/2024).

[79] Sushyanth Sridhar and Surender Reddy Salkuti. "Development and Future Scope of Renewable Energy and Energy Storage Systems". In: *Smart Cities* 5.2 (May 20, 2022), pp. 668–699. ISSN: 2624-6511. DOI: 10.3390/smartcities5020035. URL: https://www.mdpi.com/2624-6511/5/2/35 (visited on 01/06/2024).

[80] Selcuk Temiz et al. "State of charge and temperature-dependent impedance spectra regeneration of lithium-ion battery by duplex learning modeling". In: *Journal of Energy Storage* 64 (Aug. 2023), p. 107085. ISSN: 2352152X. DOI: 10.1016/j.est.2023.107085. URL: https://linkinghub.elsevier.com/retrieve/pii/S2352152X23004826 (visited on 02/07/2024).

[81] Ruiyuan Tian et al. “Quantifying the factors limiting rate performance in battery electrodes”. In: *Nature Communications* 10.1 (Apr. 29, 2019), p. 1933. ISSN: 2041-1723. DOI: 10.1038/s41467-019-09792-9. URL: https://www.nature.com/articles/s41467-019-09792-9 (visited on 01/09/2024).

[82] Pooja Vadhva et al. “Electrochemical Impedance Spectroscopy for All-Solid-State Batteries: Theory, Methods and Future Outlook”. In: *ChemElectroChem* 8.11 (June 2021), pp. 1930–1947. ISSN: 2196-0216, 2196-0216. DOI: 10.1002/celc.202100108. URL: https://chemistry-europe.onlinelibrary.wiley.com/doi/10.1002/celc.202100108 (visited on 01/07/2024).

[83] Mario Valvo et al. “Iron-Based Electrodes Meet Water-Based Preparation, Fluorine-Free Electrolyte and Binder: A Chance for More Sustainable Lithium-Ion Batteries?” In: *ChemSusChem* 10.11 (June 9, 2017), pp. 2431–2448. ISSN: 1864-5631, 1864-564X. DOI: 10.1002/cssc.201700070. URL: https://chemistry-europe.onlinelibrary.wiley.com/doi/10.1002/cssc.201700070 (visited on 01/10/2024).

[84] Bairav S. Vishnugopi, Ankit Verma, and Partha P. Mukherjee. “Fast Charging of Lithium-ion Batteries via Electrode Engineering”. In: *Journal of The Electrochemical Society* 167.9 (Jan. 7, 2020), p. 090508. ISSN: 0013-4651, 1945-7111. DOI: 10.1149/1945-7111/ab7fb9. URL: https://iopscience.iop.org/article/10.1149/1945-7111/ab7fb9 (visited on 01/04/2024).

[85] N. Von Aspern et al. “Fluorine and Lithium: Ideal Partners for High-Performance Rechargeable Battery Electrolytes”. In: *Angewandte Chemie International Edition* 58.45 (Nov. 4, 2019), pp. 15978–16000. ISSN: 1433-7851, 1521-3773. DOI: 10.1002/anie.201901381. URL: https://onlinelibrary.wiley.com/doi/10.1002/anie.201901381 (visited on 01/10/2024).

[86] Wandi Wahyudi et al. “Phase inversion strategy to flexible freestanding electrode: critical coupling of binders and electrolytes for high performance Li–S battery”. In: *Advanced Functional Materials* 28.34 (2018), p. 1802244.

[87] Wandi Wahyudi et al. “Phase Inversion Strategy to Flexible Freestanding Electrode: Critical Coupling of Binders and Electrolytes for High Performance Li-S Battery”. In: *Advanced Functional Materials* 28.34 (Aug. 2018), p. 1802244. ISSN: 1616301X. DOI: 10.1002/adfm.201802244. URL: https://onlinelibrary.wiley.com/doi/10.1002/adfm.201802244 (visited on 09/13/2023).

[88] Chao-Yang Wang et al. “Fast charging of energy-dense lithium-ion batteries”. In: *Nature* 611.7936 (Nov. 17, 2022), pp. 485–490. ISSN: 0028-0836, 1476-4687. DOI: 10.1038/s41586-022-05281-0. URL: https://www.nature.com/articles/s41586-022-05281-0 (visited on 01/04/2024).

[89] Sai Wang et al. “Properties of Lithium bis (oxatlato) borate (LiBOB) as a Lithium Salt and cycle performance in LiMn2O4 Half Cell”. In: *Int. J. Electrochem. Sci* 1.5 (2006), pp. 250–257.

[90] Susanne Wilken, Patrik Johansson, and Per Jacobsson. “Infrared spectroscopy of instantaneous decomposition products of LiPF6-based lithium battery electrolytes”. In: *Solid State Ionics* 225 (Oct. 2012), pp. 608–610. ISSN: 01672738. DOI: 10.1016/j.ssi.2012.02.004. URL: https://linkinghub.elsevier.com/retrieve/pii/S0167273812000720 (visited on 01/10/2024).

[91] Bizhong Xia, Bo Ye, and Jianwen Cao. “Polarization Voltage Characterization of Lithium-Ion Batteries Based on a Lumped Diffusion Model and Joint Parameter Estimation Algorithm”. In: *Energies* 15.3 (Feb. 4, 2022), p. 1150. ISSN: 1996-1073. DOI: 10.3390/en15031150. URL: https://www.mdpi.com/1996-1073/15/3/1150 (visited on 01/29/2024).

[92] Jian Xia et al. “A Comparative Study of a Family of Sulfate Electrolyte Additives”. In: *Journal of The Electrochemical Society* 161.3 (2014), A264–A274. ISSN: 0013-4651, 1945-7111. DOI: 10.1149/2.015403jes. URL: https://iopscience.iop.org/article/10.1149/2.015403jes (visited on 02/06/2024).

[93] Jian Xia et al. “One Sulfonate and Three Sulfate Electrolyte Additives Studied in Graphite/LiCoO $_2$ Pouch Cells”. In: *Journal of The Electrochemical Society* 162.12 (2015), A2227–A2235. ISSN: 0013-4651, 1945-7111. DOI: 10.1149/2.0151512jes. URL: https://iopscience.iop.org/article/10.1149/2.0151512jes (visited on 11/10/2023).

[94] Kang Xu. “Tailoring Electrolyte Composition for LiBOB”. In: *Journal of The Electrochemical Society* 155.10 (2008), A733. ISSN: 00134651. DOI: 10.1149/1.2961055. URL: https://iopscience.iop.org/article/10.1149/1.2961055 (visited on 12/29/2023).

[95] Kang Xu, Shengshui Zhang, and T. Richard Jow. "Formation of the Graphite/Electrolyte Interface by Lithium Bis(oxalato)borate". In: *Electrochemical and Solid-State Letters* 6.6 (2003), A117. ISSN: 10990062. DOI: 10.1149/1.1568173. URL: https://iopscience.iop.org/article/10.1149/1.1568173 (visited on 12/29/2023).

[96] Kang Xu, Shengshui Zhang, and T. Richard Jow. "LiBOB as Additive in LiPF[sub 6]-Based Lithium Ion Electrolytes". In: *Electrochemical and Solid-State Letters* 8.7 (2005), A365. ISSN: 10990062. DOI: 10.1149/1.1924930. URL: https://iopscience.iop.org/article/10.1149/1.1924930 (visited on 12/29/2023).

[97] Kang Xu et al. "Chemical Analysis of Graphite/Electrolyte Interface Formed in LiBOB-Based Electrolytes". In: *Electrochemical and Solid-State Letters* 6.7 (2003), A144. ISSN: 10990062. DOI: 10.1149/1.1576049. URL: https://iopscience.iop.org/article/10.1149/1.1576049 (visited on 12/29/2023).

[98] Kang Xu et al. "LiBOB as Salt for Lithium-Ion Batteries:A Possible Solution for High Temperature Operation". In: *Electrochemical and Solid-State Letters* 5.1 (2002), A26. ISSN: 10990062. DOI: 10.1149/1.1426042. URL: https://iopscience.iop.org/article/10.1149/1.1426042 (visited on 12/29/2023).

[99] Ningbo Xu et al. "Research progress of fluorine-containing electrolyte additives for lithium ion batteries". In: *Journal of Power Sources Advances* 7 (Feb. 2021), p. 100043. ISSN: 26662485. DOI: 10.1016/j.powera.2020.100043. URL: https://linkinghub.elsevier.com/retrieve/pii/S2666248520300433 (visited on 01/10/2024).

[100] Naoaki Yabuuchi et al. "Electrochemical Properties of LiCoO $_2$ Electrodes with Latex Binders on High-Voltage Exposure". In: *Journal of The Electrochemical Society* 162.4 (2015), A538–A544. ISSN: 0013-4651, 1945-7111. DOI: 10.1149/2.0151504jes. URL: https://iopscience.iop.org/article/10.1149/2.0151504jes (visited on 12/30/2023).

[101] Yu-Xing Yao, Chong Yan, and Qiang Zhang. "Emerging interfacial chemistry of graphite anodes in lithium-ion batteries". In: *Chemical Communications* 56.93 (2020), pp. 14570–14584. ISSN: 1359-7345, 1364-548X. DOI: 10.1039/D0CC05084A. URL: http://xlink.rsc.org/?DOI=D0CC05084A (visited on 01/04/2024).

[102] Meng Yu et al. "Weakened Capacity Fading of Li-Rich Cathode via Aqueous Binder for Advanced Lithium Ion Batteries". In: *Journal of The Electrochemical Society* 166.16 (2019), A4122.

[103] Chris Yuan et al. "Water-based manufacturing of lithium ion battery for life cycle impact mitigation". In: *CIRP Annals* 70.1 (2021), pp. 25–28.

[104] Caiping Zhang et al. "A Generalized SOC-OCV Model for Lithium-Ion Batteries and the SOC Estimation for LNMCO Battery". In: *Energies* 9.11 (Nov. 1, 2016), p. 900. ISSN: 1996-1073. DOI: 10.3390/en9110900. URL: http://www.mdpi.com/1996-1073/9/11/900 (visited on 02/08/2024).

[105] Hao Zhang et al. "Graphite as anode materials: Fundamental mechanism, recent progress and advances". In: *Energy Storage Materials* 36 (Apr. 2021), pp. 147–170. ISSN: 24058297. DOI: 10.1016/j.ensm.2020.12.027. URL: https://linkinghub.elsevier.com/retrieve/pii/S2405829720304906 (visited on 01/04/2024).

[106] Honghe Zheng et al. "A comprehensive understanding of electrode thickness effects on the electrochemical performances of Li-ion battery cathodes". In: *Electrochimica Acta* 71 (June 2012), pp. 258–265. ISSN: 00134686. DOI: 10.1016/j.electacta.2012.03.161. URL: https://linkinghub.elsevier.com/retrieve/pii/S0013468612005270 (visited on 01/29/2024).

[107] Honghe Zheng et al. "Cooperation between Active Material, Polymeric Binder and Conductive Carbon Additive in Lithium Ion Battery Cathode". In: *The Journal of Physical Chemistry C* 116.7 (Feb. 23, 2012), pp. 4875–4882. ISSN: 1932-7447, 1932-7455. DOI: 10.1021/jp208428w. URL: https://pubs.acs.org/doi/10.1021/jp208428w (visited on 01/06/2024).

# A

# Results

*Appendix voor de overige grafieken en informatie die niet perse in de scriptie passen.*

## A.1. Electrochemical characterisation

### A.1.1. Graphite vs. lithium rate performance cycling

| Electrode | Capacity (mAh/cm$^2$) | Thickness ($\mu$m) | Porosity (%) |
|---|---|---|---|
| PAA_CONVA1 | 4.23 | 142 | 52 |
| PAA_APIA1 | 4.28 | 130 | 48 |
| PVDF_CONVA1 | 3.46 | 95 | 46 |
| PVDF_HPIA1 | 3.93 | 104 | 45 |
| PES_HPIA | 5.54 | 141 | 45 |

**Table A.1:** Graphite based electrode specifications for half cell rate performance cycling.

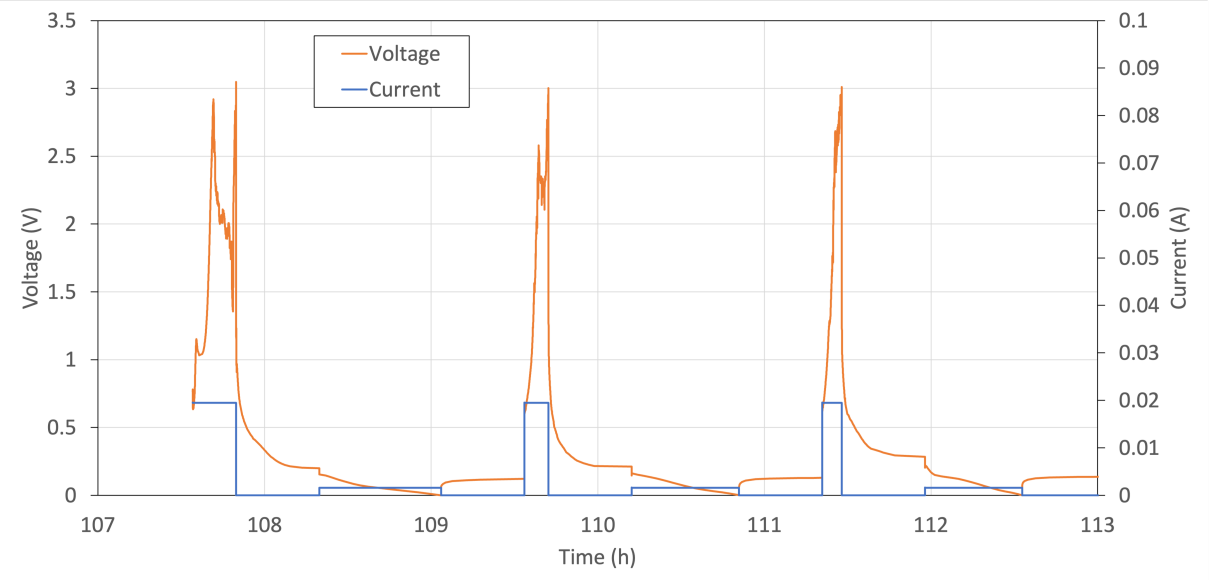


**Figure A.1:** Voltage curve of the 4C rate performance cycles of the PAA conv based graphite half cells.

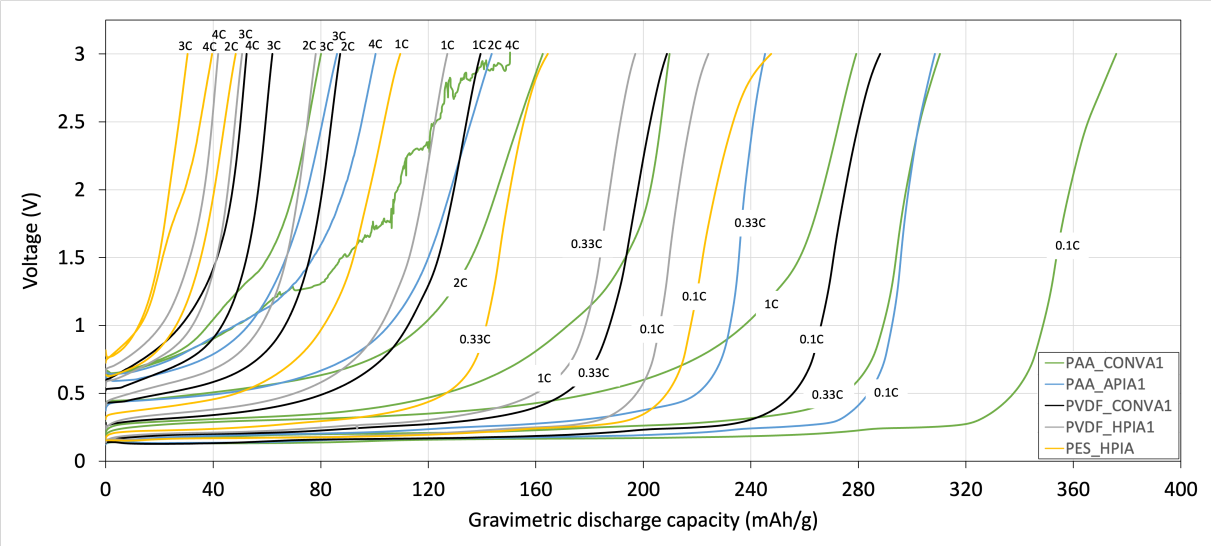


**Figure A.2:** Voltage plotted against the gravimetric discharge capacity of each last rate cycle for each anode half cell.

## A.1.2. Graphite vs. lithium long term cycling

| Electrode | Capacity (mAh/cm$^2$) | Thickness ($\mu$m) | Porosity (%) |
|---|---|---|---|
| PAA_CONVA2 | 4.72 | 129 | 48 |
| PAA_APIA2 | 3.96 | 102 | 43 |
| PVDF_CONVA2 | 2.94 | 89 | 50 |
| PVDF_HPIA2 | 3.66 | 96 | 44 |
| PAA_CONVA3 | 4.20 | 145 | 59 |
| PAA_APIA3 | 3.89 | 119 | 53 |
| PVDF_CONVA3 | 3.07 | 92 | 51 |
| PVDF_HPIA3 | 3.67 | 114 | 53 |

**Table A.2:** Graphite based electrode specifications for half cell long term cycling.

### A.1.3. NMC vs. lithium rate performance cycling

| Electrode | Capacity (mAh/cm$^2$) | Thickness ($\mu$m) | Porosity (%) |
|---|---|---|---|
| CMC/SBR_CONVC1 | 5.57 | 182 | 60 |
| CMC/SBR_CONVC2 | 3.67 | 143 | 52 |
| CMC/SBR_IPIC1 | 5.91 | 174 | 47 |
| CMC/SBR_IPIC2 | 5.54 | 167 | 48 |
| CMC/PAA_CONVC1 | 3.87 | N/A | N/A |
| CMC/PAA_CONVC2 | 4.02 | N/A | N/A |
| PAA_CONVC | 2.51 | 80 | 51 |
| PVDF_CONVC1 | 3.64 | 91 | 37 |
| PVDF_CONVC2 | 3.68 | 88 | 35 |

**Table A.3:** NMC811 based electrode specifications for half cell rate performance test.

### A.1.4. NMC vs. lithium long term cycling

| Electrode | Capacity (mAh/cm$^2$) | Thickness ($\mu$m) | Porosity (%) |
|---|---|---|---|
| CMC/SBR_CONVC3 | 4.7 | 190 | 52 |
| CMC/SBR_IPIC3 | 6 | 205 | 51 |
| PVDF_CONVC3 | 4 | 103 | 29 |
| PVDF_EPIC | 3.6 | 123 | 48 |

**Table A.4:** NMC811 based electrode specifications for half cell long term cycling test.

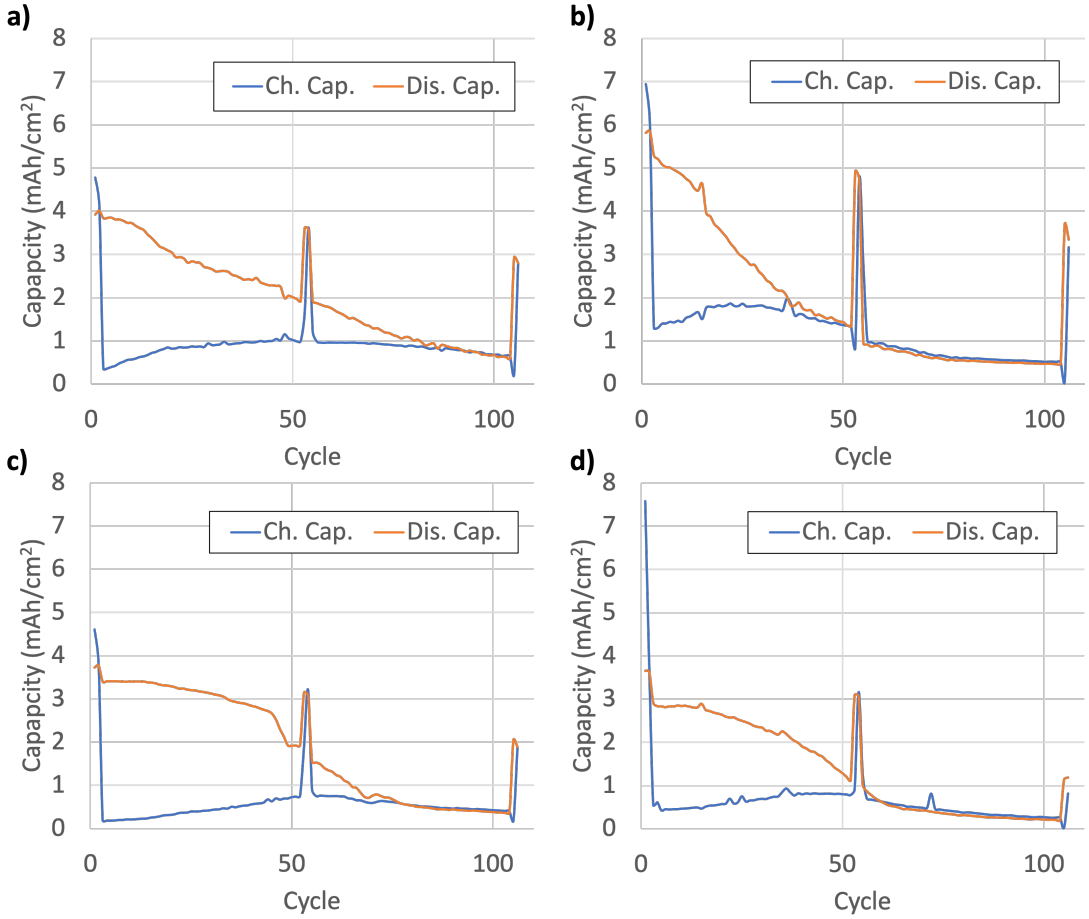


**Figure A.3:** Overview of the constant voltage charge and discharge capacities for CMC/SBR_CONVC (a), CMC/SBR_IPIC (b), PVDF_CONVC (c) and PVDF_EPIC (d) .

### A.1.5. Graphite vs. NMC

| Electrode | Capacity (mAh/cm$^2$) | Anode porosity (%) | Thickness ($\mu$m) |
|---|---|---|---|
| A:PAA_C:PVDF 1 | A:3.80, C:3.25 | 54 | 113 |
| A:PAA_C:PVDF 2 | A:4.20, C:3.50 | 54 | 123 |
| A:PVDF_C:CMCSBR 1 | A:4.12, C:3.40 | 50 | 111 |
| A:PVDF_C:CMCSBR 2 | A:4.07, C:3.62 | 54 | 116 |
| A:PAA_C:CMCSBR 1 | A:4.17, C:4.3.30 | 48 | 107 |
| A:PAA_C:CMCSBR 2 | A:4.37, C:3.37 | 59 | 130 |
| A:PVDF_C:PVDF 1 | A:3.99, C:3.28 | 54 | 115 |
| A:PVDF_C:PVDF 2 | A:3.99, C:3.23 | 52 | 110 |

**Table A.5:** Specifications on the electrode properties used in the combination test.

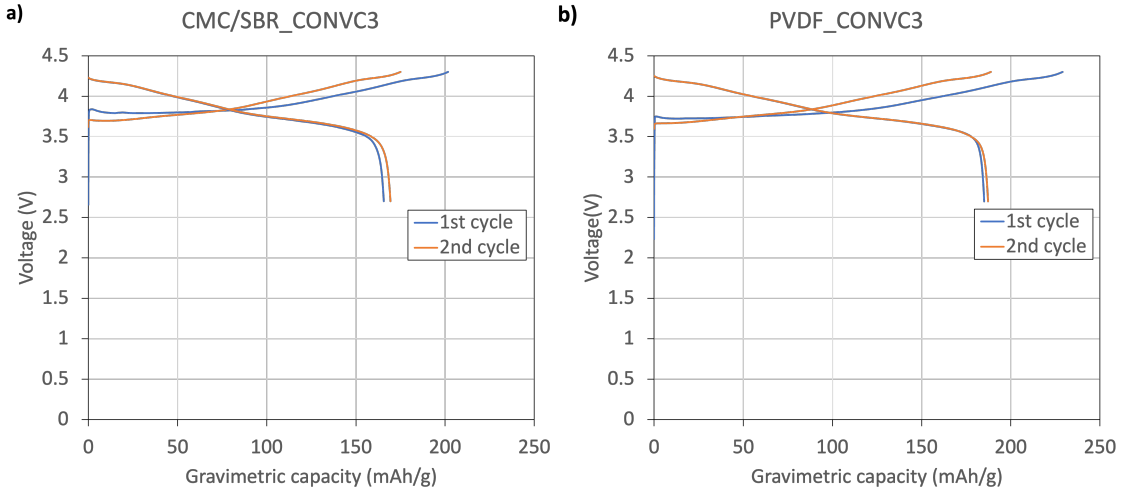


**Figure A.4:** Voltage curves of the formation cycles of CMC/SBR_CONVC3 (a) and PVDF_CONVC3 (b).